

THE GENERATION OF IPDF MICROPULSATIONS, WITH SPECIAL
ATTENTION TO FREQUENCY SHIFT MECHANISMS

by

THOMAS W. KOLESZAR

M.Sc., The University of British Columbia, 1980

B.Sc. (Honours), The University of British Columbia, 1978

A THESIS SUBMITTED IN PARTIAL FULFILMENT OF
THE REQUIREMENTS FOR THE DEGREE OF
DOCTOR OF PHILOSOPHY

in

THE FACULTY OF GRADUATE STUDIES
Geophysics and Astronomy

We accept this thesis as conforming
to the required standard

THE UNIVERSITY OF BRITISH COLUMBIA

December 1988

© THOMAS W. KOLESZAR, 1988

In presenting this thesis in partial fulfilment of the requirements for an advanced degree at the University of British Columbia, I agree that the Library shall make it freely available for reference and study. I further agree that permission for extensive copying of this thesis for scholarly purposes may be granted by the head of my department or by his or her representatives. It is understood that copying or publication of this thesis for financial gain shall not be allowed without my written permission.

Department of GEOP. + ASTR.

The University of British Columbia
Vancouver, Canada

Date Dec. 15 / 88

ABSTRACT

Short period geomagnetic micropulsations termed IPDPs (Intervals of Pulsations of Diminishing Period) are investigated using ground station data, geosynchronous satellite magnetograms, and the Kp and Dst geomagnetic indices. A model for the generation of IPDPs is described, and consideration is given to three mechanisms which could be responsible for the IPDP frequency rise: the inward motion, azimuthal drift, and increasing background magnetic field mechanisms. A simplified IPDP generation model containing the first two of these mechanisms is tested by computer simulation. Results from this simulation indicate the possibility of significant source region inward motion without actual plasmopause displacement, and the possibility of eastward developing IPDPs. Using amplitude variations along a north-south line of ground stations, two methods, each applicable under different ionospheric propagation conditions, are developed for quantitatively determining the inward motion of the IPDP source region. A system for qualitatively determining the potential influence of the increasing background field mechanism on an IPDP using the Dst index and geosynchronous satellite magnetograms is also formulated. Lastly, a technique for the assessment of the effects of the azimuthal drift mechanism, in conjunction with the inward motion mechanism, is developed. This

technique assumes that only these two mechanisms are operating. In addition to addressing the frequency shift mechanisms, it provides estimates of the injection boundary position and the magnitude of any (ring current created) magnetic field depression in the IPDP source region. The frequency rises of two IPDPs are analyzed in detail using these methods. In both cases, the inward motion effect is the dominant factor in producing the frequency rise, with the increasing background field mechanism having no significant effect. The azimuthal drift mechanism is a secondary factor in creating one event's frequency rise, and actually suppresses the frequency rise of the other event. The computer simulation calculations also generally show the inward motion mechanism to be the dominant effect in producing IPDP frequency rises. Longitudinal variations within an IPDP event are also examined. The results of this examination are consistent with the IPDP generation model used here, which includes showing significant variations between stations spaced comparatively closely in longitude.

TABLE OF CONTENTS

ABSTRACT	ii
ACKNOWLEDGEMENTS	x
Chapter 1. INTRODUCTION	1
Chapter 2. DATA SOURCES AND ANALYSIS	8
2.1. Data Sources	8
2.2. Data Processing	14
Chapter 3. PROPERTIES OF IPDPS	20
3.1. Physical Characteristics	20
3.2. Occurrence of IPDPS	25
3.3. Network Observations	31
3.4. Satellite Observations	34
3.5. Relation to Geomagnetic Phenomena	37
Chapter 4. MAGNETOSPHERIC MODEL OF IPDP GENERATION	40
4.1. IPDP - Substorm Model	40
4.2. IPDP Frequency Shift Mechanisms	55
4.2.1. Inward Motion	56
4.2.2. Increasing Background Field ..	58
4.2.3. Azimuthal Drift	59
4.3. Discussion of IPDP Frequency Shift Mechanisms	61
4.4. IPDP Frequency Behaviour Simulation ..	65
4.4.1. Computational Procedure	66
4.4.2. Model IPDPS versus Observed IPDPS	73
4.4.3. Other Model Results and Predictions	82
4.4.4. Model Versus Real GMLTs	88
4.4.5. Discussion of IPDP Simulation Model	92
Chapter 5. EXPERIMENTAL RESULTS	95
5.1. Inward Motion of IPDP Source Region ..	95
5.1.1. Feb. 14 Event	96
5.1.2. Feb. 15 Event	111
5.2. Magnetic Field Changes in IPDP Source Region	122
5.2.1. Ring Current Versus IPDPS ..	125
5.2.2. Individual IPDP Event Assessments	134
5.2.3. Ring Current and Inward Motion Mechanism	148
5.2.4. Discussion of Ring Current Effects on IPDPS	152

5.3. Azimuthal Drift Effects on IPDP	
Frequency Evolution	155
5.3.1. Feb. 14 Event	164
5.3.2. Feb. 15 Event	176
5.4. Longitudinal IPDP Development	182
5.4.1. Feb. 14 Event	184
5.4.2. Feb. 15 Event	186
5.4.3. Feb. 24c Event	190
5.4.4. Discussion	193
5.5. Discussion of Experimental Results ..	196
Chapter 6. CONCLUSION	202
REFERENCES	206
Appendix A. THE ION-CYCLOTRON INSTABILITY AND IPDP FREQUENCY	214
Appendix B. THE IONOSPHERIC WAVEGUIDE	217
Appendix C. GEOMAGNETIC INDICES	227

List of Tables

Table I: Geomagnetic Variations	2
Table II: Micropulsation Classification	3
Table III: ULF Station Coordinates	9
Table IV: IPDP Events	13
Table V: Magnetic Observatory Coordinates	15
Table VI: IPDP Physical Characteristics	22
Table VII: IPDP Occurrence Characteristics	26
Table VIII: Model IPDP Characteristics	75

List of Figures

Figure 1: Pc 1 Range Dynamic Spectra	5
Figure 2: Feb. 15 IPDP Event	6
Figure 3: ULF Station Location Map	10
Figure 4: Dynamic Spectra: Feb. 14 IPDP	21
Figure 5: Chart Record: Feb. 14 IPDP	24
Figure 6: Diurnal Distribution of IPDP Occurrence	27
Figure 7: IPDP Occurrence versus Kp Index	28
Figure 8: Co-Longitudinal Site Comparison: Feb. 14 IPDP ..	33
Figure 9: Co-Latitudinal Site Comparison: Feb. 24c IPDP ..	35
Figure 10: IPDP Observations: Satellite versus Ground	36
Figure 11: Double-spiral Injection Boundary	42
Figure 12: Injection Boundary Position versus Kp	43
Figure 13: Proton Injection and Drift Trajectories	48
Figure 14: Substorm Current Systems	50
Figure 15: Three Average Plasmapause Profiles	54
Figure 16: The Inward Motion Δf Mechanism	63
Figure 17: Computer Simulation Flow Chart	69
Figure 18: Frequency and Slope vs GM Lat. (simulation) ...	77
Figure 19: IPDP Occurrence versus Activity (simulation) ...	78
Figure 20: Frequency and Slope versus GMLT (simulation) ..	80
Figure 21: Onset Drift versus Activity (simulation)	81
Figure 22: Inward Motion Effects on IPDPs (simulation) ...	83
Figure 23: Westward and Eastward Developing IPDP Models ..	87
Figure 24: West and Eastward IPDP results (simulation) ...	89

Figure 25: Modelled versus Observed IPDP GMLTs	91
Figure 26: Polarization Spectrogram; 0840UT, Feb. 14	98
Figure 27: Pol. Spectrograms; PS: 0900, 0940 UT, Feb. 14	100
Figure 28: Pol. Spectrograms; LL: 0900, 0940 UT, Feb. 14	101
Figure 29: X and Y Component Power Variations, Feb. 14 ..	103
Figure 30: Power Ratios versus Position, Feb. 14 IPDP ...	106
Figure 31: Source Inward Motion, Feb. 14 IPDP	110
Figure 32: Inward Motion Frequency Rise, Feb. 14 IPDP ...	112
Figure 33: Polarization Spectrogram; 2157UT, Feb. 15	114
Figure 34: PS and LL Pol. Spectrograms; 2201UT, Feb. 15 ..	115
Figure 35: Source - Station Geometry: 2149UT, Feb. 15 ...	117
Figure 36: Source Position Estimation: 2149UT, Feb. 15 ..	119
Figure 37: Power Ratios versus Position, Feb. 15 IPDP ...	121
Figure 38: Source Inward Motion, Feb. 15 IPDP	123
Figure 39: Inward Motion Frequency Rise, Feb. 15 IPDP ...	124
Figure 40: Ring Current Development: ΔB Profiles	129
Figure 41: Magnetic Field Behaviour: IPDP Source Region ..	133
Figure 42: IPDP Occurrence versus Dst Index	135
Figure 43: IPDPs versus Dst Index: Case I - IV Samples ..	136
Figure 44: IPDP versus Dst and GOES 2; Feb. 14	138
Figure 45: IPDP versus Dst and GOES 2; Feb. 15	140
Figure 46: Great Whale River Magnetogram, Feb. 15	141
Figure 47: IPDP versus Dst and GOES 3; Jan. 29	143
Figure 48: IPDP versus Dst and GOES 3; Feb. 24c	145
Figure 49: Inward Motion + $\Delta B \Delta f$: Feb. 15	153

Figure 50: Injection Boundary Estimation Flow Chart	165
Figure 51: X-component Magnetogram: GWR, Feb. 14	167
Figure 52: Model Plot for the Feb. 14 IPDP	169
Figure 53: Frequency Shift Results: Feb. 14 IPDP	170
Figure 54: Combined Frequency Rise Results: Feb. 14 IPDP	173
Figure 55: Poor Injection Boundary Results: Feb. 14 IPDP	175
Figure 56: Great Whale River Magnetogram: Feb. 15 IPDP ..	177
Figure 57: Model Plot for the Feb. 15 IPDP	179
Figure 58: Frequency Shift Results: Feb. 15 IPDP	181
Figure 59: Combined Frequency Rise Results: Feb. 14 IPDP	183
Figure 60: Freq. Profiles from GM and PS: Feb. 14 IPDP ..	185
Figure 61: Power Spectra from GM and PS: 0910UT, Feb. 14	187
Figure 62: Freq. Profiles from GM and PS: Feb. 15 IPDP ..	188
Figure 63: Cross-Correlations: LL-PS and GM-PS, Feb. 15	191
Figure 64: Freq. Profiles: GM, PS, and PG; Feb. 24c IPDP	192
Figure 65: Ionospheric Electron Density Profiles	218
Figure 66: Ionospheric Duct Paths and Reflection Coefficients	221

ACKNOWLEDGEMENTS

I express my deepest thanks to my supervisor, Dr. T. Watanabe, for his invaluable advice and constant encouragement. I also offer my thanks to Drs. G. Clarke, R. Ellis, G. Fahlmann, and B. Shizgal for their participation as committee members. My special thanks go to Sonya Dehler, who helped keep me sane through the trials of thesis preparation, to my mother, Mrs. S. Koleszar, for her patient editing of this thesis, and to wife, Ulrike, for her unending encouragement and support during my time at UBC.

I express my appreciation to Drs. T. Oguti, S. Kokubun and K. Hayashi, University of Tokyo, Drs. T. Kitamura and O. Saka, Kyushu University, and Dr. R.E. Horita, University of Victoria, for their efforts in acquiring the IPDP data set (Pulsating Aurora Campaign). The GOES 2 and 3 magnetic data were supplied from the World Data Center, Boulder, Colorado, and were processed by Drs. S. Kokubun and G. Ishida of the University of Tokyo. The auroral-zone station magnetograms and the Kp index data were also obtained from the World Data Centre, Boulder, Colorado, and the Dst index data from the World Data Centre, Greenbelt, Maryland.

This thesis research was supported by the Natural Sciences and Engineering Research Council of Canada through Grant A - 3564. The Pulsating Aurora Campaign was supported by the same agency through Grant A - 3397.

CHAPTER 1. INTRODUCTION

The Earth's magnetic field is subject to many kinds of variations. These fluctuations, which can be of either internal or external origin, range in period from 10^7 years down to ≈ 1 second. Table I presents a summary of such geomagnetic variations. The family of fluctuations of interest here, the micropulsations, occupies the shorter end of this period range.

Geomagnetic micropulsations have periods in the range of 600 to 0.2 seconds. They are transitory fluctuations of small amplitude, typically less than 1 part in 10^4 of the geomagnetic field strength at the Earth's surface, which leave no permanent effect on Earth's main field. Their origin is external, meaning that they are generated either directly or indirectly as a result of solar wind magnetosphere interactions. Though they were first reported more than a century ago (Stewart, 1861), the study of micropulsations is a relatively young field with most of the research in the area occurring within the last 25 years.

Based on morphological differences, micropulsations have been divided into two broad classes; continuous pulsations, or Pc, and irregular or impulsive pulsations, termed Pi. These classes have been further divided into subclasses as shown in Table II. Each of these subclasses may also contain many morphologically distinct types of

Table I
Geomagnetic Variations

<u>Variation</u>	<u>Origin</u>	<u>Period (seconds)</u>
Dipole Reversals	Internal	10^{15}
Secular	Internal	$10^9 - 10^{10}$
Magnetic Storms	External	10^6
Diurnal	External	10^5
Substorms	External	$10^4 - 10^5$
Micropulsations	External	$10^2 - 10^0$

(After Jacobs, 1970)

Table II
Micropulsation Classification

<u>Continuous Pulsations (Pc)</u>	<u>Period Range (seconds)</u>
Pc 1	0.2 - 5
Pc 2	5 - 10
Pc 3	10 - 45
Pc 4	45 - 150
Pc 5	150 - 600
Pc 6	600 -
<u>Irregular Pulsations (Pi)</u>	<u>Period Range (seconds)</u>
Pi 1	1 - 40
Pi 2	40 - 150
Pi 3	150 -

(After Nishida, 1978)

micropulsation. A summary plot (fig. 1) of Pc 1 range micropulsation dynamic spectra shows those types falling within the Pc 1 frequency range, including IPDPs, the subject of this thesis.

The acronym IPDP comes from the name Interval of Pulsations of Diminishing Period. IPDPs were first named by Troitskaya and Melnikova (1959), and first described in some detail by Troitskaya (1961). The name makes reference to the distinguishing feature of all IPDPs; the rising frequency trend displayed throughout each 20 minute to 2 hour long event. In the past, other names have also been applied to IPDPs; these include Solar Whistles (Duffus et al., 1958), Gurglers (Tepley and Amundsen, 1964), and Sweepers (Heacock, 1967). More recently, the term ODP, meaning Oscillations of Declining Period, has been used by Barkova and Solov'ev (1984) and Dovbnya et al. (1984). An example of an IPDP dynamic spectrum and waveform is shown in figure 2.

It has often been noted that IPDPs could become a useful tool for magnetospheric research (Troitskaya, 1961; Bossen et al., 1976; Heacock et al., 1976; Maltseva et al., 1981). Before this possibility can become a reality however, we must develop a good understanding of the IPDP generation mechanism, especially those effects which control the frequency rise. In view of this, three proposed frequency increase mechanisms have received the most

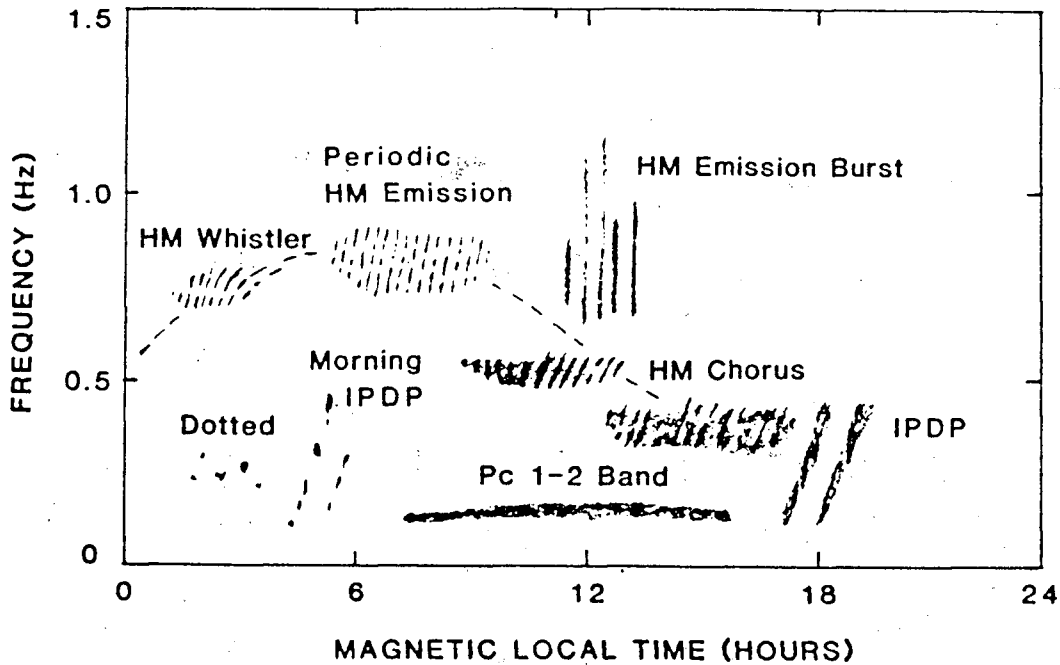


FIGURE 1.

Summary plot of dynamic spectra of Pc 1 range micropulsations versus geomagnetic local time (after Fukunishi et al., 1981). Note the IPDP spectra in the lower part of the Pc 1 frequency range near 1800 magnetic local time.

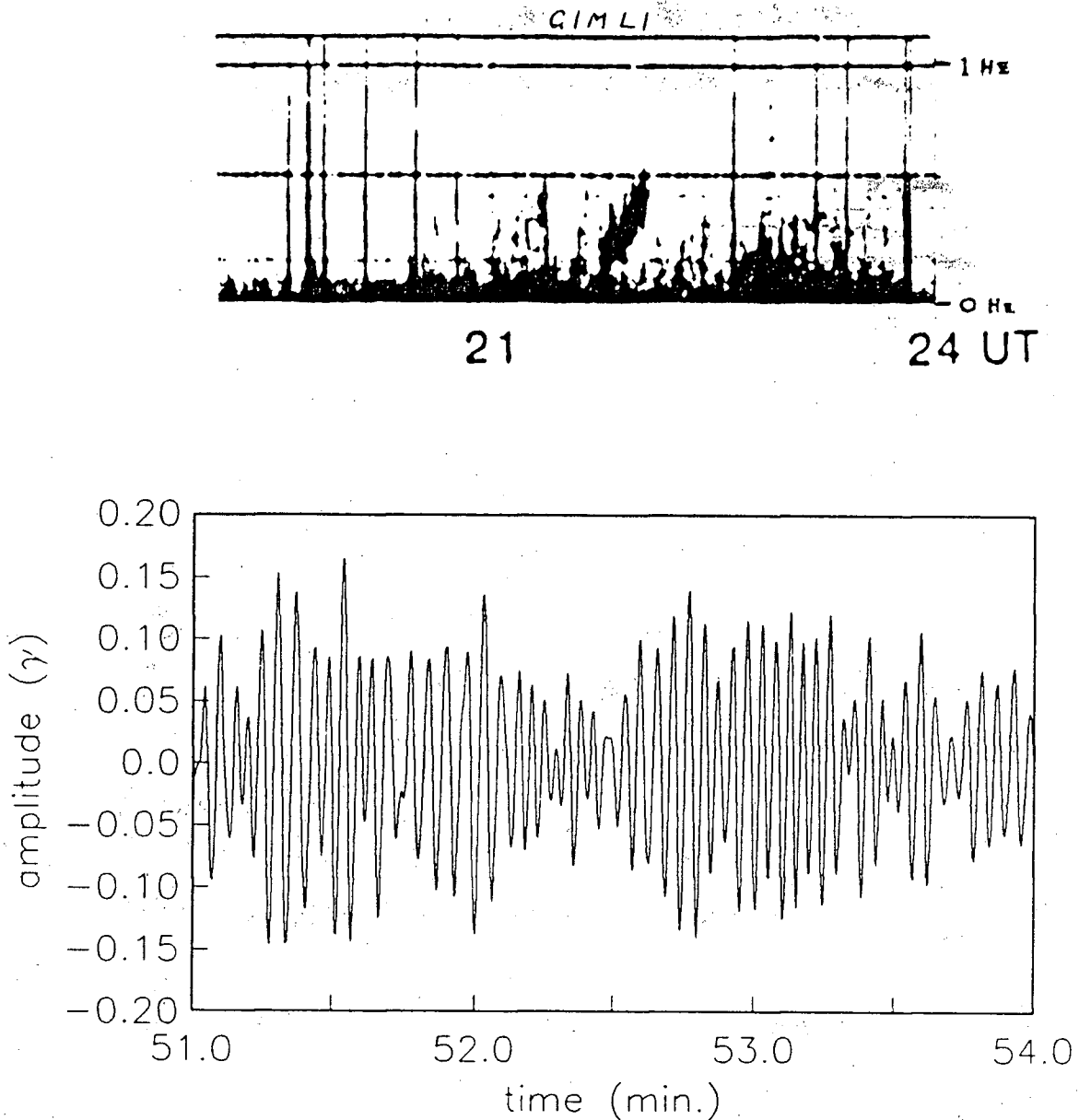


FIGURE 2.

Dynamic spectrum of the horizontal components (top), and chart record (bottom) of the Y component for the February 15 IPDP event as observed at Gimli, Manitoba (cf. Table III and fig. 3). The chart record covers only 3 minutes (2151 - 2154 UT) near the beginning of the event.

attention; inward motion of the generation region (Gendrin et al., 1967; Heacock, 1967), westward drift of hot protons (Fukunishi, 1969), and increasing background magnetic field strength (Roxburgh, 1970). It has also been observed that more than one of these mechanisms may operate at once (Heacock, 1973; Kangas et al., 1974).

Using ground-based and satellite data, this thesis will present a quantitative assessment of the possible contribution of each of these mechanisms to the IPDP frequency rise in the context of an overall model for IPDP generation. Chapter Two will describe the data sources and analysis methods used here, while Chapter Three is an in depth description of IPDPs and their relationships to other geomagnetic phenomena. The generation process of IPDPs is discussed in Chapter Four, including the frequency shift mechanisms, while Chapter Five presents the results of the experimental tests of these mechanisms, along with a discussion of their significance.

CHAPTER 2. DATA SOURCES AND ANALYSIS

This chapter offers a description of the data sets used in this thesis, followed by a review of the techniques used in the analysis of the IPDP data.

2.1. DATA SOURCES

The research work presented in Chapters Four and Five made use of information from five sources: the 1980 "Aurora-ULF-VLF" campaign micropulsation records, GOES satellite magnetograms, magnetograms from auroral zone magnetic observatories, Kp indices, and Dst indices.

The primary data source, that of the IPDP micropulsation records, was the "Aurora-ULF-VLF" campaign (Oguti et al., 1982). As part of this project, thirteen ULF stations were operated in western Canada at auroral zone and plasmapause latitudes during January and February of 1980. Eleven of the thirteen stations were located at latitudes suitable for recording IPDPs. These stations are listed, along with their geographic and corrected geomagnetic coordinates (Gustafsson, 1984), in Table III, and their locations are plotted in figure 3. The network they comprised consisted essentially of three north-south lines of stations; one each in British Columbia, Saskatchewan, and Manitoba (cf. fig. 3). Two east-west lines could also be constructed from the network; a northern line of SR, LR, and

Table III
ULF Station Names and Coordinates

	<u>Geographic</u>		<u>Corrected</u> <u>Geomagnetic</u>	
	<u>Lat. (°N)</u>	<u>Long. (°E)</u>	<u>Lat. (°N)</u>	<u>Long. (°E)</u>
<u>Manitoba Line</u>				
Island Lake (IL)	53.9	265.3	64.9	329.6
Gimli (GM)	50.6	263.0	61.4	326.8
<u>Saskatchewan Line</u>				
Rabbit Lake (RL)	58.2	256.3	67.8	314.8
South End (SE)	56.3	256.5	66.0	315.8
La Ronge (LR)	55.2	254.7	64.6	313.7
Waskesiu (WS)	53.9	253.9	63.1	313.1
Park Site (PS)	52.2	252.8	61.3	312.2
Lucky Lake (LL)	51.0	252.9	60.1	312.7
<u>B.C. Line</u>				
Steen River (SR)	59.7	242.8	66.6	295.7
Prince George (PG)	53.9	237.1	59.6	292.4
Victoria (VC)	48.3	236.4	53.8	294.1

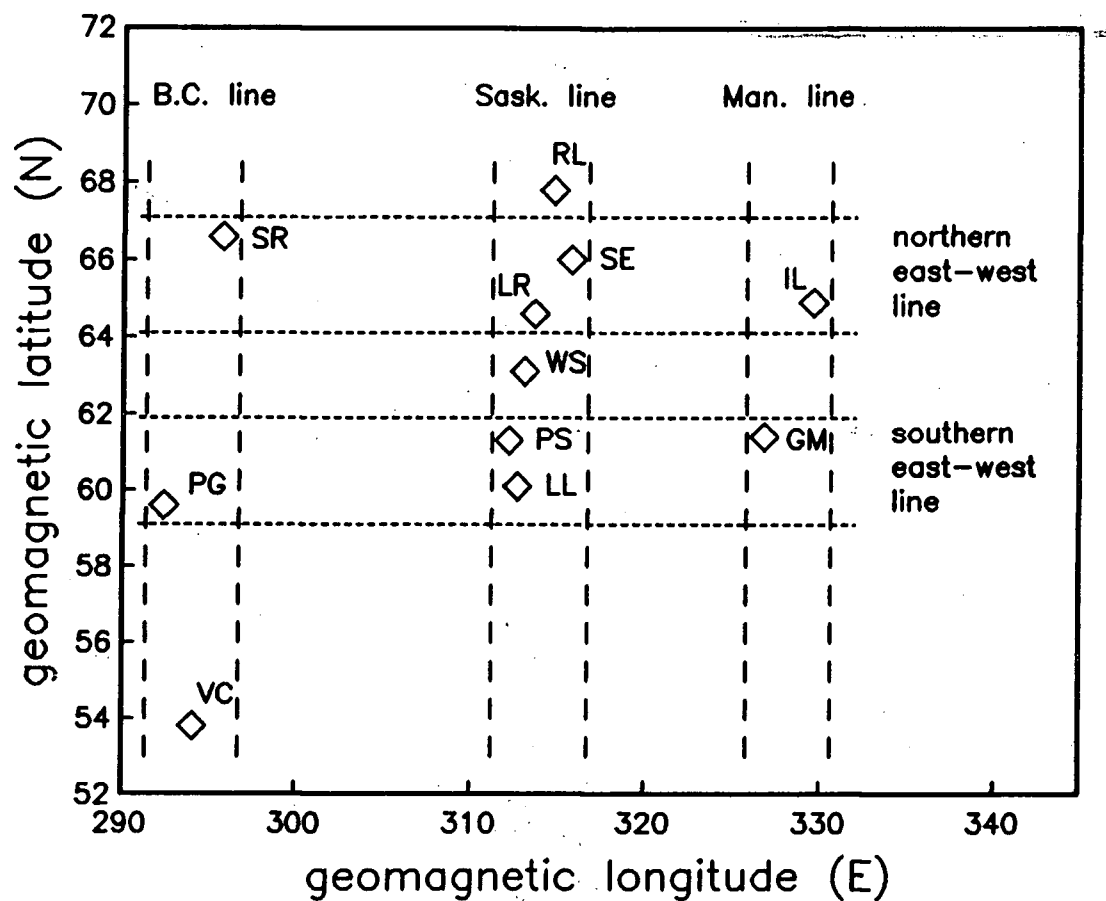


FIGURE 3.

Plot of ULF station locations, in geomagnetic coordinates, for the "Aurora-ULF-VLF" campaign. The north-south and east-west station lines are also shown.

IL, as well as a southern line of PG, PS and/or LL, and GM. The recording systems at these ground stations consisted of induction magnetometers with high- μ metal cores, amplifiers, and slow-speed FM analogue tape recorders. These systems were each capable of recording three orthogonal components: X (magnetic north), Y (magnetic east), and Z (downward). Further information on the campaign, including the recording systems used, can be obtained from Oguti et al. (1982).

The network of ULF stations was not without its problems. Depending on the recording system, narrow band instrument noise was present within the IPDP frequency band, at either 0.5 or 0.7 Hz. Man-made impulsive noise also interfered with some stations: traffic noise at GM, RL, PG, and SR; and radio transmissions at IL and PG. In addition, WS recorded broad band noise below 0.2 Hz which was attributed to lake oscillations. A more serious problem for the study of IPDPs proved to be missing data intervals. For example, at WS the X-component was not recorded at all, some of the tapes from PG and IL proved to be unreadable, and almost all stations suffered from incomplete coverage of the campaign period. With these difficulties, it was quite rare to have most of the stations operating properly at the time of an IPDP event, which limited the choice of events suitable for detailed analysis.

Altogether, ten IPDPs were recorded between Jan. 16 and

Feb. 24, 1980. These events are listed in Table IV. A book of dynamic spectra from the Aurora-ULF-VLF campaign (Oguti et al., 1982) was used to identify them. From these ten events, three were selected for detailed analysis. These three, Feb. 14, Feb. 15, and Feb. 24c, will be discussed extensively in Chapter Five. The criteria for selection of the above events included that they be recorded at more than one site on a north-south line and/or more than one site on an east-west line for analysis purposes (cf. Chapter Five), the quality of the data obtained, and the clarity of the IPDP, ensuring that the event was unambiguously identified as an IPDP.

Magnetograms from two geosynchronous satellites, GOES 2 and GOES 3, were also used. The magnetograms from both of these GOES satellites consist of 0000-2400 UT plots of three orthogonal components, H, D, and V, plus the total field strength, all being plotted in gammas. The GOES 2 satellite orbits near 251° E, and is thus close to the geomagnetic meridian of the Saskatchewan north-south line. During the campaign period, only twelve days of data are available from this satellite, from Feb. 5 to Feb. 16 inclusive. The GOES 3 satellite orbits near 225° E, close to the geomagnetic meridian of the B.C. north-south line. Magnetograms from this satellite are available for the entire campaign period.

The third data set required for the analysis of IPDPs

Table IV
IPDP Events

	<u>Event</u>	<u>UT</u>
1.	Jan. 16	0255 - 0315
2.	Jan. 23	0535 - 0635
3.	Jan. 27	2230 - 2320
4.	Jan. 28	0000 - 0105
5.	Jan. 29	0150 - 0315
<u>6.</u>	<u>Feb. 14</u>	<u>0835 - 0940</u>
<u>7.</u>	<u>Feb. 15</u>	<u>2145 - 2205</u>
8.	Feb. 24a	0000 - 0130
9.	Feb. 24b	0150 - 0300
<u>10.</u>	<u>Feb. 24c</u>	<u>0550 - 0650</u>

(Events selected for detailed analysis underlined.)

consists of magnetograms from an array of eight auroral and sub-auroral zone magnetic observatories (see Table V). These magnetograms were obtained from World Data Center A for solar-terrestrial physics in Boulder, Colorado (NOAA). The data are in the form of one-minute values given to the nearest gamma for the magnetic north, magnetic east, and vertical components, as well as for the total field strength.

The last two data sets used here are the Kp and Dst indices. Kp indices were available from World Data Center A for solar-terrestrial physics, and Dst indices from World Data Center A for rockets and satellites in Greenbelt, Maryland (NASA). These two indices are described in detail in Appendix C.

2.2. DATA PROCESSING

This section provides a description of analogue and digital processing techniques employed during the analysis of the IPDP data.

The first step in the analysis of an IPDP event, after its identification, is simply to look at it in the form of a high speed magnetogram or as a dynamic spectrum (spectrogram). This is necessary both to understand the gross properties of the event and to establish the parameters for later digitization and computer analysis.

Table V
Magnetic Observatory Coordinates

	<u>Geographic</u>		<u>Corrected</u> <u>Geomagnetic</u>	
	<u>Lat.(°N)</u>	<u>Long.(°E)</u>	<u>Lat.(°N)</u>	<u>Long.(°E)</u>
St. John's (STJ)	47.6	307.4	55.4	31.0
Ottawa (OTT)	45.4	284.5	57.2	359.2
Great Whale R. (GWR)	55.2	282.3	66.8	359.6
Whiteshell (WHS)	40.3	264.8	51.1	330.7
Fort Churchill (FC)	58.8	265.9	69.7	329.5
Meanook (ME)	54.6	246.7	62.4	303.4
Yellowknife (YEK)	62.4	245.6	69.8	297.4
Victoria (VC)	48.5	236.6	54.1	294.3

Each of these displays can be created from the analogue magnetic tapes; directly in the case of a magnetogram, and through a spectrum analyser (Nicolet 440B or Spectral Dynamics SD345) and fibre-optic oscillograph (Honeywell 1856A) for a dynamic spectrum.

The IPDP events chosen for detailed study required digitization prior to computer analysis. The analogue-to-digital conversion system consisted of an analogue tape drive, an analogue filter bank, and a Data Translation DT-2801-A A/D card dumping the digitized data directly onto an IBM PCAT computer. The sampling frequency was set at 3.75 Hz. Prior to digitization, 48 db/octave anti-aliasing filters with a corner frequency of 1.5 Hz were applied.

The digitized events are then subjected to detailed analysis in order to understand their frequency, amplitude, and polarization evolution. This analysis is carried out using programs for digital filtering, fast Fourier transforms (FFTs), and cross-correlations.

The FFT routine used for IPDP analysis here is a complex FFT routine from the Microway 87FFTTM package. As part of the pre-FFT processing, the data were filtered with a Butterworth band-pass filter (Kanasewich, 1981) to remove unwanted noise, especially at low frequencies, outside the IPDP's frequency range. The roll-off of this filter is 96

dB/octave.

The FFT method for detailed IPDP evolution analysis requires that the event be divided into a series of relatively short records, typically of 512 or 1024 points (2.27 or 4.55 minutes of data), each of which is then individually analysed. Within these short data segments the IPDP frequency is assumed to be constant for the purpose of applying an FFT. This assumption has been tested by the analysis of synthetic signals with frequencies increasing at rates similar to those encountered in IPDPs. For the segment lengths used, the FFT analysis of these signals reproduced their known amplitude and frequency characteristics very well, thus indicating that the assumption of constant frequency used here is reasonable. The frequency and amplitude evolution of an IPDP is then found from the spectra computed from the FFTs of a succession of consecutive data segments comprising the IPDP.

The polarization spectrograms, from which the evolution of an event's polarization is found, are obtained from the combined complex FFTs of coincident X and Y component data segments. Polarization spectrograms appear as normal power spectra, except that the data presented are for the given polarization component only. These spectrograms can be produced for right circular, left circular, and linear polarizations as shown below (Arnoldy et al., 1979). If F_j^x

and F_j^y are the Fourier transformed complex series of the X and Y data components

$$F_j = \sum_{k=0}^{N-1} f_j \exp[-i2\pi jk/N],$$

then the right and left circular polarization components can be represented as:

$$F_j^r = (F_j^x - i F_j^y) / \sqrt{2} \quad (2.1a)$$

for the right component, and as:

$$F_j^l = (F_j^x + i F_j^y) / \sqrt{2} \quad (2.1b)$$

for the left component. From these circular components, the polarization power spectra are calculated as follows:

$$P_j^c = |F_j^r|^2 - |F_j^l|^2 \quad (2.2)$$

where positive P_j^c represents power in the right circular component, and negative P_j^c in the left component. Linear polarization spectrograms are calculated from:

$$P_j^L = [(|F_j^r|^2 + |F_j^l|^2)^2 - |P_j^c|^2]^{\frac{1}{2}} \quad (2.3).$$

Finally, cross-correlations are used to compare recordings of an event taken simultaneously at different stations. To facilitate this, cross- and auto-correlation routines from the *Microway 87FFT*TM package were used.

In addition to the above signal processing techniques, some curve-fitting is also required for the IPDP analyses. The curve-fitting routine employed here, from the *Laboratory Technologies Inc.* NOTEBOOK software package, uses an iterative least-squares regression technique.

CHAPTER 3. PROPERTIES OF IPDPS

This chapter will review the physical and occurrence characteristics of IPDPS as observed by ground stations, and compare geosynchronous satellite observations to ground observations. In addition, IPDP relationships with other geomagnetic phenomena will be discussed.

3.1. PHYSICAL CHARACTERISTICS

IPDPS are broad-band events which exhibit a progressively rising mid-frequency throughout their lifetimes. Figure 4 shows a dynamic spectrum of a typical IPDP event.

Some of the basic physical properties of IPDPS, as seen from ground stations, have been summarized in Table VI. The parameters of most IPDPS will fall within the ranges given. However, in extreme conditions, some events will have some parameter values outside these ranges. Initial frequencies as low as 0.05 Hz, which is in the Pc 3 frequency range, have been recorded (Heacock, 1971). End frequencies of up to 2 Hz have also been observed, especially at lower latitudes. The change in frequency during the course of an event must be positive for the event to be identified as an IPDP. A typical increase in frequency would be greater than 1 octave, and sometimes as high as 3 octaves (Saito, 1969). Though the frequency slopes which different IPDP events can

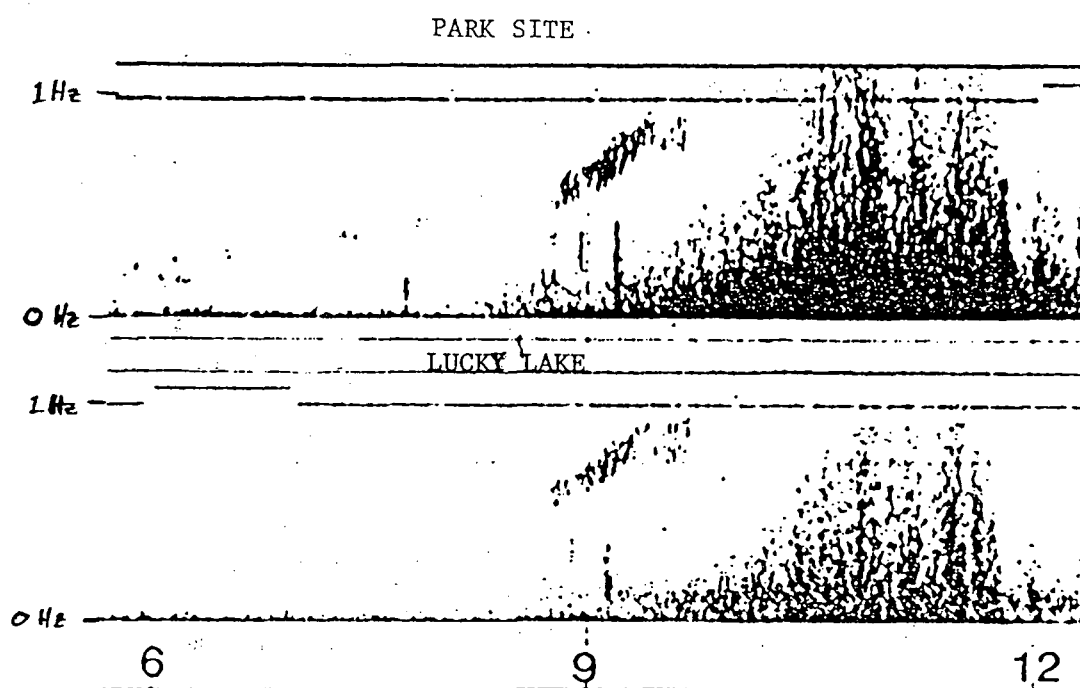


FIGURE 4.

Dynamic spectra of an IPDP recorded on Feb. 14, 1980 at Park Site and Lucky Lake, Saskatchewan. This event, which occurs near 0900UT, clearly shows the rising frequency trend typical of IPDPs.

Table VI
IPDP Physical Characteristics

Initial frequency (F_i)	0.1 - 0.3 Hz
End frequency (F_e)	0.5 - 1.0 Hz
Change in frequency ($F_e - F_i$)	0.2 - 0.7 Hz
Average slope ($(F_e - F_i)/T$)	0.2 - 1.0 Hz/h
Duration (T)	20 min - 2 h
Amplitude	0.01 - 1.0 γ

exhibit may be quite different, within an individual event they tend to be fairly constant. An average slope of 0.73 Hz/h was obtained by Heacock (1971) from 130 events, while Roxburgh (1970) found a typical slope to be 0.3 Hz/h. In extreme cases, the slope may be much larger than 1 Hz/h. For example, slopes of up to 5 Hz/h have been reported (Roxburgh, 1970). The width of the noise band of IPDPs is usually in the range of 0.1 - 0.3 Hz.

From a sample of 66 events, an average length for IPDPs of 39 minutes was found by Fukunishi et al. (1981). Most IPDP event durations exceed 20 minutes, though events longer than 2 hours are quite rare.

A mean amplitude of 0.1γ for IPDP events was given by Gendrin (1970). However, IPDPs often contain short, higher amplitude intervals as well. The chart recording in figure 5 shows an example of such an interval. These structured elements, as the high amplitude intervals are often called, tend to occur at randomly spaced intervals during the course of an IPDP event.

The polarization shown by IPDPs can be right-handed or left-handed elliptical, or linear. Arnoldy et al. (1979) reported a progression of first right-handed, then linear, then left-handed, then linear again, and lastly right-handed polarization again during the course of an IPDP event.

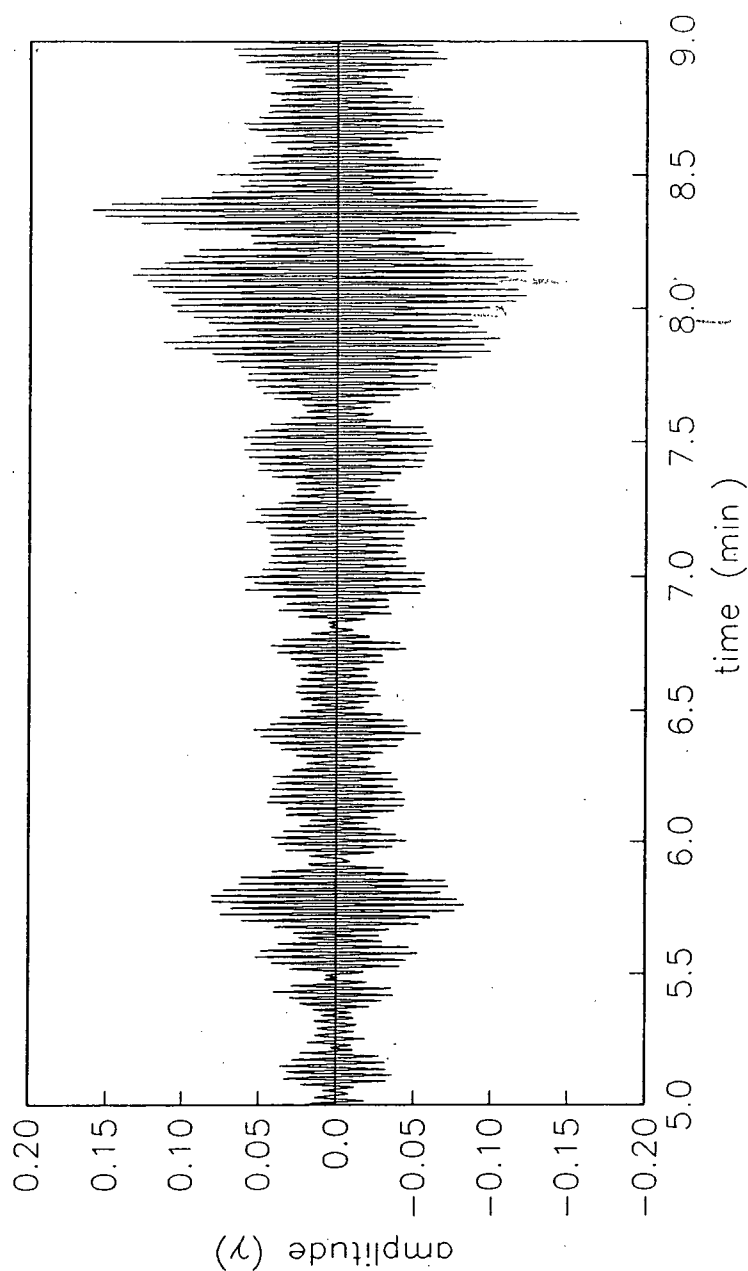


FIGURE 5.

Y component magnetogram of a part of an IPDP event (0905 - 0909 UT) recorded at Park Site, Sask. on Feb. 14, 1980. A 0.4 - 1.0 Hz bandpass filter has been applied to the data. Note the higher amplitude interval near 0908UT.

3.2. OCCURRENCE OF IPDPS

Table VII presents a brief summary of the occurrence characteristics of evening-side IPDPS. Morning-side IPDPS (Fukunishi and Toya, 1981; Dovbnya et al., 1984), which typically appear near 0500 geomagnetic local time (GMLT), are possibly a distinct class of micropulsation from evening-side IPDPS and are not considered in this thesis. As with Table VI, the values given here will be typical of most, but not all, IPDP events. IPDPS are strongly concentrated in the evening local time sector, with the peak in occurrence near 2000 GMLT as shown in figure 6. The heaviest concentration of events also occurs in the geomagnetic latitude (GM Lat.) range of 60° to 65° , the sub-auroral zone. Very few have been observed at latitudes higher than 70° . Below 50° GM Lat., IPDPS are also less common, reaching these latitudes only through ionospheric duct propagation (cf. Appendix B) or on days of very high magnetospheric activity. Most IPDPS occur on moderately active days ($20 < \Sigma Kp < 30$), though some are occasionally seen on relatively quiet days ($10 < \Sigma Kp < 20$). Heacock (1967) found a median value of 3- for the 3-hourly Kp index corresponding to an IPDP event's occurrence time. Figure 7 shows when IPDPS occurred on a Kp versus time plot covering $2\frac{1}{2}$ months (Gendrin, 1970). Heacock (1967) also found that IPDPS occurred at the rate of approximately 12 per quarter,

Table VIIIPDP Occurrence Characteristics

Local time	1600 - 0100 GMLT
Latitude	55° - 65° GM Lat.
$\Sigma_{24hr} Kp$	20 - 35
3-hourly Kp	1 - 5

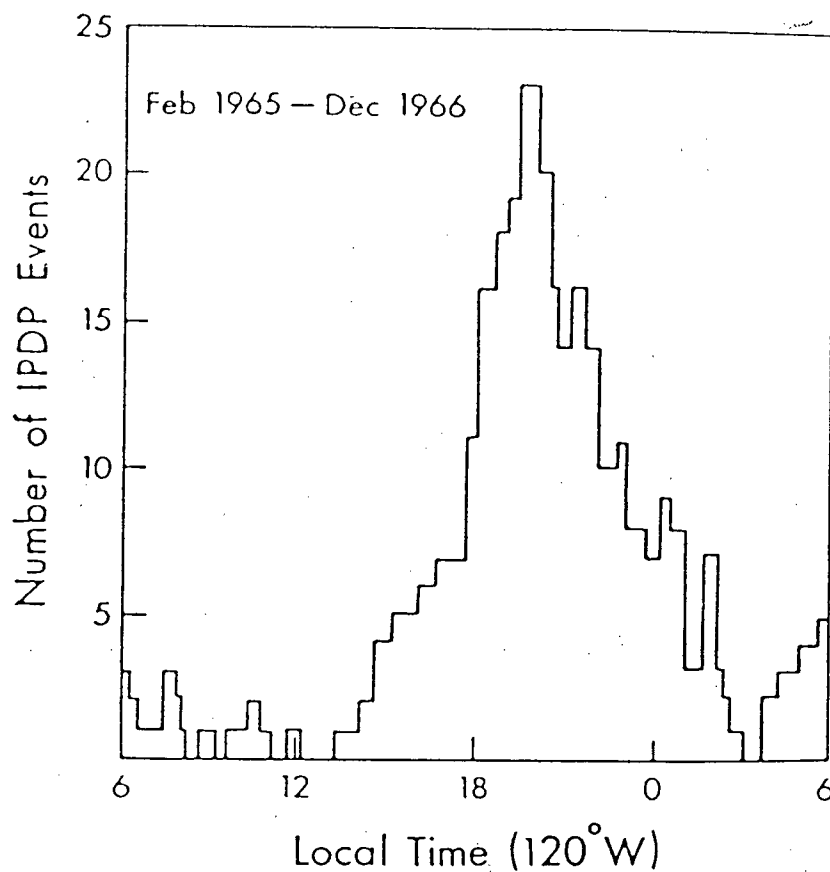


FIGURE 6.

Diurnal distribution of the occurrence of IPDPs, showing the peak in occurrence in the evening hours. These data were collected at Seattle, Wash. (GM Lat. $\approx 53^\circ$) by Knafllich and Kenney (1967).

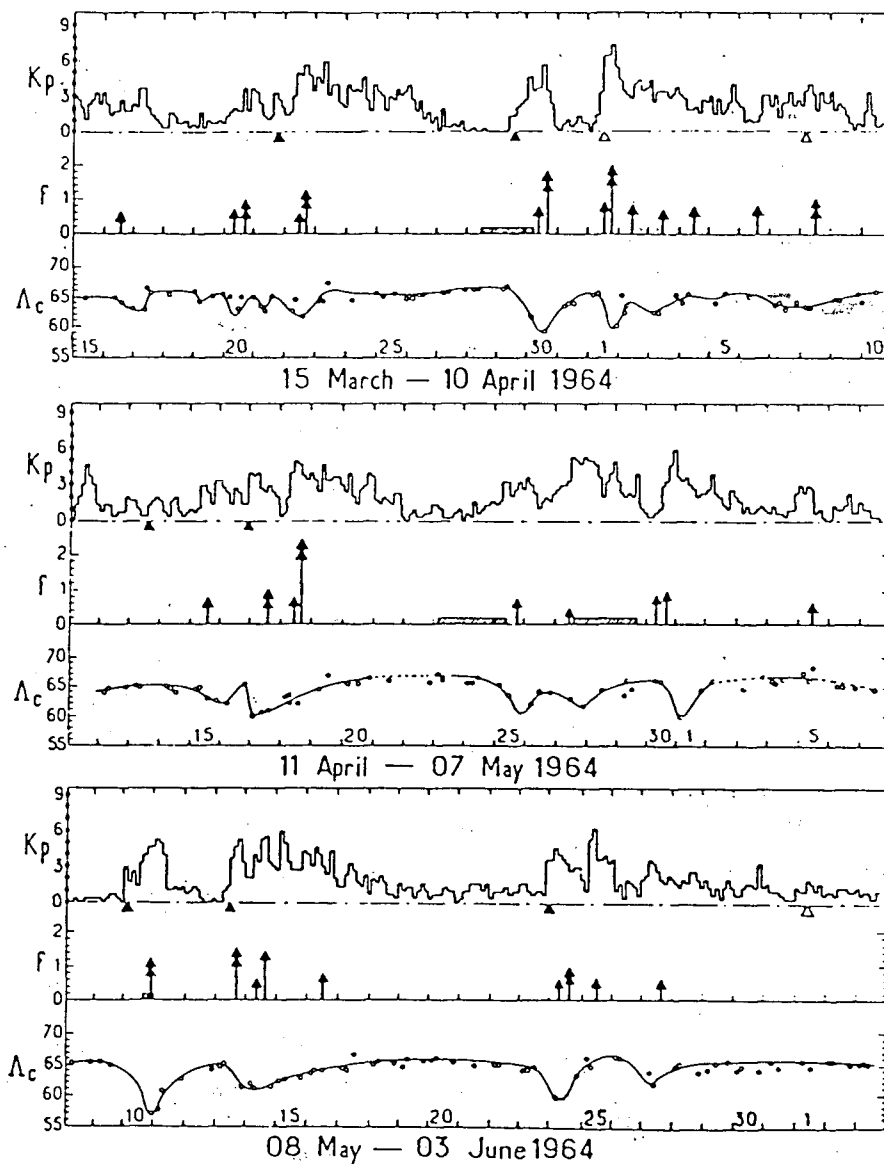


FIGURE 7.

Occurrence of IPDPs versus Kp index (Gendrin, 1970). The vertical arrows in the central panels indicate IPDPs, which tend to occur in more active times (higher Kp).

increasing to several dozen per quarter in the summer. Fukunishi et al. (1981) obtained the somewhat lower rate of 66 events in 25 months at Syowa Station, Antarctica (GM Lat. = -65.9°).

As indicated above, on days of high magnetospheric activity IPDPs are observed at lower latitudes, while high latitude stations detect nothing. These lower latitude events tend to exhibit higher frequencies than the high latitude IPDPs. According to Soraas et al. (1980), the low latitude, high Kp events also tend to occur at earlier local times, though, for constant Kp, the maximum occurrence rate is at an earlier GMLT for high latitude IPDPs. Heacock et al. (1976) found the diurnal peak to be near 1700 GMLT for College, Alaska (64.5° GM Lat.) and near 2000 GMLT for Palo Alto, California. (43.5° GM Lat.). Other latitude effects that have been noted include 0.1γ amplitudes at lower latitudes versus 1γ amplitudes at high latitudes (Heacock, 1967) as well as lower frequency slopes at high latitudes (Pikkarainen et al., 1983).

Heacock (1971) found that IPDP slope varies with GMLT, determining an average slope of 0.55 Hz/h from a set of 63 IPDPs occurring in the 1200 to 1600 GMLT sector, and an average slope of 0.91 Hz/h from 67 events occurring in the 1700 to 2300 GMLT sector. However, Roxburgh (1970) claimed to find no correlation between slope and GMLT. Heacock et

al. (1976) also compared the slopes of IPDPs to the AE index for late-evening sector events, finding that high AE correlated with high slopes and low AE with low slopes. These correlations were not evident in the afternoon sector. Note that both the Kp and AE indices are described in Appendix C.

Various studies comparing IPDPs recorded at geomagnetically conjugate stations have been conducted. Gendrin et al. (1966) reported that IPDP structured elements, or high amplitude intervals, appeared simultaneously at conjugate stations and with the same polarization, that is, both displaying the same sense of magnetic vector rotation at one time. Both these characteristics are opposite those shown by structured Pc 1 (pearls), whose elements appear alternately and with opposite senses of vector rotation at conjugate stations. Arnoldy et al. (1979) found that an IPDP recorded at Siple, Antarctica, and Roberval, Quebec, showed neither left-hand polarization nor cosmic noise absorption which accompanies left-hand polarization (cf. sec. 3.5) simultaneously at each site even though Roberval is only 40km from Siple's conjugate point. This indicates that care must be taken in interpreting "conjugate" point polarization observations. Heacock et al. (1976) found that in virtually all cases IPDPs recorded at one site were also seen at the conjugate

site, and exhibited the same frequency slope at both sites. It was also found, however, that the occurrence of structured elements within an IPDP were uncorrelated between the conjugate sites, which is in contrast to the result mentioned above. It must be noted that, with respect to both polarization and element occurrence, there appears to be some uncertainty in IPDP properties.

3.3. NETWORK OBSERVATIONS

Networks of ground stations have often been employed to study IPDP events. These networks have generally consisted of north - south lines of stations (Lukkari et al., 1977; Maltseva et al., 1981; Pikkarainen et al., 1983; Maltseva et al., 1985; Pikkarainen et al., 1986), and/or east - west station arrays (Maltseva et al., 1970; Heacock, 1973; Soraas et al., 1980; Pikkarainen et al., 1983).

Magnetograms and spectrograms of an IPDP event recorded at stations in a north - south line generally have similar appearances at each site. Ionospheric ducting of IPDP signals causes an event recorded simultaneously at latitudinally separated stations to show the same frequency, slope, duration, and structured elements at each location. The amplitude of an IPDP, however, will vary along a north - south line of stations, with the location of the peak amplitude moving southward during the event (among others;

Lukkari et al., 1977, Maltseva et al., 1981, Pikkarainen et al., 1986). Figure 8 shows simultaneous chart records of an IPDP obtained from two of the stations of the Saskatchewan north - south chain (PS and LL) separated by 1.2° of latitude, demonstrating the similarity of signals from co-meridional stations.

Somewhat less attention has been paid to simultaneous observations of IPDPs at stations separated in longitude. The studies that have been done indicate that the longitudinal range of IPDP events can vary widely; Soraas et al. (1980) found events covering more than 140° geomagnetic longitude (GM Long.) are rare, while 30% of the events observed spanned less than 60° GM Longitude. Though Pikkarainen et al. (1983) commented that no drastic changes in IPDP frequency - time characteristics are necessarily observed over the 100° longitude range of an event and Soraas et al. (1980) found that IPDPs can be quite similar over ranges of less than 60° GM Long., it is nevertheless clear that some longitudinal differences do exist within an IPDP event as seen on an east - west chain of stations. Maltseva et al. (1970) found that both the frequency and slope of IPDPs tends to be higher towards the east, that is, towards midnight. While Heacock (1973) could not confirm the trend for IPDP slopes, it was noted that a delay in onset times to the west of 15 minutes to 1 hour was often seen

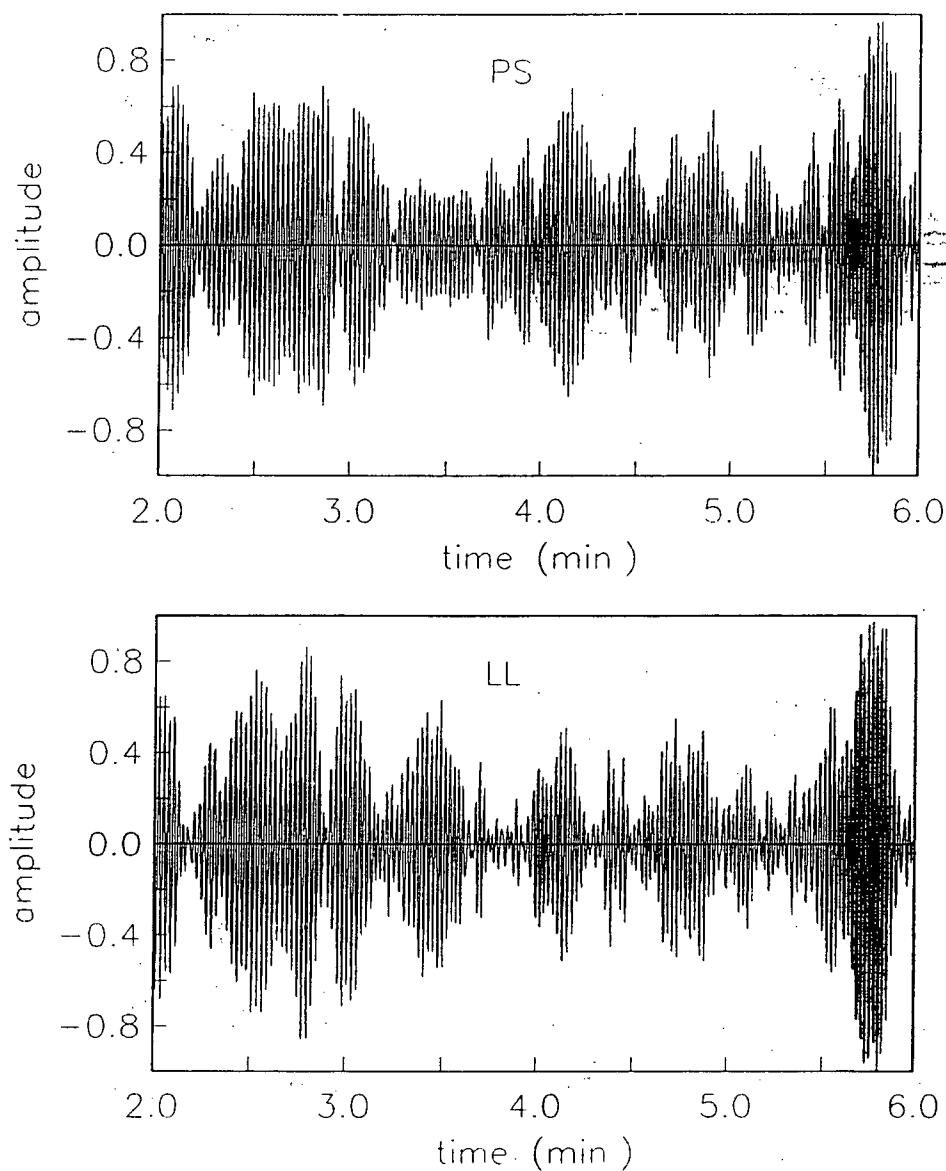


FIGURE 8.

Comparison of Y component record segments (0902 to 0906 UT) from two stations on the same meridian (Park Site, 312.2° E, and Lucky Lake, 312.7° E), Feb. 14 event. Each segment has been normalized and a 0.4 - 1.0 Hz bandpass filter has been applied. Note the similarity in the signals between these two stations.

between Meanook and College, 44.5° west (towards dusk) of Meanook. Pikkarainen et al. (1983) obtained a much faster onset drift of $5^\circ - 6^\circ/\text{min}$ to the west from 23 events. Three of these 23 events were also examined in detail, with all three showing longer durations towards the west and less intense low frequencies towards the east. Two of the events displayed no change in slope with longitude, while the third exhibited lower slopes towards the west. Figure 9 shows simultaneous chart records of an IPDP from two sites in the southern east - west line (PG and PS). Here, the signals do not show the same degree of similarity as those in figure 8. The stations are separated by 19.8° GM Longitude.

3.4. SATELLITE OBSERVATIONS

IPDPs have been studied from geosynchronous satellites by Bossen et al. (1976), using ATS-1 data, and McPherron (1981), using ATS-6 data. Almost all events seen at geosynchronous orbit are also seen at a ground station near the foot of the satellite's field line. For these IPDPs, the frequency spectrum seen at the satellite is narrower than that on the ground, but is contained within the same range. Satellites also observe smaller changes in frequency and shorter durations than ground stations for IPDP events (cf. fig. 10). These differences are likely due to ionospheric ducting of the ground-recorded signals (cf. Appendix B).

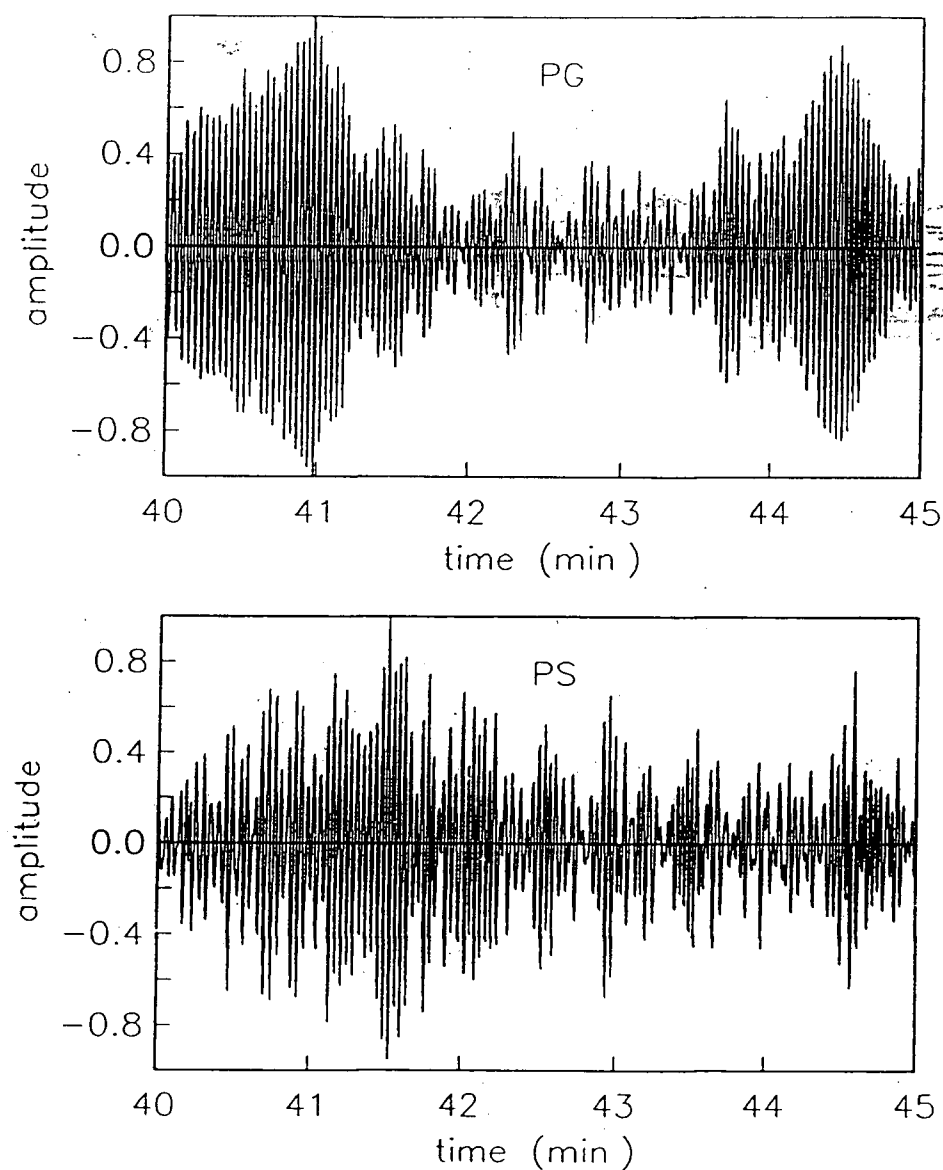


FIGURE 9.

Comparison of Y component record segments (0641 to 0646 UT) from two stations near the same parallel (Park Site, 61.3° N, and Prince George, 59.6° N), Feb. 24c event. Each segment has been normalized and a 0.2 - 0.6 Hz bandpass filter has been applied. These longitudinally separated stations exhibit quite different IPDP signals.

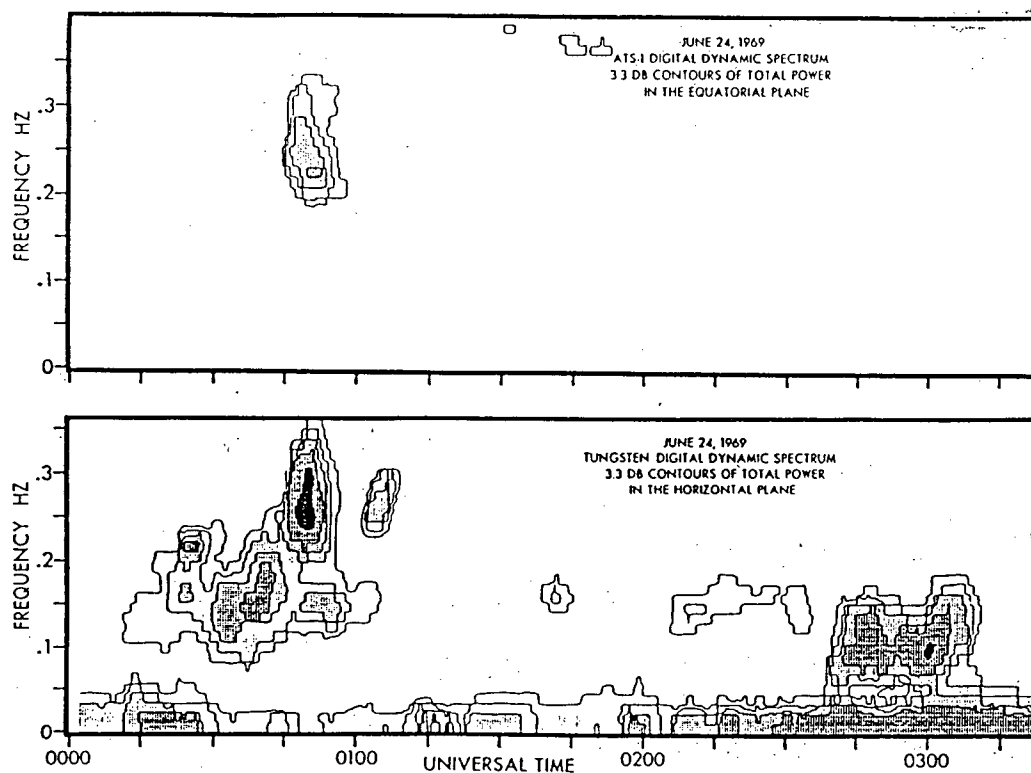


FIGURE 10.

Comparison of spectra from an IPDP recorded simultaneously by satellite (ATS-1) and at a ground station (Tungsten, NWT.) (Bossen et al., 1976). Note the shorter event duration and smaller frequency rise seen by the satellite.

Amplitudes of about 5γ have been recorded in orbit, which is approximately 50 times greater than a typical ground station amplitude. The polarizations observed at these satellites are left-handed elliptical, and at ATS-6, which is 10° above the magnetic equator, IPDP waves are always observed propagating away from the equator.

3.5. RELATION TO GEOMAGNETIC PHENOMENA

It is well established that IPDPs occur in active periods following storm sudden commencements. In particular, they are always associated with magnetospheric substorms, occurring in the expansion and recovery phases (Heacock et al., 1976). The onset of the expansion phase is seen on the ground as a sharp negative bay in the X component at high latitude stations near midnight. In the dusk sector, the X component often exhibits high latitude positive bays during a substorm expansion phase. IPDPs can occur in the afternoon or evening sectors following, usually within an hour, the onset of a sharp negative bay near midnight. The delay time is generally longer for IPDPs occurring at earlier local times, and it has been found that the slope of an event tends to decrease as this delay time increases (Fukunishi, 1969). IPDPs are also known to occur in conjunction with the dusk sector high latitude positive bays. During a substorm expansion phase, satellites in geosynchronous orbit observe

a depression in the magnetic field strength, followed by a recovery. Although Roxburgh (1970) found that IPDPs occurred during this recovery phase, the results of Bossen et al. (1976) indicated that 83% of the 33 events studied occurred when the magnetic field at geosynchronous orbit was either decreasing or constant.

Proton precipitation and associated proton aurora have been observed with IPDP events (Fukunishi, 1973), as has cosmic noise absorption (CNA). Note, however, that CNA is most likely not caused by precipitating protons, but rather by increased ionization in the ionosphere caused by precipitating protons (Fukunishi, 1973), or by relativistic electrons precipitated by parasitic interactions between IPDP waves and these electrons (Thorne and Kennel, 1971; Thorne and Larsen, 1976). Arnoldy et al. (1979) found that the left-hand polarized phase of IPDPs was correlated with the occurrence of CNA, particle precipitation, and auroral light. In addition to visual aurora, IPDPs have been associated with the auroral sporadic E-layer and auroral X-ray bursts.

IPDPs have also been associated with other types of micropulsations. Heacock (1967) reported that 4-second band pulsations sometimes terminate in IPDPs, and Roxburgh (1970) found that occasionally hm emissions immediately follow IPDP events. Maltseva et al. (1981) reported observations of Pc

4-5 pulsations at geosynchronous orbit only while IPDPs were seen on the ground. Pi bursts (Pi 1) were studied in conjunction with IPDPs by Heacock (1971). It was noted that Pi bursts occur before and towards midnight of almost all IPDPs. They appear at higher latitudes than IPDPs, and are accompanied by large scale particle precipitation into the ionosphere.

CHAPTER 4. MAGNETOSPHERIC MODEL OF IPDP GENERATION

It is now generally accepted that IPDP micropulsations are produced by an ion-cyclotron instability involving left-hand polarized waves and westward drifting particles injected into the inner magnetosphere from the magnetotail during magnetospheric substorms (Horita et al., 1979; Pikkarainen et al., 1983). However, not all the aspects of this process are completely understood, this being especially true of the mechanism(s) responsible for the rising frequency trend exhibited by IPDPs. In this chapter, the magnetospheric processes responsible for the appearance of IPDPs are described (section 4.1), followed by a description and discussion of the frequency shift mechanisms (sections 4.2 and 4.3). Lastly, the processes described in sections 4.1 through 4.3 are examined using a simple computer simulation of IPDP frequency behaviour (section 4.4).

4.1. IPDP - SUBSTORM MODEL

At the onset of a magnetospheric substorm, hot particles, which may eventually become involved in IPDP generation, are injected from the plasma sheet in towards the night side of the Earth. This injection is driven by the substorm associated intensified westward electric field. Though the plasma heating mechanism responsible for the high

particle energies is not yet well understood, it is likely related to the reconnection process occurring in the magnetotail at magnetospheric substorm onset (Nishida, 1978). Some of the particles involved in the injection precipitate directly into the ionosphere near midnight at high latitudes. This is most likely the precipitation observed in conjunction with the Pi bursts, which are often seen near midnight preceeding IPDPs (cf. section 3.5).

A sharp inner boundary of the injected particles has been observed or inferred by some authors (Mauk and McIlwain, 1974; McIlwain, 1974; Mauk and Meng, 1983). If direct observation of this boundary is not possible, its original position can be calculated by backtracking the drift motions of the particles from where they were detected by satellite. Such calculations result in the identification of a sharply defined spiral or double spiral shaped boundary, as shown in figure 11 (double spiral) and figure 12 (single spiral). These boundaries are closest to Earth just after midnight, with the cusp of a double - spiral boundary usually falling near 0100-0200 GMLT. Single spiral boundaries, which almost always spiral out westward towards dusk, can have their closest point as far eastward (towards morning) as 0300-0400 GMLT. Note that before drift motions and particle precipitation disturb the injected plasma, particles of all energies and pitch angles are present

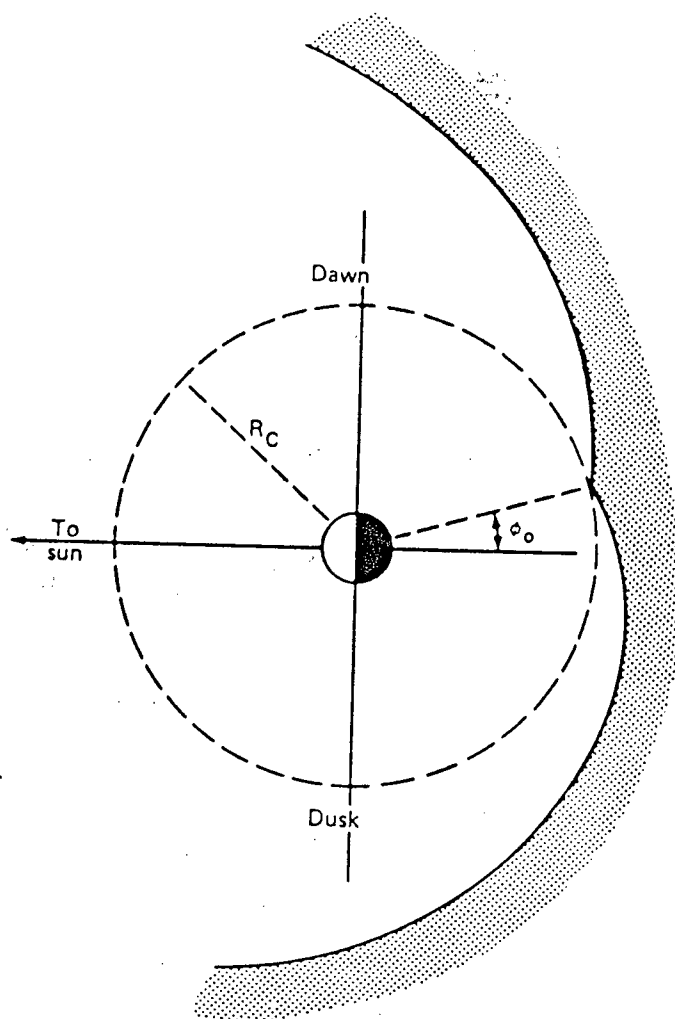


FIGURE 11.

Diagram of a double-spiral injection boundary (Mauk and Meng, 1983).

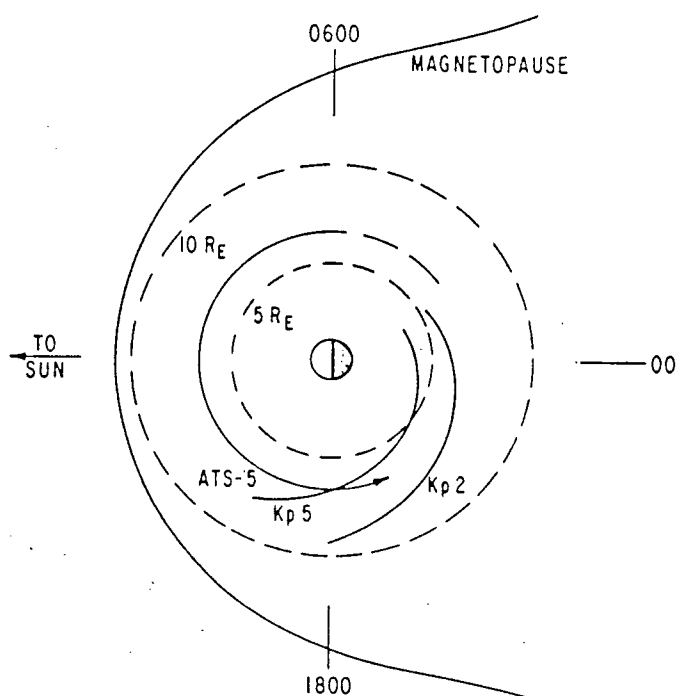


FIGURE 12.

Westward single-spiral injection boundary (Mauk and McIlwain, 1974). Note the boundary position variation with magnetospheric activity (Kp): inner boundary, Kp = 5; outer boundary, Kp = 2.

together.

It has been found that the position of the injection boundary is dependent on the level of magnetospheric activity (Kp), with the boundary occurring further inward during more active times, as illustrated in figure 12. Mauk and McIlwain (1974) have presented a formula relating boundary position to Kp and GMLT for a single westward spiral boundary:

$$L_b = \frac{122 - 10Kp}{GMLT - 7.3} \quad (4.1)$$

where L_b is the L shell of the boundary ($L = [\text{distance from center of Earth}]/[\text{radius of Earth}]$) and Kp is the "instantaneous" Kp value. Note that in equation 4.1, GMLT, which is expressed in hours, is actually equal to GMLT + 2400 after midnight (i.e. 0100 becomes 2500).

Arnoldy and Moore (1983) have suggested also that the boundary forms first near midnight, then expands continuously to the west forming a single spiral, or both to the east and to the west forming a double spiral. Their studies indicate that it takes approximately 10 to 15 minutes for the entire injection boundary to form, with the formation proceeding more quickly near midnight than to the west or east.

Immediately after the hot protons are injected into the inner magnetosphere, they begin to drift westward under the influence of the gradient and curvature of the geomagnetic field. The gradient drift velocity is given by (Jackson, 1975):

$$\bar{v}_g = \frac{v_{\perp}^2}{2\omega} \left[\frac{\bar{B} \times \bar{\nabla}_{\perp} B}{B^2} \right] \quad (4.2a)$$

and the curvature drift velocity by:

$$\bar{v}_c = \frac{v_{\parallel}^2}{\omega R} \left[\frac{\bar{R} \times \bar{B}}{RB} \right] \quad (4.2b)$$

where v_{\perp} and v_{\parallel} are the particle velocities perpendicular and parallel to the magnetic field B . \bar{R} is the radius vector from the effective center of curvature to the field line and ω is the particle gyrofrequency. From Jackson (1975), and using $\omega = qB/mc$, $R = r_E/3$ at equator of a dipole field (r_E is distance from center of Earth), and $B = B_{eq}/L^3$ (B_{eq} is field strength on Earth's surface at the equator), equations 4.2a and 4.2b above can be combined to give a total drift velocity of:

$$v_d = \frac{3Wc(1 + \cos^2 a)L^2}{qR_E B_{eq}} \quad (4.3)$$

where W is the total particle kinetic energy, a is the pitch angle, R_E is the radius of the Earth, and c is the speed of light. Note that since ω is positive because q is positive for protons, the drift velocity is directed westward. It is apparent from this equation that the drift velocity increases with particle energy and with distance from Earth (increasing L).

The energy dependence of v_d indicates that a satellite in the evening sector should see a softening proton energy spectrum as progressively slower, lower energy particles are encountered during the westward drift. This effect, which is more pronounced in the dusk region further from the injection boundary is well supported by observation (McIlwain, 1974; Horita et al., 1979; Mauk and Meng, 1983). The duration of IPDPs is also well matched by the duration of the enhanced flux of westward drifting protons as measured by satellite (Soraas et al., 1980). Though the pitch angle distribution at injection is virtually isotropic, leading to large scale precipitation into the ionosphere at higher latitudes, inside and towards dusk of the injection boundary the westward drifting protons show an

highly anisotropic distribution with an almost empty loss cone (Williams and Lyons, 1974a,b) (see fig. 13).

Though there is a strong dawn to dusk electric field across the magnetotail during substorms, this does not seem to affect the drift motions of high energy particles inside the plasma sheet inner edge. This is primarily due to the formation of the Alfvén layer, a layer having a net positive charge on the evening side and a net negative charge on the morning side, which is created by the differential drift motions of protons and electrons in the inner magnetosphere. The polarization electric field produced by these charged layers is directed dusk to dawn, opposite the tail field, and significantly reduces the net electric field inside the Alfvén layer (Nishida, 1978). Thus, for higher energy protons above a few keV which are responsible for IPDP generation, the electric field effects on drift motion are negligible and the drift paths are circular. Lower energy particles will undergo $\vec{E} \times \vec{B}$ drift as well as gradient and curvature drifts, with the electric field effects becoming dominant at energies of less than one keV (Nishida, 1982). Satellite observations of spatial proton energy dispersion patterns also show that the electric field component of the drift velocity must be quite small for high energy protons (McIlwain, 1974; Mauk and Meng, 1983).

This polarization electric field is also believed to be

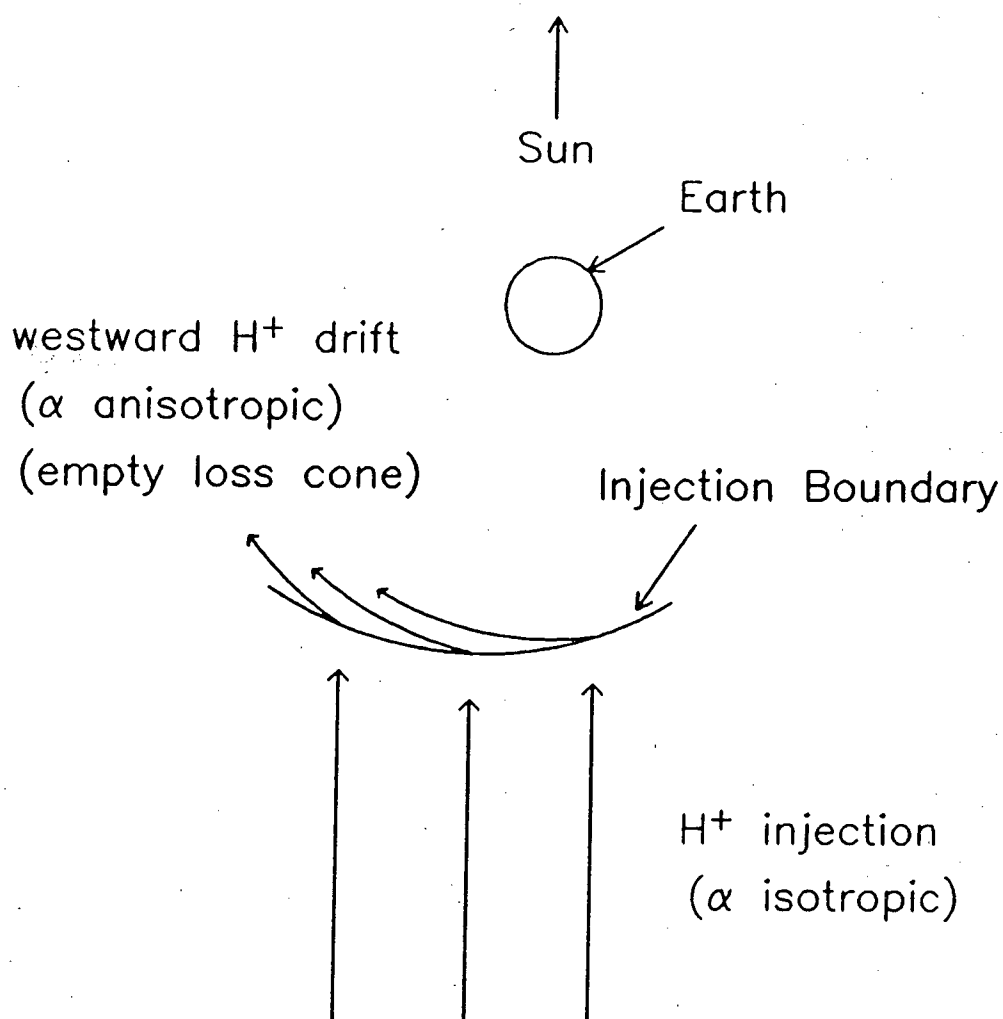


FIGURE 13.

Proton injection and westward drift trajectories during a substorm. Note the different pitch angle (α) distributions present during the injection and westward drift phases.

responsible for driving the eastward electrojet which is sometimes, though not always, observed with ionospheric substorms (Nishida, 1978; Boteler, 1980). This electrojet creates the dusk sector positive bays seen with IPDPs (cf. section 3.5), and is connected to the partial ring current produced by the westward proton drift by an inward field aligned current (see fig. 14). It is noteworthy that neither IPDPs nor the eastward electrojet - partial ring current system appear with every substorm. This may be due to the fact that weak substorms have weak injections that do not penetrate deeply into the inner magnetosphere, thus depriving both IPDPs and the partial ring current of their sources.

As the hot protons continue their westward drift, those on lower L shells will eventually meet the plasmapause, which is a region of steep gradients in cold plasma density separating the high density trapped cold plasma inside the plasmapause from the much lower density plasmas outside of it. It is here that the drifting protons undergo the ion-cyclotron instability which transfers particle energy to wave energy, thus generating an IPDP event. The instability occurs when a wave with IPDP frequencies, whose propagation vector is oppositely directed to the particle velocity parallel to the background magnetic field, has its frequency doppler shifted in the proton rest frame to match the

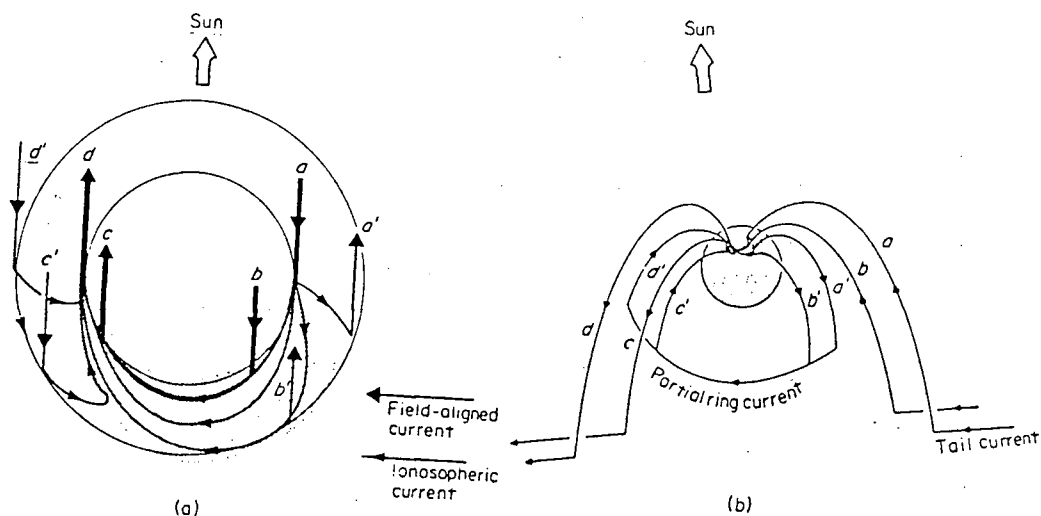


FIGURE 14.

Magnetospheric and ionospheric substorm current systems. The system features relating to IPDP occurrence are the partial ring current and the downward field-aligned currents labelled c' and d' which feed the eastward electrojet (Kamide et al., 1976).

proton's gyrofrequency. The opposed directions of travel mean that only left-hand polarized waves can interact with the protons since the direction of rotation of the wave field must coincide with the direction of proton gyration about the magnetic field lines. The above implies that the wave frequency, ω , must be less than the proton gyrofrequency, Ω_p , which is as observed (typically $\omega \sim 0.1 \Omega_p$).

The instability occurs preferentially at the plasmopause because of its sharply increasing cold plasma density (n_c). Cornwall et al. (1970) and Perraut et al. (1976) calculated that the peak growth rate of ion-cyclotron waves (ICW) is just inside the plasmopause, and Gomberoff and Cuperman (1982) have shown that the growth of ICW increases as n_c/n_w increases, which occurs as the plasmopause is crossed, until n_c/n_w reaches an optimum value, and then growth decreases again. The plasmopause as the IPDP generation location is also supported by observation (Horita et al., 1979).

The growth of ICW depends critically on the anisotropy (A) in the hot proton distribution as well as on n_c . Gendrin et al. (1971) have shown that $A > 1/[(\Omega_p/\omega)-1]$, where Ω_p = proton gyrofrequency and $A = [T_{\perp}/T_{\parallel}] - 1$, for ICW to grow. Here, T_{\perp} and T_{\parallel} are defined as $T_{\perp} = m_p \langle v_{\perp}^2 \rangle / (2k)$ and $T_{\parallel} = m_p \langle v_{\parallel}^2 \rangle / k$ where m_p is the proton mass, $\langle v_{\perp}^2 \rangle$ and $\langle v_{\parallel}^2 \rangle$

are the averages of the squares of the speeds perpendicular and parallel to the magnetic field, and κ is Boltzmann's constant. For $\Omega_p/\omega = 10$, this means A must be greater than 0.11. The hot proton pitch angle distribution will have become anisotropic (i.e. $A > 0$) during the westward drift. However, given the very low n_c found outside the plasmopause, A does not become large enough for the ion-cyclotron instability to occur in this region. This is confirmed by Cornwall and Schulz (1971), who found that, outside the plasmopause, the storm-time ring current is stable with respect to the ion-cyclotron instability. It is not until the plasmopause is reached that both the anisotropy and n_c favour wave growth. Once inside the plasmopause, however, wave growth again decreases due to electron-ion collisions (Cornwall et al., 1970) and an altered hot proton population. Since the instability process takes the particle energy from v_{\perp} , it also reduces A since T_{\perp}/T_{\parallel} is reduced. This has the effect of scattering protons into the previously empty loss cone of their pitch angle distribution, resulting in a loss of particles to the ionosphere. The lowered A and n_w then result in a decreased wave growth inside the plasmopause.

After amplification, the ICW propagate down field lines towards Earth's surface. Similarities in occurrence times and dynamic spectra of IPDPs as recorded at conjugate

stations in the northern and southern hemispheres, and as observed by satellites and ground stations near the same field lines, provide strong evidence for such field line guiding (cf. sections 3.2 and 3.4). The correlations of proton precipitation and CNA with the left-hand polarized waves (cf. section 3.5), which arrive at the ionosphere directly overhead of a ground station, provide further confirmation of field line guiding of the waves. This proton precipitation represents at least a portion of the downward field aligned current connecting the partial ring current and the eastward electrojet mentioned earlier. The observation that the waves always propagate away from the equator (cf. section 3.4) also indicates that amplification of the ICW takes place primarily in the equatorial region.

The shape of the plasmopause exerts strong control over where and when IPDPs appear. Figure 15 shows three estimates of the averaged plasmopause configuration. The westward proton drift from the midnight region and the dusk sector bulge in the plasmopause account for the observation that IPDPs occur predominantly in the evening sector (cf. section 3.2). This also controls the longitudinal extent of individual IPDPs (cf. section 3.3). As well, the equatorial plasmopause distance controls the latitudes of peak IPDP observation by ground stations. The plasmopause shape provides an obvious latitude GMLT correlation in IPDP

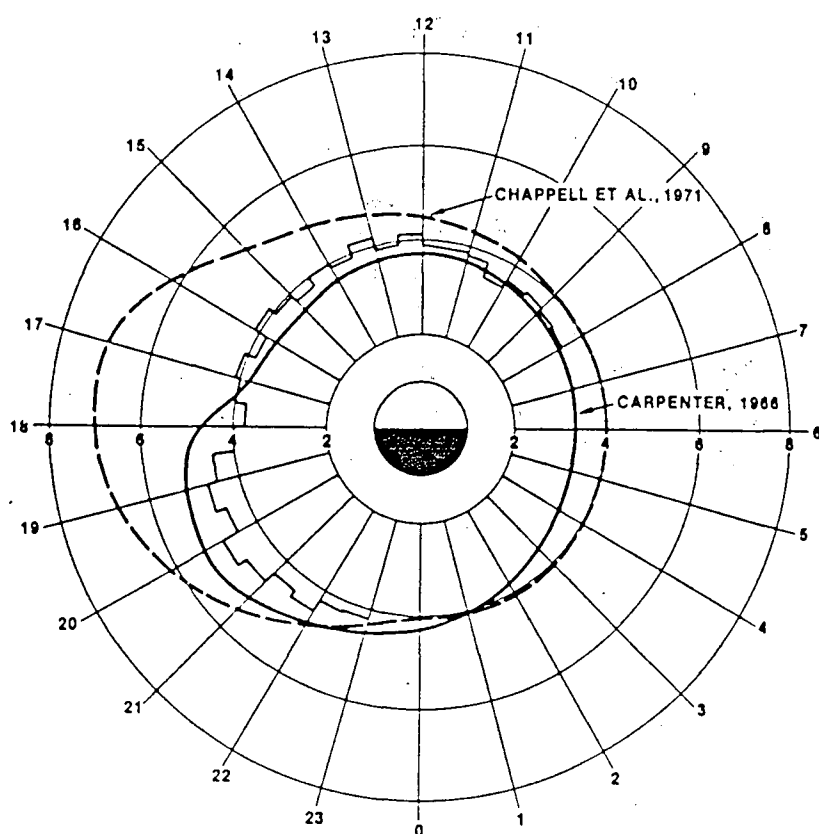


FIGURE 15.

Three average plasmapause L versus LT profiles as determined from whistler observations (Carpenter, 1966), Ogo 5 ion mass spectrometer data (Chappell et al., 1971), and Explorer 45 dc probe data (histogram) (Maynard and Grebowsky, 1977). Note the increased plasmapause radius near 1800 LT which is termed the dusk sector bulge.

occurrence, with higher latitude events tending to occur at earlier GMLT. Since the plasmapause radius shrinks with higher magnetospheric activity there is also a latitude Kp correlation, with higher latitude events occurring when Kp is lower (cf. section 3.2). Note that these observed occurrence characteristics and correlations also provide confirmation that IPDPs are generated at the plasmapause.

4.2. IPDP FREQUENCY SHIFT MECHANISMS

The preceding section has described the general generation processes which create IPDPs, excepting those which produce the characteristic frequency rise. In this section, three mechanisms which have been proposed to account for the IPDP frequency shift are reviewed.

The primary factors controlling the frequency change of the ion-cyclotron resonance generating IPDPs are the strength of the background magnetic field in the generation region and the energy of the hot resonating protons. In Appendix A (equation A.4b), it is shown that the frequency (f) varies with these parameters as:

$$f \propto \frac{B^{1.5}}{W^{0.5}} \quad (4.4).$$

The rising tone of IPDPs can therefore be caused by an

increasing magnetic field B , or a decreasing proton energy W . Below, two processes that result in increasing B , inward motion and increasing background field, and one resulting in decreasing W , azimuthal drift, are discussed.

4.2.1. Inward Motion

Inward motion of the IPDP generation region from higher L shells in towards the Earth, and thus to regions of higher magnetic field strength, was among the first mechanisms proposed to account for the frequency rise of IPDPs (Gendrin et al., 1967; Heacock, 1967). This inward motion was believed to involve the diffusion inward across field lines in the premidnight - dusk sector of an hot proton cloud in which the ion-cyclotron instability occurred. The diffusion was thought to be driven by a westward electric field (Troitskaya et al., 1968).

Roxburgh (1970) noted, however, that the inward diffusion velocities ($\approx 6\text{km/s}$) and electric fields ($\approx 6\text{kV}/R_E$) necessary for this mechanism to operate are not observed in the IPDP generation region. There is, though, a way to move the generation region to lower L shells without requiring a cross L drift of the hot protons during the event. As discussed in section 4.1, IPDP generation occurs at the plasmopause after a westward drift, in circular orbits, of the hot protons. The radial position of the generation

region is then controlled by the plasmopause position above, that is, in the same meridian as, the ground station recording the event. If the plasmopause moves inward, as is observed to happen during magnetospheric storms, then the generation region will also move inward, resulting in the westward drifting protons meeting the plasmopause at successively lower L shells in the meridian of the ground station, and causing the IPDP emission frequency to rise (Heacock, 1971; Horita et al., 1979).

If it is assumed that Earth's magnetic field is approximately dipolar ($B \propto L^{-3}$) at these small radial distances, and also that W is assumed to be constant in order to isolate the effects of the inward motion related magnetic field changes, then equation 4.4 becomes:

$$\frac{f_f}{f_i} = \left[\frac{L_i}{L_f} \right]^{4.5} \quad (4.5)$$

where X_i and X_f are, respectively, the initial and final values for each quantity. Note that the strong dependence of f on L (power of 4.5) indicates that a relatively small change in L can produce a significant frequency rise.

Observations of inward source movement have been made in three ways. Lukkari et al. (1977) and Maltseva et al. (1981) observed the latitude of peak IPDP amplitude moving

southward along a north-south chain of stations as the frequency rose, implying inward source motion in the equatorial plane, Maltseva et al. (1985) and Pikkarainen et al. (1986) used riometer absorption events to trace inward source movements, and Arnoldy et al. (1979) observed the RH - LH - RH polarization sequence over a ground station, also implying source motion. Though it is now generally agreed that inward motion can play a role in creating the IPDP frequency shift, the significance of this role is not yet well understood. It has been variously claimed that the role is minor (Heacock, 1971) or major (Pikkarainen et al., 1983).

4.2.2. Increasing Background Field

An alternative process for increasing the magnetic field strength in the IPDP generation region is to have the region remain at a constant radial distance while the background field strength increases with time. This mechanism was first proposed by Roxburgh (1970). It requires that the IPDP event occur during the partial ring current decay phase after a magnetospheric substorm, when the current's equatorial magnetic field depression in the IPDP generation region is weakening. If we assume that L and W are constant, the increasing field effect on frequency would be (from equation 4.4):

$$\frac{f_f}{f_i} = \left[\frac{B_f}{B_i} \right]^{1.5} \quad (4.6).$$

Though Roxburgh (1970) reported IPDP events whose frequency rise could be quantitatively explained by this increasing field mechanism, the relationship between the magnetic field at geosynchronous orbit and that in an IPDP source region at lower L may not be as simple as was supposed. The actual field behaviour will depend critically not only on the growth and recovery of the ring current, but its position and movement as well. This could cause the magnetic field behaviour at geosynchronous orbit and at a lower IPDP source region to be quite different. Bossen et al. (1976), using a geosynchronous satellite and a conjugate ground station, found that the IPDP and magnetic field data could not support the increasing field mechanism (cf. section 3.5).

4.2.3. Azimuthal Drift

The azimuthal drift mechanism for IPDP frequency shifts was first articulated by Fukunishi (1969). This theory stipulates that the IPDP frequency rises as the energy of the protons involved in the ion-cyclotron instability falls.

The gradually softening proton energy spectrum is created by the energy dependent westward azimuthal drift velocity of the protons. After the substorm plasma injection, higher energy protons drift westward faster, reaching the generation region ahead of the lower energy protons on the same L shell. This effect would cause a steady frequency rise throughout an IPDP event. If B is assumed constant, then, from equation 4.4, the decreasing energy effect is given by:

$$\frac{f_f}{f_i} = \left[\frac{W_i}{W_f} \right]^{0.5} \quad (4.7).$$

Note that the dependence of f on W is relatively weak (power of only 0.5).

The existence of proton energy softening as described above has been verified by calculation from ground observations, using the delay time from substorm onset to IPDP occurrence and proton drift velocities, by Kangas et al. (1974) and also observed by satellite (cf. section 4.1). Despite this, there is still considerable uncertainty over the importance of the azimuthal drift mechanism to IPDP frequency shifts. Heacock (1971) ascribed to it the dominant role, while Pikkarainen et al. (1983) concluded that its contribution to IPDPs must be minor and Soraas et al. (1980)

stated that the observed energy dispersion was over too narrow a range to provide significant frequency rise. Bossen et al. (1976) noted that the azimuthal drift mechanism was a plausible mechanism to explain IPDPs.

4.3. DISCUSSION OF IPDP FREQUENCY SHIFT MECHANISMS

It is clear that the state of understanding of IPDP frequency shifts is far from complete since disagreement exists over the importance of, and even the existence of, the mechanisms described in section 4.2. It should also be pointed out that the relative importance of the roles of the three mechanisms discussed here could possibly change with changing magnetospheric conditions, and/or their significance could simply be different at different GMLTs.

The inadequacies found in each of the above mechanisms' ability to explain the IPDP frequency shift alone has forced the consideration of the superposition of two or more of these mechanisms to account for IPDP events. Most of these hybrid models have involved the combination of inward motion and azimuthal drift effects, with the inward motion being due to one of $\vec{E} \times \vec{B}$ drift (e.g., Fraser and Wawryzniak, 1978), plasmopause motion (e.g., Horita et al., 1979), or successive injections penetrating to lower L before their azimuthal drift starts (Kangas et al., 1974). These hybrid models have not actually been quantitatively tested against

IPDP data, and represent only the general realization that some sort of superposition of mechanisms is necessary to explain IPDPs.

In this thesis, we will test an IPDP frequency shift model involving the azimuthal drift and inward motion mechanisms which follows logically from the generation model discussed in section 4.1. In this model, the energy dispersive azimuthal drift effects occur during the westward drift of the hot protons from the injection boundary to the plasmapause. The source region inward motion results from the injected plasma covering a range in L in combination with plasmapause inward motion, with the slower drifting protons at lower L (cf. equation 4.3) meeting a contracting plasmapause above a ground station after the faster drifting protons at higher L intersect the plasmapause above the same ground station (see fig. 16 (top)). In addition, the model also incorporates a new inward motion process due to plasmapause geometry. Even if the plasmapause motion is not significant during an event, the IPDP generation region, as seen by a ground station, can still appear to move to lower L shells due to the shape of the plasmasphere dusk sector bulge. As the Earth's rotation carries the ground station from dusk towards midnight, the slower drifting lower L protons will meet the plasmapause at a steadily decreasing radial distance overhead of the ground station (see fig. 16

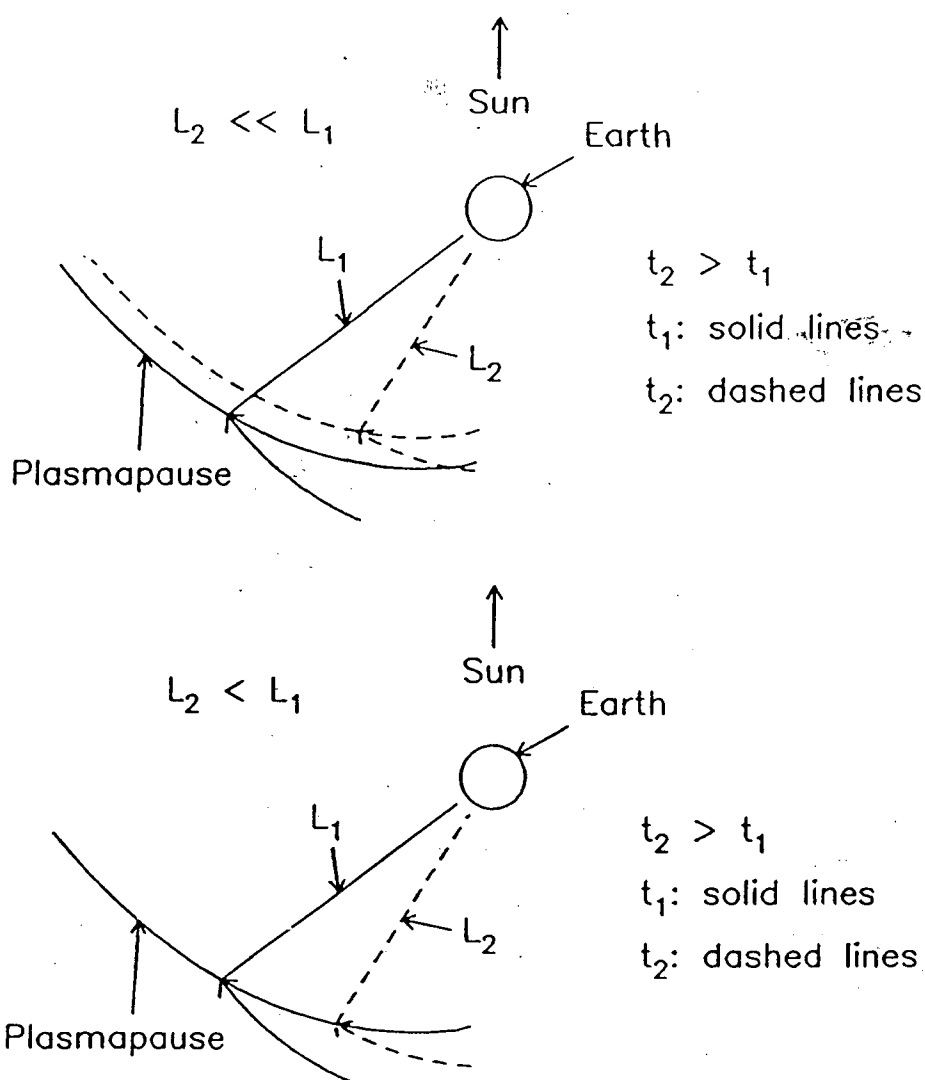


FIGURE 16.

TOP: Diagram showing inward source motion due to L-dependent azimuthal drift velocity variations and a contracting plasmopause. BOTTOM: Diagram showing that inward motion of the IPDP source region, due to Earth's rotation and the plasmopause bulge shape, still exists even when there is no contraction of the plasmopause. The times t_1 and t_2 correspond to the times of generation (plasmopause intersection) on the respective L shells.

(bottom)).

From equation 4.4, assuming a dipolar field, and using equation 4.3 to account for the varying drift velocities at different L, the frequency shift becomes:

$$\frac{f_f}{f_i} = \left[\frac{\Delta L T_i}{\Delta L T_f} \cdot \frac{t_{df}}{t_{di}} \right]^{0.5} \left[\frac{L_i}{L_f} \right]^4 \quad (4.8)$$

where $\Delta L T$ is the arc through which the protons drift, that is, the distance of drift = $\Delta L T \cdot L$ ($\Delta L T$ in radians), and t_d is the drift time of the protons from injection to plasmopause for each L shell. The proton energy (W) has been replaced in this equation by $\Delta L T$ and t_d since we are no longer sampling one stream of protons on one L shell with its simple softening spectrum, but crossing L shells into different proton streams which could result in a more complicated energy evolution. The drift times and arcs now characterize the proton energy variation seen at the plasmopause above a ground station as the station is carried eastward during an IPDP event. Equation 4.8 shows a slightly reduced dependence on L compared to equation 4.5, and also that increasing drift times and decreasing drift arcs will result in frequency rises.

The frequency shift model described here will be tested by computer simulation (section 4.4), and the results of the

analysis of data from a network of ground stations will also be interpreted in terms of this model (cf. Chapter Five). If any temporal changes, positive or negative, occur in the background magnetic field strength during an IPDP event, the effect would be superimposed on the other mechanisms already operating, enhancing or depressing the frequency rise created by these other mechanisms. However, in this model, such field changes are not essential to the development of an IPDP.

4.4. IPDP FREQUENCY BEHAVIOUR SIMULATION

The magnetospheric processes described in sections 4.1 through 4.3 can be simulated by computer. The purpose of this simulation is to quantitatively test the model to see if, starting from magnetospheric conditions observed to be associated with IPDP occurrence, it can reproduce IPDP frequency behaviour as seen by ground stations. This test is directed primarily at IPDP frequency evolution since this is the outstanding unexplained feature of IPDP-type micropulsations and the principal focus of this thesis. In addition to frequencies, however, the simulation also yields information on local times and latitudes of IPDP occurrence, event durations, and the evolution of the hot proton energies.

4.4.1. Computational Procedure

The model considered here begins at the formation of the injection boundary, follows the drift of the injected protons from there to the plasmopause where the IPDPs are generated, and finally determines what a ground station would see during an event.

The initial step of this modelling process involves defining the starting configuration. This requires specifying the plasmopause and injection boundary positions. The location of the injection boundary is calculated as discussed in section 4.1 (cf. equation 4.1). Note that the parameters in this equation can vary (Mauk and Meng, 1983), thus changing the form of the injection boundary. The plasmopause position is determined from a simple teardrop model of the plasmopause shape, the formula for which is (Kivelson, 1976):

$$L^2 R_E E = C \{ [1 - (1 + \sin(\phi))^{\frac{1}{2}}] / \sin(\phi) \}^2 \quad (4.9)$$

where E is the magnetospheric electric field strength in the equatorial plane, C is the corotation potential ($\approx 90\text{kV}$), and $\phi(\text{radians}) = \pi \cdot \text{LT}/12$ ($\text{LT} = \text{local time in hours}$). In equation 4.9, the reference meridian from which ϕ is measured is the meridian of the apex of the dusk sector bulge.

In the dusk sector, where most IPDPs occur, the plasmopause shape produced by this model is quite similar to the average plasmopause shape of Maynard and Grebowsky (1977) (cf. fig. 15). The orientation of the dusk sector bulge (i.e. LT position of the apex of the bulge) and the actual radius of the plasmopause, in the equatorial plane, are known to be variable. Here, these parameters are calculated from statistical relations found by Higel and Lei (1984). The orientation of the plasmopause bulge is given by:

$$LT = 23.45 - 0.64 \cdot \Sigma_{9hr} Kp \quad (4.10).$$

The radius of the plasmopause is controlled by E (cf. equation 4.9), which is given by:

$$E(kV/R_E) = 0.88 + 0.12Kp + 0.019Kp^2 \quad (4.11).$$

The validity of this relation is limited to values of $E < 2kV/R_E$ and $Kp < 6$.

By using equations 4.1 and 4.9 to 4.11 for, respectively, the plasmopause and injection boundary, the model starting configuration can be produced by inputting only the GMLT range of the injection boundary and the Kp indices for the preceding nine hours (three 3-hourly

values). At this point, a plot of the model starting configuration can be produced, as shown in the model flow chart in figure 17.

The next step of the modelling process involves calculating the injected proton drift motions. However, before this step, both the energy range and increment (in keV) must be input into the computation (cf. fig. 17). For simplicity, it is assumed that all the protons, which are initially at rest, start drifting from positions on the injection boundary. For comparison, however, some tests have been carried out under the assumption that the injected plasma occupies a limited area behind the boundary upon injection (see section 4.4.3).

At each (L,LT) point along the injection boundary, then, there exists a common range of energy values. For each energy level (W) at each (L,LT) point, the westward drift motion of a proton of that energy can now be calculated. The proton drift paths are assumed to be circular (cf. section 4.1), and the changing LT positions of each proton are followed using the westward drift velocity of equation 4.3. A new LT value is calculated for each proton at each time step of one minute during the drift phase of the model. Note that the pitch angle (α) used in the velocity calculations was 60° . This would, assuming that all protons in a distribution had the same α , correspond to an anisotropy of

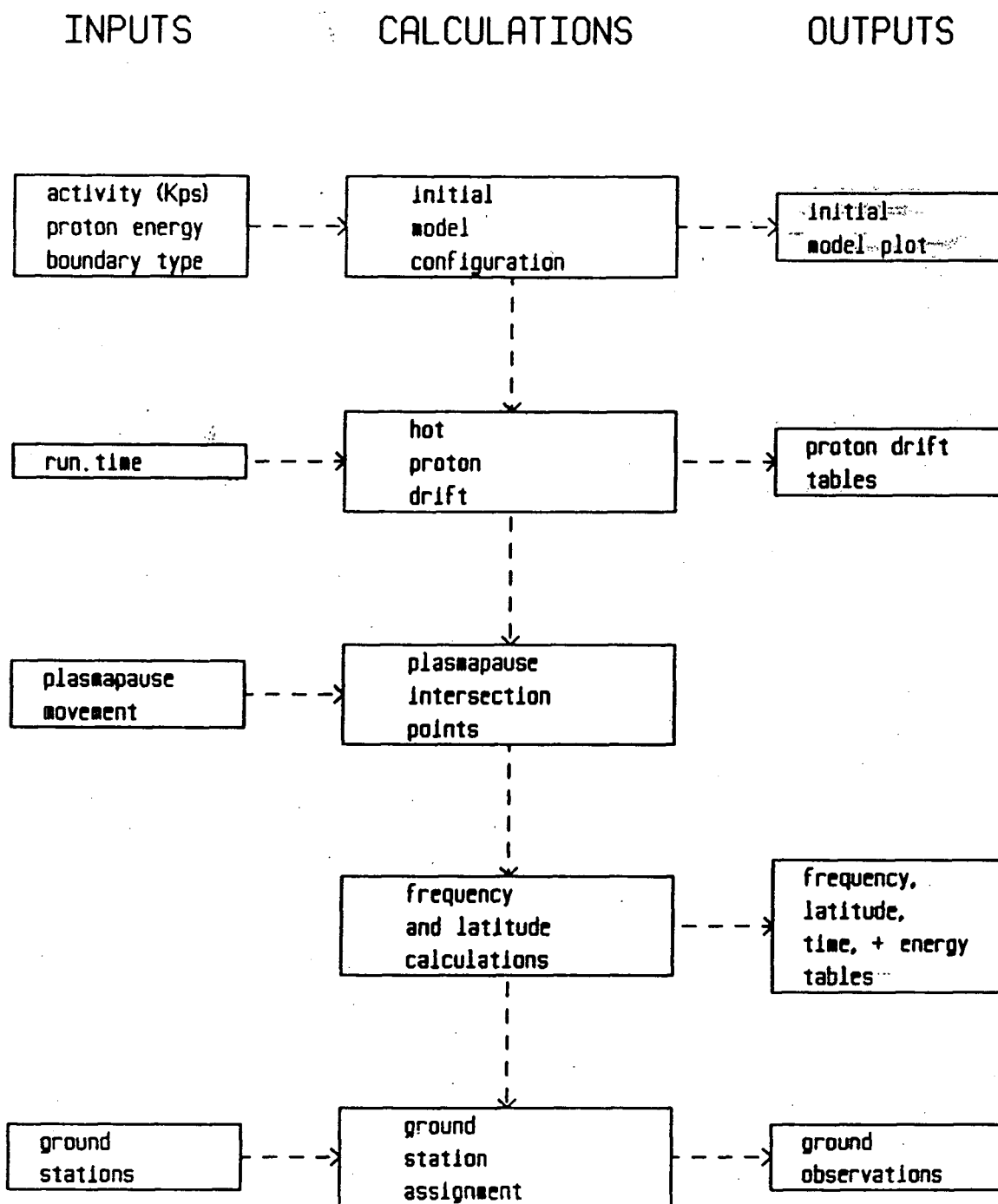


FIGURE 17.

Flow chart for computer simulation of IPDP micropulsations (see text for detailed description).

$A = 2$. Gendrin et al. (1971) found (for $P_c = 1$) that A was generally between 1 ($\alpha = 55^\circ$) and 2 ($\alpha = 60^\circ$). Note also that the start of the drift process is delayed at the western end of the injection boundary in accordance with the finite boundary formation time found by Arnoldy and Moore (1983) (cf. section 4.1).

During the drift phase of the model, for each proton energy on each L shell at each time step, the LT coordinate of the proton is tested to see if it is less than the plasmopause LT coordinate on the same L shell at that time (ie, $LT_p(L, W, t) < LT_{pp}(L, t)$, where LT_p is the drifting proton's LT and LT_{pp} is the plasmopause LT). For each case, the first time step at which $LT_p(L, W, t) < LT_{pp}(L, t)$ defines when plasmopause intersection is said to have occurred (cf. fig. 17). The particle drift motions are not followed after this time, since this is the point at which IPDP generation is said to take place. The intersection point determines the LT and time (t) of IPDP generation for protons of energy W drifting along a path of radius L . The model provides an option for the inward movement of the plasmopause, due to plasmasphere contraction, during the drift phase. If this option is selected, the plasmopause is moved inward at each time step by decreasing the LT coordinate of each (L, LT) pair defining the plasmopause in the afternoon-evening sector (see section 4.4.3). Because of the shape of the

plasmopause dusk sector bulge (cf. fig. 16 (top)), this has the same effect as decreasing the radial distance L at a fixed meridian.

Once the plasmopause intersection point is known, it is possible to calculate the ion-cyclotron wave frequency for that point, relative to a reference frequency (f_r), as follows (from equation 4.4 in a dipolar field):

$$\frac{f}{f_r} = \left[\frac{L_r}{L} \right]^{4.5} \cdot \left[\frac{W_r}{W} \right]^{0.5} \quad (4.12)$$

where L_r is the L value of the eastern (lower) end of the injection boundary and W_r is the highest proton energy value being considered. Assuming a dipolar field, the geomagnetic latitude can also be found from the L value of the intersection point as follows:

$$\lambda_{GM} = \cos^{-1}(1/\sqrt{L}) \quad (4.13).$$

With data from each intersection point, it is now possible to produce a table of results which includes the latitude, time, energy, local time, and relative frequency for each plasmopause intersection point, the point at which IPDP wave amplification is said to occur (see fig. 17).

This, however, does not yet represent an IPDP event. In

order to obtain a representation of an IPDP event as seen by a ground station, we must first define a set of ground stations, each of which "sees" only a limited LT sector of the plasmopause "above" it, that is, near its own meridian. The model allows specification of an array of up to ten ground sites spaced by half an hour in LT (7.5° long.). The station array can be positioned over any local time range. Only the LT coordinate of a ground site is necessary since north-south ionospheric ducting is considered to be very good, and a signal reaching the ionosphere on one meridian will be detected at any ground station in the auroral and sub-auroral zones along that meridian.

The LT range of the plasmopause that each ground station "sees" has been set at $\pm 0.15\text{h}$ (or $\pm 2.25^\circ$ Long.) for most runs. This is equivalent to a 250km range at 60° Lat., and is consistent with the Pc 1 source size results of Hayashi et al. (1981). The LT coordinate of each intersection point is tested to see if it falls within the LT range of a ground station. If so, it is assigned to that ground station and the relative frequency, latitude, time, and proton energy associated with it are said to be observed at that station. It should be noted that the local time of each ground site changes throughout the event as Earth's rotation carries the station eastward. It is now possible to write out a table for each station containing the

frequencies, times, latitudes, and energies "observed" at each station (see flow chart in fig. 17). These (f, t, λ, W) data sets are chronologically arranged, in order of increasing time (t) , and now represent an IPDP event as observed by that ground station.

4.4.2. Model IPDPs versus Observed IPDPs

The model described above has been run with all variables extending throughout, and sometimes beyond, their normal ranges associated with IPDP activity. The K_p index associated with the IPDP occurrence interval varied from 1 to 7, while $\Sigma_{9hr} K_p$ varied from 1 to 19. The proton energy ranges $(W_{max} - W_{min})$ used in the runs extended from 10 to 80 keV, and all the values used fell within the energy span of 10 to 340 keV. Most runs used an injection boundary calculated from equation 4.1, however, some tests were also done with different parameters substituted into equation 4.1 (cf. section 4.4.1) to produce steeper or flatter boundary shapes.

The results of these numerous runs can now be compared with the properties of IPDPs described in Chapter Three. However, the model produces only relative frequency information (f/f_r) , cf. equation 4.12), which restricts the comparisons that can be made. This difficulty can be partially circumvented by comparing the known IPDP

frequencies to frequencies produced by models having the most common Kps (near 3) and proton energies (40 to 100 keV) associated with observed IPDPs. The median frequency produced by these model runs is assumed to be the same as the median observed IPDP frequency, allowing a very rough adjustment to be made to the model frequencies so that they are comparable to observed frequencies. This enables the frequency ranges and slopes derived from these adjusted model frequencies to be compared with actual values. It must be emphasized, however, that no comparison of absolute frequencies is made here, and that all quantitative frequency-related information must be regarded as only rough estimates when being compared to observed values.

With this in mind, we can then examine the results presented in Table VIII. These results, which are a summary of the properties of model IPDPs computed with parameters most commonly associated with real events, are compared to observed IPDP characteristics (from Tables VI and VII in Chapter Three). Though the ranges of the model results do not always exactly match the IPDP observations, in general the agreement between the two is quite good. Note that though no GMLT of peak occurrence can be assigned from the model results since the actual rates of IPDP occurrence versus the input parameters are not well understood, the center of the GMLT range of the model results lies at 2030

Table VIII
IPDP Characteristics

	<u>Model Results</u>	<u>Observations</u>
Initial frequency (F_i)	0.1 - 0.6 Hz	0.1 - 0.3 Hz
End frequency (F_e)	0.2 - 1.1 Hz	0.5 - 1.0 Hz
ΔF ($F_e - F_i$)	0.1 - 0.6 Hz	0.2 - 0.7 Hz
Slope ($(F_e - F_i)/T$)	0.1 - 0.6 Hz/h	0.2 - 1.0 Hz/h
Duration (T)	0.25 - 1.75 h	0.33 - 2.0 h
Local time	1800 - 2300 GMLT	1600 - 0100 GMLT
Latitude	60° - 65.5°	55° - 65°

GMLT, which compares well with the observed peak at 2000 GMLT (cf. section 3.2).

The latitude frequency and latitude slope correlations mentioned in section 3.2 (paragraph two) are also produced by the model runs (see fig. 18). It is interesting to note, however, that a possible GMLT slope relationship about which conflicting statements have appeared (cf. section 3.2, paragraph three), is not clearly supported by the model results. The Kp GMLT and Kp GM Lat. correlations noted in section 3.2 are also reproduced by the model, though not in precisely the same manner. Previous comparisons have only been concerned with the single Kp value associated with the IPDP occurrence interval. While this single index can be used for the latitude comparison, since this index controls the plasmopause radial distance (cf. equations 4.9 and 4.11) (fig. 19), it is by itself not entirely appropriate for the Kp GMLT relation. Since $\Sigma_{9hr} Kp$ controls the GMLT orientation of the plasmopause (cf. equation 4.10), it is this parameter that accounts for the Kp GMLT relation that is both reproduced by the model and observed (fig. 19).

Most of the modelled IPDPs covered 45° - 65° GM Long., though it is possible to generate events spanning much greater ranges, such as 100° or more, examples of which have been reported (cf. section 3.3). It is also quite clear that differences can be seen within modelled IPDP events

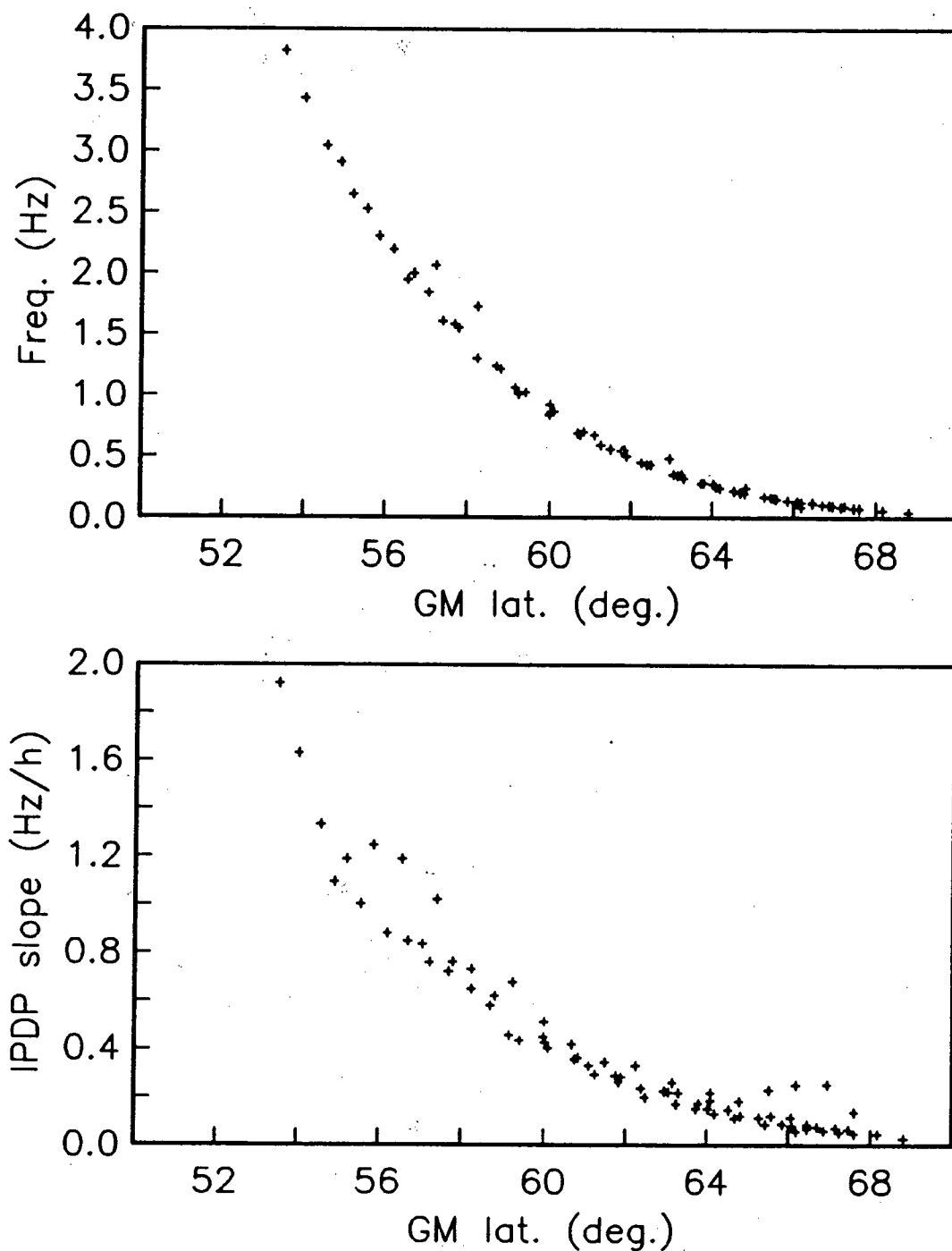


FIGURE 18.

Simulation results demonstrating the reproduction of the IPDP frequency - GM Lat. (top) and slope - GM Lat. (bottom) correlations.

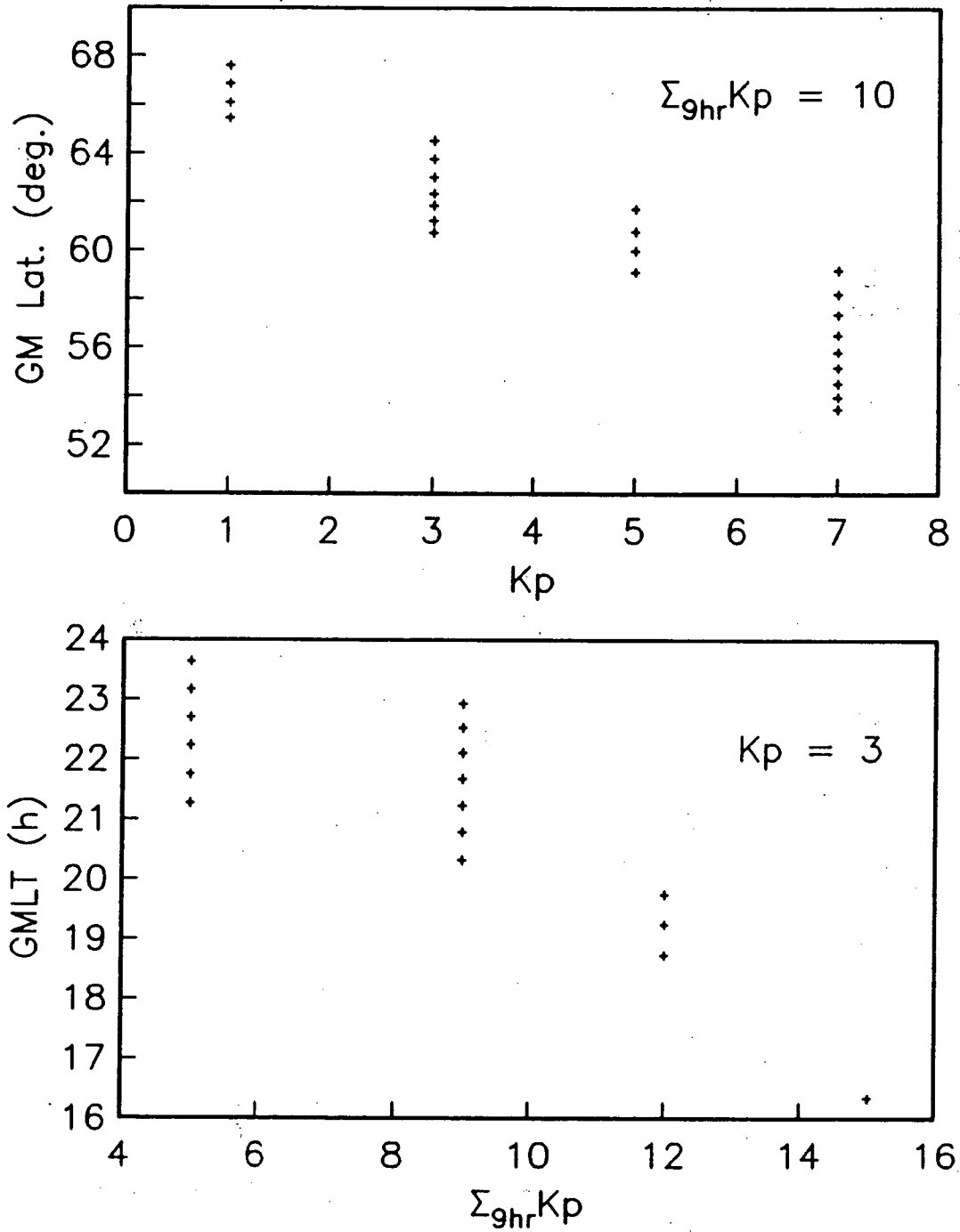


FIGURE 19.

Simulation results showing the GM Lat. - Kp ($\Sigma_{9hr}Kp = \text{constant}$) (top) and GMLT - $\Sigma_{9hr}Kp$ ($Kp = \text{constant}$) (bottom) correlations produced.

"observed" at ground sites spaced quite closely in longitude ($\Delta\text{GMLT} = 0.5\text{h}$). These differences can become very obvious over spans of 60° GM Long., a range over which longitudinal variations have been reported in observed IPDPs (cf. section 3.3). The model results agree with the reported later GMLT higher frequency correlation (fig. 20, top) and also show a later GMLT steeper slope correlation (fig. 20, bottom), though not always in a clear fashion. Most model event durations are either longer to the west or approximately the same at all stations seeing the event, though only cases of longer durations to the west have been reported in the literature (cf. section 3.3).

The event onset drift rates from the model can differ significantly from those discussed in section 3.3. For model IPDPs on less active days ($\Sigma_{9hr} Kp \leq 10$), onset drifts generally agree with reported observations, falling in the $2-5^\circ/\text{min.}$ range. However, on more active days ($\Sigma_{9hr} Kp \geq 10$), the onset drifts tend to be negative, as shown in figure 21, representing events developing from the west rather than the east. Such eastward development is contrary to what has previously been thought to be the case. This problem will be discussed in more detail in a subsequent section.

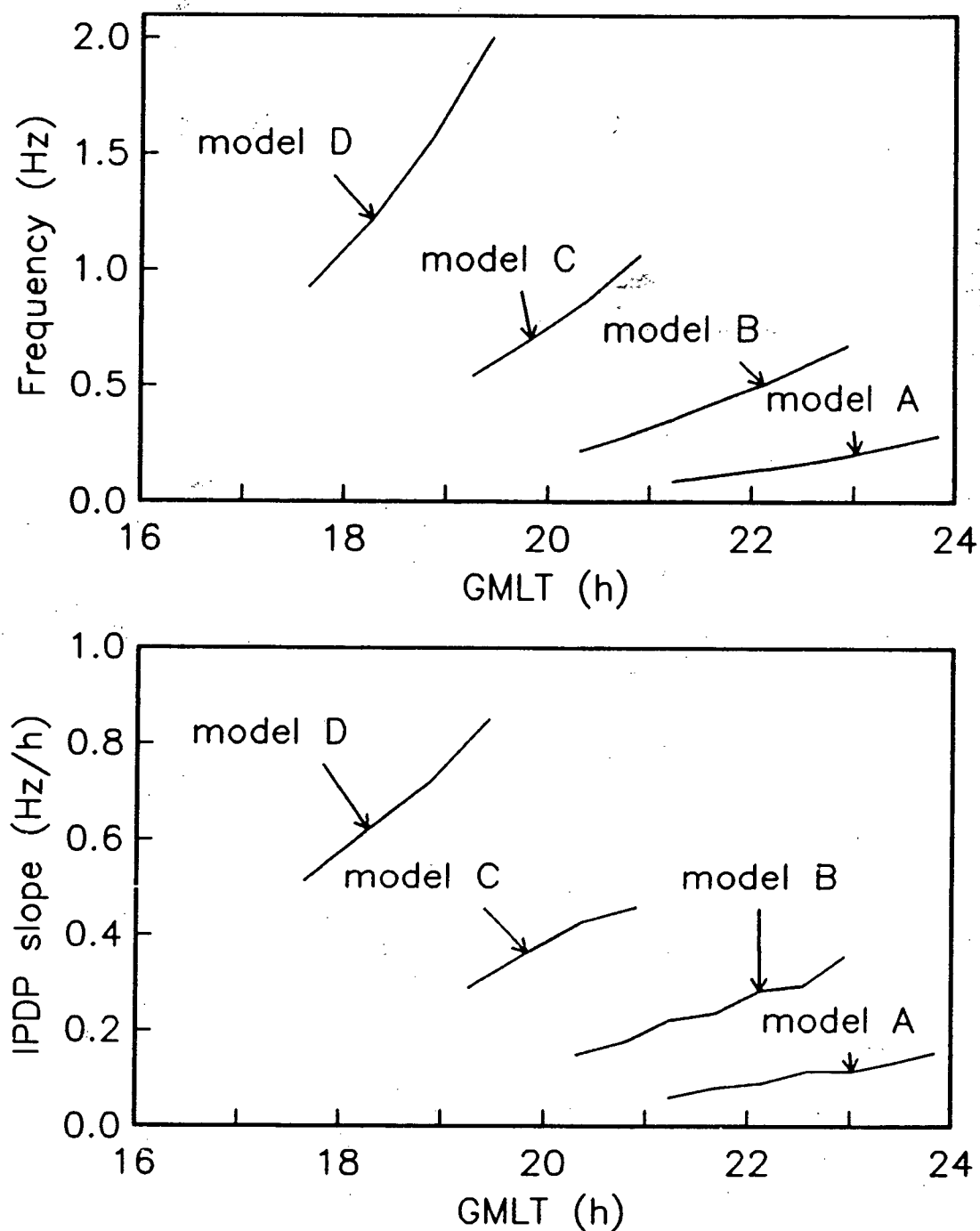


FIGURE 20.

Simulation results showing the frequency - GMT (top) and slope - GMT (bottom) correlations.

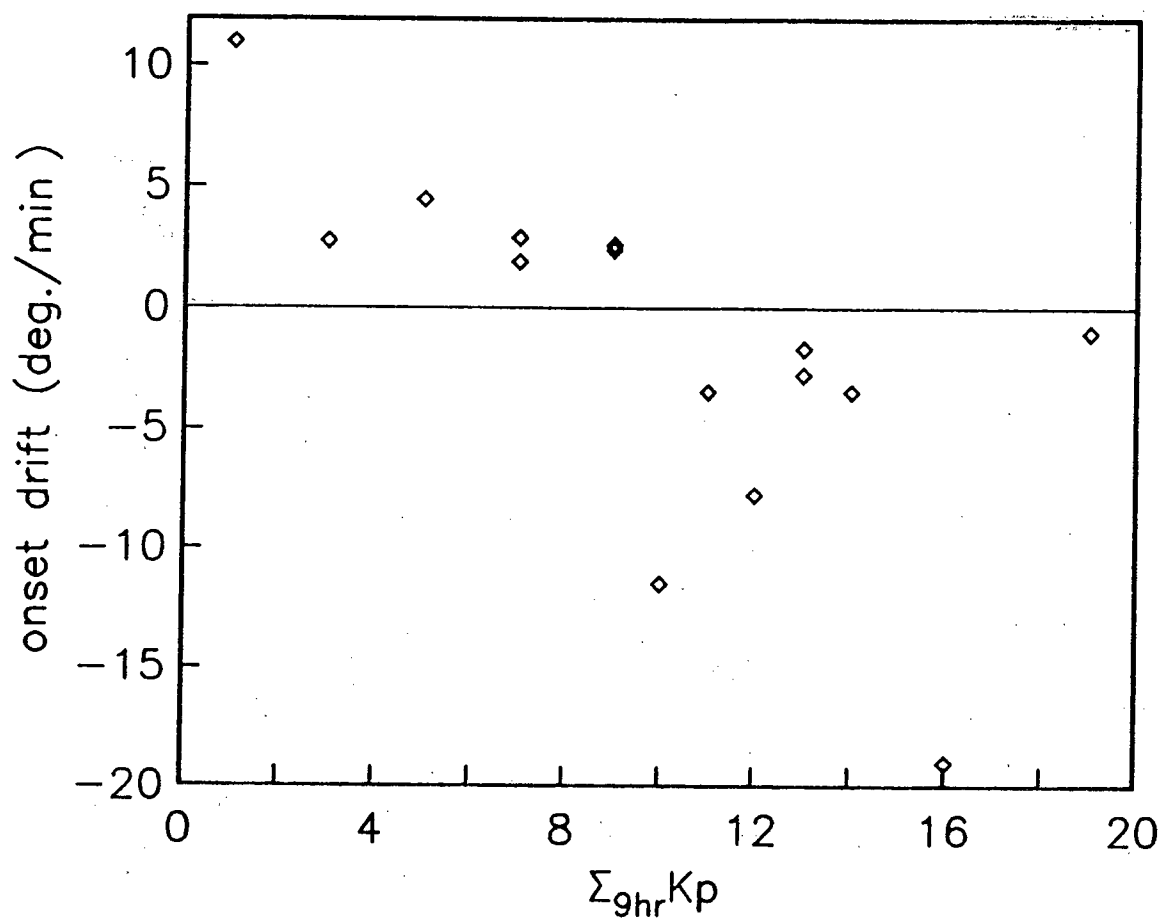


FIGURE 21.

Simulation results: onset drift versus $\Sigma_{9hr}Kp$, indicating the appearance of both westward and eastward developing IPDPs.

4.4.3. Other Model Results and Predictions

This section will present some new results produced by the model calculations.

There has been some uncertainty concerning the possible role of inward motion of the plasmopause in creating the IPDP frequency shift. Here, the effects of this movement have been explored by model calculation. Simulations have been carried out keeping all parameters the same except for the rate of plasmopause inward motion. Figure 22 (top) shows the plasmopause position, as seen by the same ground station, for four cases with differing plasmopause movement rates (dLT) ranging from zero to $dLT = -0.010h/[time\ step]$ (cf. section 4.4.1). The four cases are; Model A: $dLT = 0$, Model B: $dLT = -0.002h$, Model C: $dLT = -0.005h$, and Model D: $dLT = -0.010h$. The effects of this inward movement on IPDP frequency-time characteristics for the same four cases are also illustrated in figure 22 (bottom). Note that the greater inward movements, towards lower L shells and correspondingly lower latitudes, result in higher frequencies and higher frequency slopes due to the stronger magnetic field B and higher dB/dt "observed" by the ground station. The results of these calculations clearly demonstrate that while an inward moving plasmopause has the potential to change the characteristics of an IPDP, including dramatically enhancing the frequency rise, it is

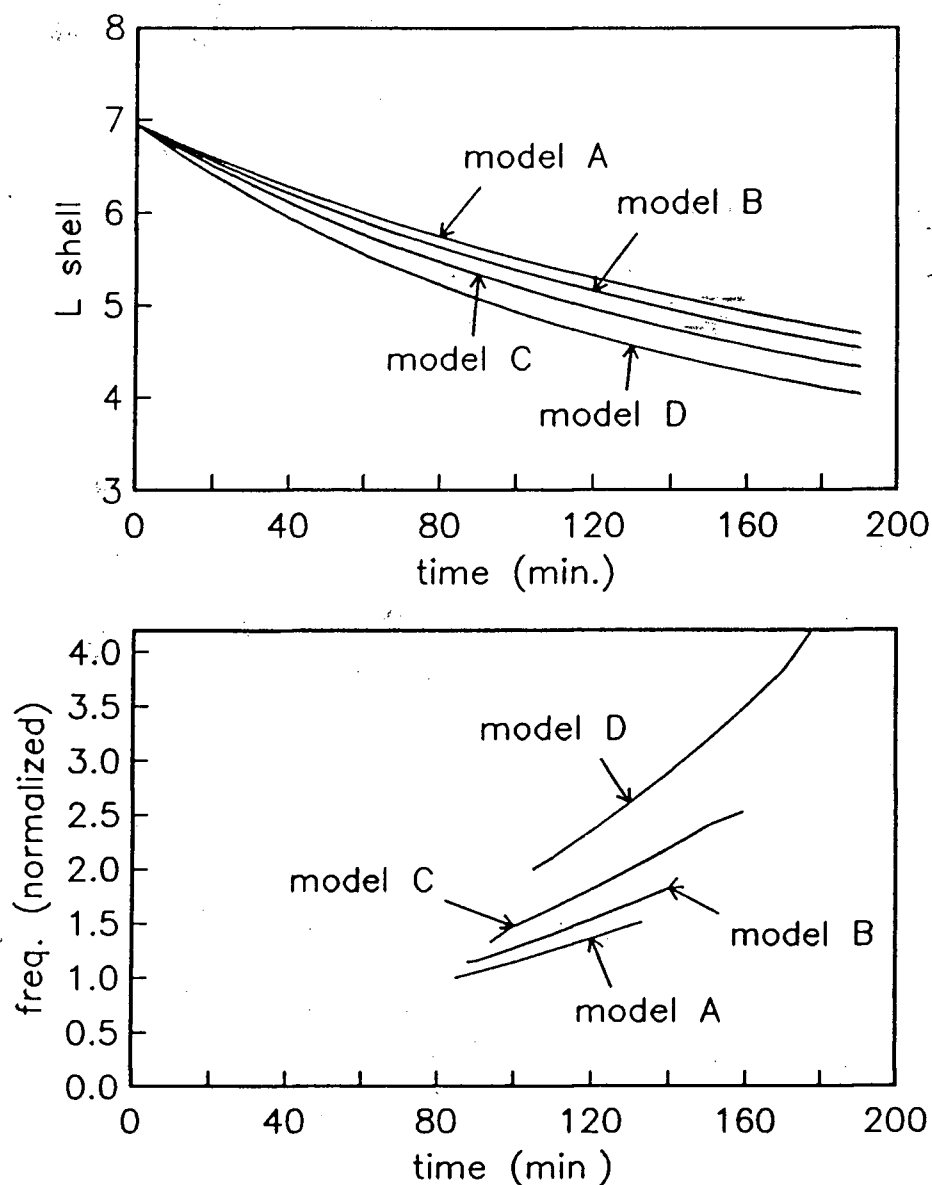


FIGURE 22.

Effects of plasmopause inward motion on IPDPs. Top: L shell of the plasmopause over a ground station for 4 cases of inward motion, increasing from A (no inward motion) to D (see text). Bottom: frequency-time plots for each of the above cases for an IPDP event as seen by the same ground station. Note that the zero-movement case (Model A) still shows significant inward motion and frequency rise.

clearly not a required condition for the appearance of an IPDP event, since the zero-movement case (Model A in fig. 22) shows a significant frequency rise.

The GMLT range over which the injection boundary forms is a primary factor controlling the longitudinal range over which an IPDP is seen on the ground, since, along with the plasmopause orientation and radial position, it determines over what GMLT range the ion-cyclotron instability can occur along the plasmopause. As noted in section 4.4.2, the most common span of modelled events was 45° to 65° GM Long.; for these models, the injection boundary GMLT span from which protons involved in the IPDP generation drifted ranged from 1.9 to 3.8 hours. In order to reproduce the very wide GM Long. extents of over 140° occasionally observed in IPDPs (cf. section 3.4), injection boundary spans of significantly greater than 4 hours GMLT are required.

It was mentioned in section 4.4.1 that some models were run with the proton drift starting not only on the injection boundary, but also from a limited area behind it. For these runs, the model was altered such that the proton drift began on and from an area of up to 10° behind the boundary, that is, on a given L shell, the protons can begin their drift anywhere on an arc beginning at the injection boundary and extending up to 10° to the east. The IPDPs seen on the ground resulting from these model runs exhibit only very

minor differences from events whose drift started on the injection boundary only, thus the disparities between the two model types are insufficient to determine, by way of comparisons to real events, which is the more appropriate.

As mentioned previously (cf. section 4.4.2), an interesting outcome of the IPDP modelling has been the appearance of eastward developing events. Eastward developing IPDPs are observed first at more westerly ground stations, then appear later at sites progressively further east. This effect, which has been reported only very recently (Hayashi et al., 1988), is referred to here as a negative, or eastward, onset drift velocity, as opposed to the normal positive, or westward, onset drift.

The geometry of the plasmopause and the injection boundary determine whether a modelled event will develop eastward or westward. For an eastward IPDP, the geometry must be such that the hot protons drifting westward on higher L shells meet the plasmopause before those on lower L shells. This requires that the drift time at higher L must be less than that at lower L. The drift time in turn depends on the drift velocity (v_d), which is higher at higher L, and on the length of the drift path, that is, the local time range ΔGMLT through which the protons drift. The major factors controlling how ΔGMLT varies between high and low L are the orientation of the plasmopause, or the GMLT position

of the bulge apex, and the shape, or steepness, of the injection boundary. In general, steeper boundaries, those which curve more rapidly away from Earth, produce westward developing events, while flatter boundaries, those whose distance from Earth increases more slowly, tend to result in eastward developing events. Also, eastward events tend to occur on more active days when the plasmopause is generally lower and has its bulge apex at earlier GMLTs and the injection boundary is also lower and is shifted toward earlier GMLTs (cf. fig. 14). Figure 23 shows examples of the different plasmopause injection boundary geometries necessary to produce eastward and westward IPDP events.

As a result of the modelling conducted, the major differences between eastward and westward developing IPDPs, as observed from the ground, appear in the onset drifts, durations, and hot proton energy spectra. As mentioned above, the onset times are later for more easterly sites for eastward events, opposite to the case for westward developing events. The trend in durations of eastward IPDPs is also opposite to that of westward events, with events lasting longer at the more easterly ground stations. The energy spectra of the protons involved in the generation of the IPDP waves observed by a ground station are believed to show a softening energy trend. This effect is believed to proceed more slowly to the west, and model calculations are

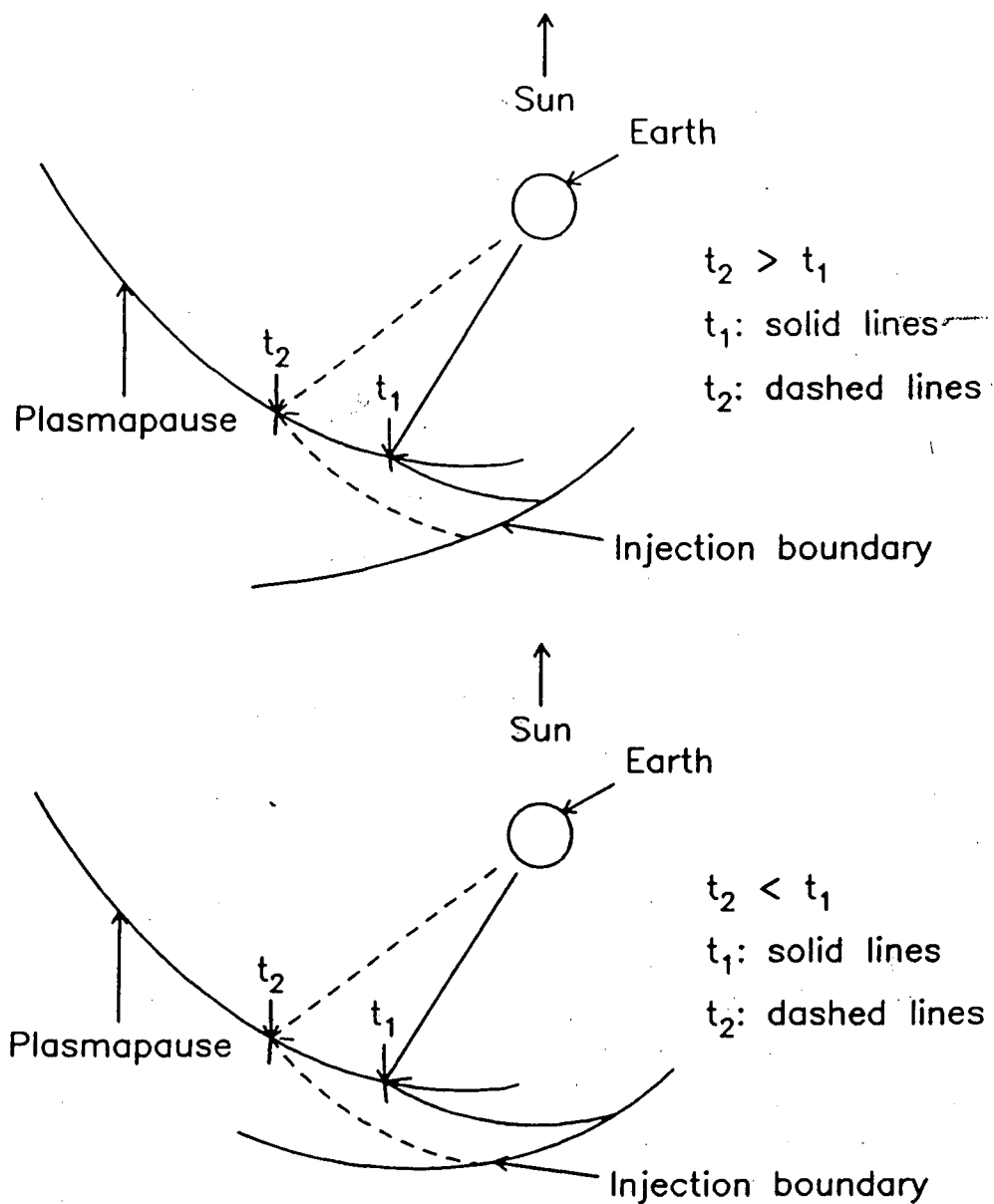


FIGURE 23.

Model diagrams for a westward developing IPDP ($L_b = 30/(LT-17.5)$) (top) and an eastward developing IPDP ($L_b = 60/(LT-12)$) (bottom). Both models used $K_p = 3$ and $\Sigma g_{hr} K_p = 9$. The plasmopause profiles are calculated from equations 4.9 through 4.11.

in agreement with this result for westward developing events. However, for eastward IPDPs, the model results show the softening proceeding more slowly to the east. Figure 24 demonstrates these model results.

These predictions concerning eastward IPDPs await verification by observation. However, the model parameters producing the eastward events seem quite plausible, and, as mentioned, recently the appearance of eastward events has been indicated by Hayashi et al. (1988). Still, even if they do exist, the absence or scarcity of eastward events can tell us something of the injection boundary shape, indicating perhaps that it is more commonly of the steeper form rather than having a flatter profile. It is evident that most IPDPs occur at evening sector local times when the plasmopause bulge is located near dusk or later. This may also account for the lack of eastward events, which modelling shows would tend to occur more readily at the earlier local times accessible when the bulge is located at earlier GMLTs.

4.4.4. Model Versus Real GMLTs

Comparison of the IPDP model considered here to real IPDP events can be achieved by entering measured magnetospheric parameters associated with observed IPDPs into the model and checking the results against the observed

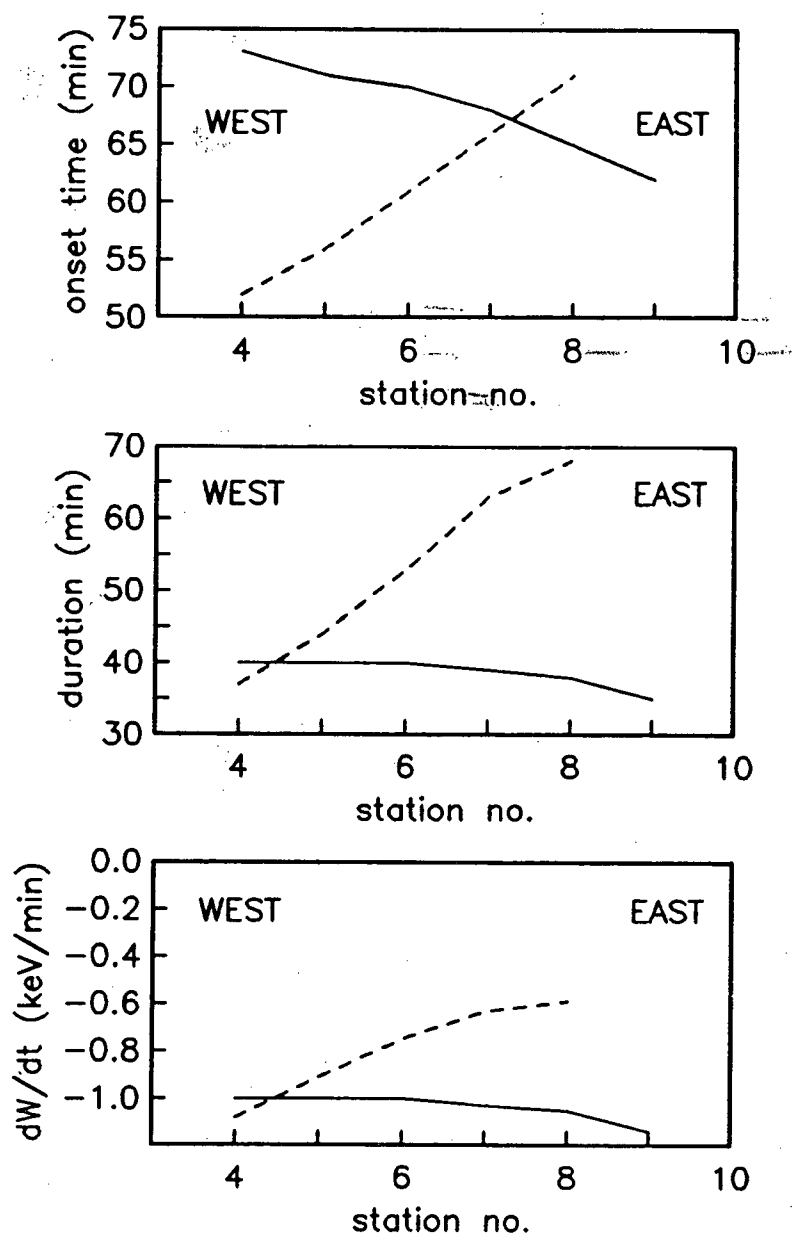


FIGURE 24.

Simulation results: westward versus eastward developing IPDPs. Onset times (top), durations (middle), and proton energies (bottom) are compared for an east - west line of stations (models as in fig. 23). The stations are separated by $7\frac{1}{2}^\circ$ long. ($\frac{1}{2}h$). The solid lines are for the westward developing event and the dashed lines for the eastward developing event.

event. Due to the nature of the model and the real event analysis requirements, however, only the GMLT range of occurrence can be compared for all ten IPDPs in the data set under consideration.

For the ten events available, the GMLT span over which each occurred has been determined. The GMLT range of possible IPDP occurrence allowed by the model was found, for each event, by a simulation run using the Kp indices associated with that event. Such a run determines the plasmopause position and, assuming an injection boundary easternmost end of 0200 GMLT, the lowest L shell of hot proton drift. The L range covered by the westward drift is determined by this lower limit and an upper limit given by the plasmopause bulge apex L. This L range combined with the plasmopause position then gives the GMLT range of possible IPDP generation. For seven of the ten IPDPs studied, the observed GMLT span falls within the range allowed by the model, and one other event's GMLT span lies mainly (more than 50%) within the permitted range. In the case of only two events does the observed GMLT range not correspond to the model results at all. Figure 25 shows a successful match, the Feb. 15 event, and a failed match, the Feb. 14 event.

These model results indicate that the model is reasonably successful in predicting the potential GMLT

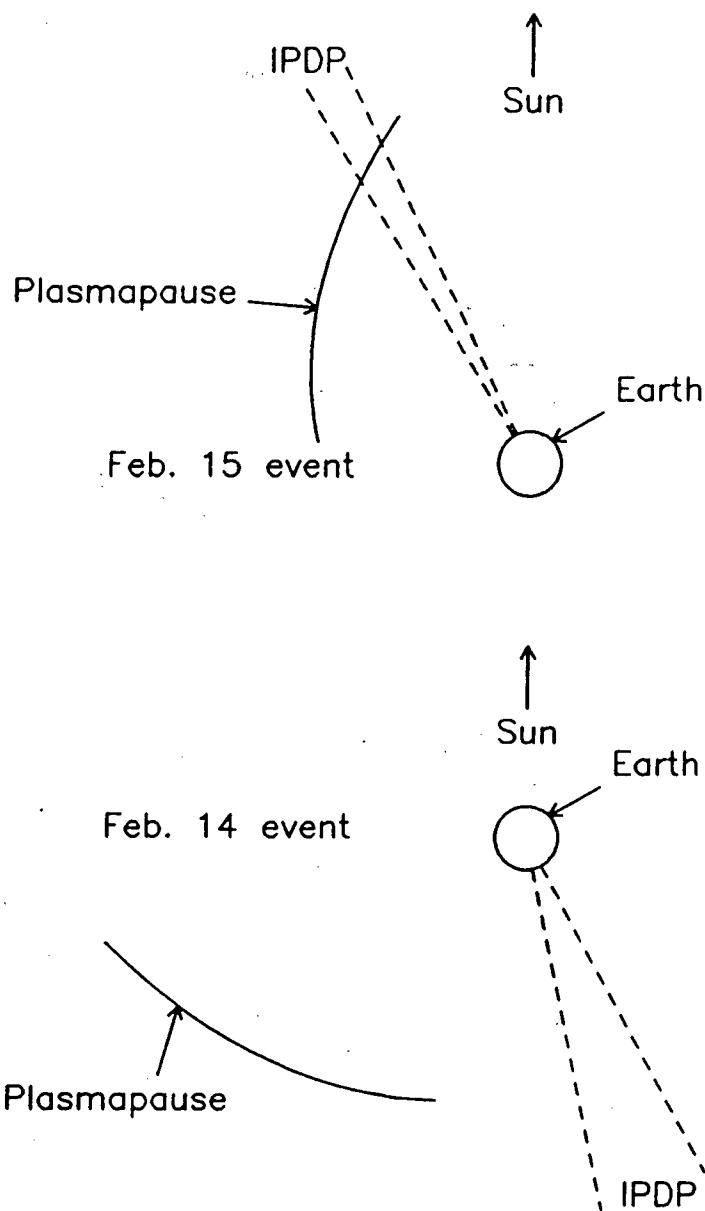


FIGURE 25.

Modelled versus observed IPDP GMLT comparisons. The plasmopause section plotted indicates where the model predicted an IPDP could occur, and the observed IPDP GMLTs are marked by the dashed lines. Here, a successful prediction is shown (Feb. 15 event, top), along with an unsuccessful one (Feb. 14 event, bottom).

positions of IPDPs. The statistical nature of the relations determining the plasmopause size and orientation and the injection boundary position may be the cause of the two failed GMLT predictions, though a larger IPDP data set would be necessary for a proper evaluation of the performance of these relations as combined in the context of this IPDP model.

4.4.5. Discussion of IPDP Simulation Model

As mentioned at the outset of the description of this IPDP model, the model is quite simple and of limited purpose. It calculates only relative frequencies, and the plasmopause and injection boundary positions are determined from statistical relations which will not always be applicable to individual events. Furthermore these relations are not valid for all Kps (cf. section 4.4.1). Another limitation of the model is its lack of facility to allow for the effects of temporal changes in the geomagnetic field strength, at a fixed L, on IPDP frequency evolution. This was not included since the increasing background field mechanism is not believed to be necessary for producing IPDP frequency behaviour (cf. section 4.3).

The assumption of good ionospheric ducting applies only along the geomagnetic meridian, and not to ducting in the east-west direction, perpendicular to the geomagnetic

meridian. That good north-south ducting of IPDP signals in the sub-auroral zone ionosphere occurs is well known, but the role of east-west ducting is less well understood (cf. Appendix B). If east-west ducting does exist, its primary effect would be to increase the frequency band-width of an IPDP as observed at the latitude of the source field lines by adding, at generally lower amplitudes, lower or higher frequencies ducted from the west or east respectively, to the generally higher amplitude signals observed from its own meridian by a ground station. An additional assumption used to facilitate the calculation of the change in IPDP frequency due to a change in L , and also the geomagnetic latitude from L , is that of a dipolar geomagnetic field.

With its framework of limitations and assumptions discussed above, this model may be considered to be a "first approximation" attempt. To develop it further would require the inclusion of a more sophisticated geomagnetic field model, including ring current and temporal effects, better information on the formation and position of the injection boundary and the nature of the plasma behind it, improved knowledge of the shape and movement of the plasmapause, and a more detailed treatment of the ion-cyclotron instability generating the IPDP and the subsequent propagation of the HM waves through the magnetosphere and ionosphere to the ground stations.

Where it was possible to make comparisons, the model results agreed quite well with the known IPDP observations (cf. section 4.4.2). A check of modelled IPDP GMLTs versus observed IPDP GMLTs for ten events also revealed a good match (75%, cf. section 4.4.4). These results, while not proving the correctness of the model, raise confidence in its usefulness and indicate that the new results produced by it merit consideration and investigation. In summary, these new results include the significant apparent inward motion possible without actual plasmopause inward motion and the possibility of eastward developing IPDP events.

CHAPTER 5. EXPERIMENTAL RESULTS

Three IPDPs, the Feb. 14, Feb. 15, and Feb. 24c events (cf. sec. 2.1), have been analysed in detail (cf. sec. 2.2). The results of these analyses are used here to study the causes of the IPDP frequency rise and the longitudinal development of IPDPs. The primary aim of this work is to provide some experimental indication of the relative importance, or even existence, of the various frequency shift mechanisms discussed in sections 4.2 and 4.3. Section 5.1 examines the inward motion mechanism's effect on the Feb. 14 and Feb. 15 IPDPs (cf. section 4.2.1), while section 5.2 presents a study of the increasing background magnetic field mechanism (cf. section 4.2.2). In section 5.3, the contributions of the azimuthal drift mechanism (cf. section 4.2.3) to the frequency shifts of the two events studied in section 5.1 are examined. The longitudinal development results are presented in section 5.4, and section 5.5 contains a discussion of all the experimental results with reference to the IPDP model described in Chapter Four.

5.1. INWARD MOTION OF IPDP SOURCE REGION

In order to understand the frequency effects of the inward motion mechanism, the inward motion of the IPDP source region must be determined. This can be achieved through the analysis of the evolution of amplitude

variations as observed along a north-south line of stations during an IPDP event. Such analyses have been carried out for the Feb. 14 and Feb. 15 IPDPs, and are described below. The Feb. 24c event is not suitable for such analysis since only one of the stations situated to record the event on each north-south line was operating.

5.1.1. Feb. 14 Event

The IPDP event of Feb. 14 was observed by the three stations at the southern end of the Saskatchewan line; WS, PS, and LL (cf. section 2.1, fig. 3). From each of these three stations, data blocks centered every five minutes from 0835 to 0940 UT, are analyzed (cf. section 2.2) in order to follow the frequency, amplitude, and polarization evolution of the event.

The polarization spectrograms from PS and LL provide information on the propagation characteristics of the IPDP waves in the ionosphere necessary for the understanding of their amplitude variations along a north-south station line. The left-hand (LH) polarized field-line guided waves from the magnetospheric IPDP source region enter the ionosphere and penetrate through the F-layer. Some of the wave energy may become trapped in the ionospheric F-layer waveguide if the wave frequency is above a lower cut-off frequency determined by the ionospheric plasma characteristics. The

waveguide is formed in the Alfvén velocity minimum created by the peak in ionization in the F2-layer (cf. Appendix B). The trapped wave energy, which is converted from LH to RH (right-hand polarization), can then propagate horizontally along the geomagnetic meridian for long distances. Therefore, IPDPs subject to ionospheric propagation will show LH polarization if the field lines guiding the waves from the magnetospheric source region enter the ionosphere overhead of the ground site and RH polarization if they are to the north or south of the ground station (Greifinger, 1972; Arnoldy et al., 1979). If no such ionospheric propagation is occurring, then only LH polarization should be observed. A study of the appearance of RH polarization then tells us whether ionospheric propagation is occurring and below which frequency this effect is cut off, and thus indicates whether or not wave amplitude variation with distance from the wave entry point into the ionosphere is affected by ionospheric propagation. Note that the point, or area, on each meridian at which the IPDP waves enter the ionosphere is often termed the "secondary source".

In the polarization spectrograms from the Feb. 14 event, RH polarization appears only above ≈ 0.5 Hz, thus indicating the lower cut-off frequency of ionospheric propagation effects during this IPDP (for example, see fig. 26 and 27). The pattern of appearance of RH polarization

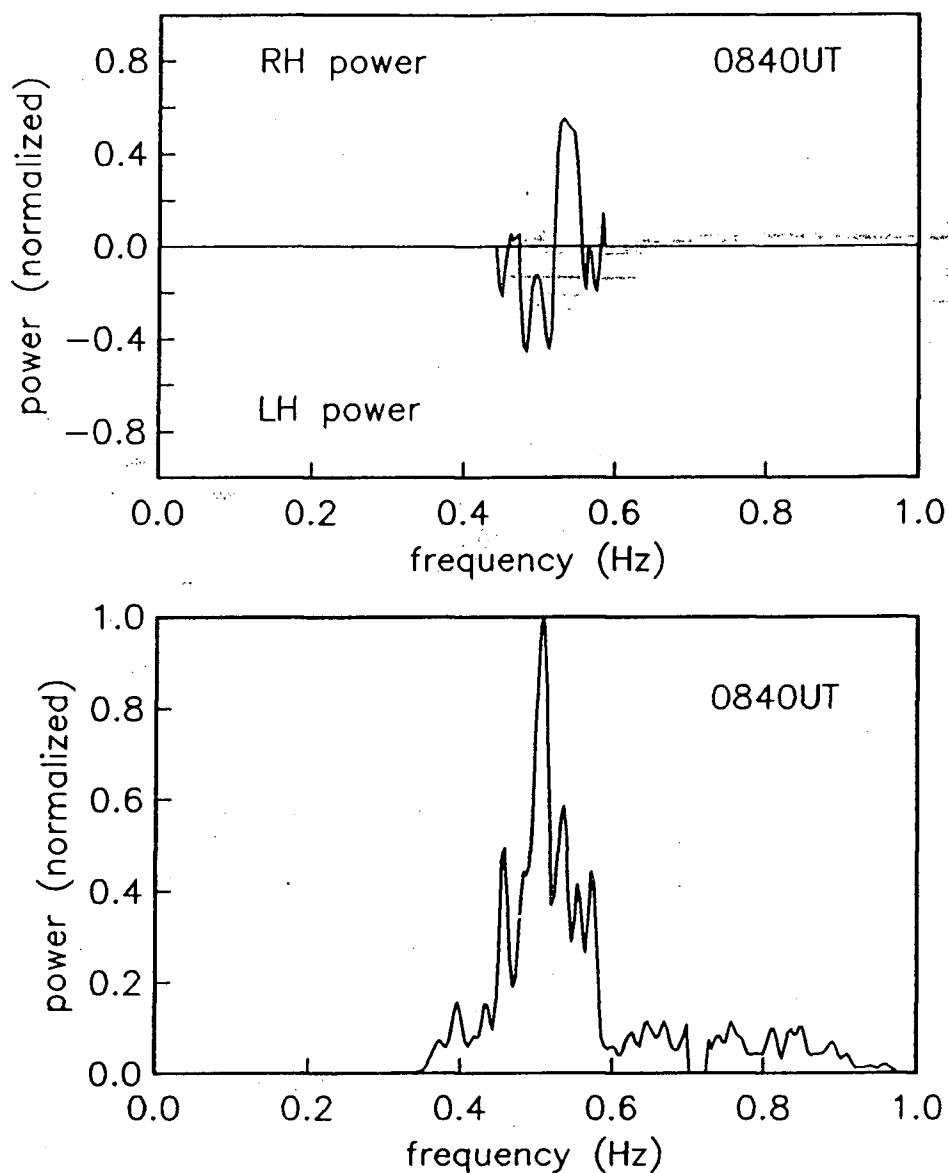


FIGURE 26.

Polarization spectrogram (top) and power spectrum (total horizontal component) (bottom) from PS for 0840UT, Feb. 14. The polarization spectrogram is actually presented as [polarized power]/[horizontal component power]. The change from LH polarization at lower frequencies to RH polarization just above ≈ 0.5 Hz indicates the position of the lower cut-off frequency of ionospheric propagation.

during this IPDP is also consistent with waves travelling within the ionosphere from a southward moving secondary source. At PS, first RH polarization appears at 0840UT, in the band above 0.5Hz (cf. fig. 26), then LH is dominant in the center of the frequency band at 0900UT (fig. 27), and lastly we see only RH again at 0940UT (fig. 27). The polarization spectrograms from LL in figure 28 also support this picture, with the signal showing RH polarization at 0900UT when the secondary source is to the north, near PS, and LH polarization in the upper part of the frequency band at 0940UT as the secondary source approaches LL. Since virtually all of this event is at frequencies $>0.5\text{Hz}$, propagation in the ionospheric waveguide is taking place. Thus, when comparing IPDP power levels observed at the three stations for the purpose of determining the secondary source position, the energy attenuation between sites can be treated as a ducted wave problem.

It should be pointed out that the simultaneous appearance of both LH and RH bands in the IPDP spectra (cf. fig. 26, 27) indicates that the magnetospheric source region is not a one-dimensional line along the plasmopause, but occupies a more extended two-dimensional area in the vicinity of the plasmopause (Hayashi et al., 1988). If the generation region were purely one-dimensional, then we should see only one polarization, LH or RH, at a time.

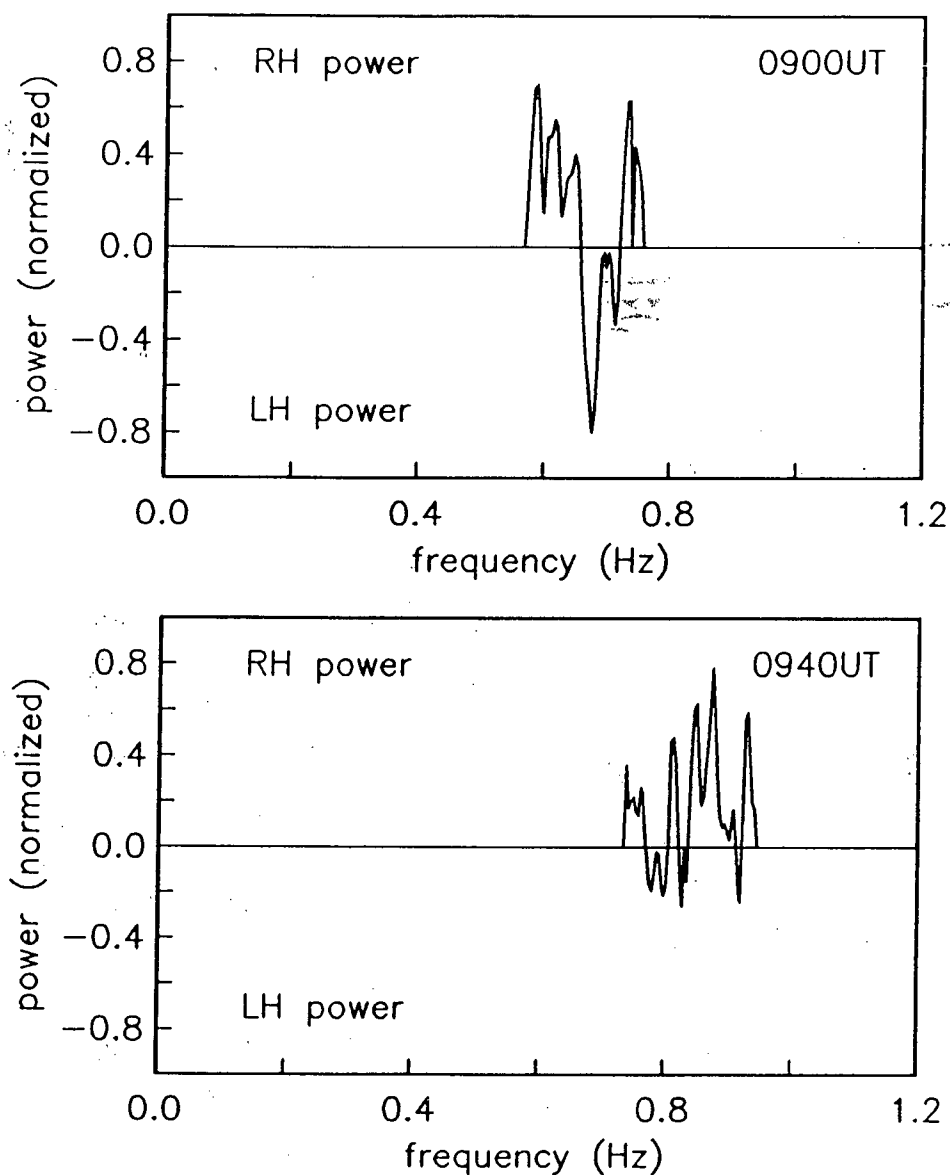


FIGURE 27.

Polarization spectrograms from PS for 0900UT and 0940UT (presented as in fig. 26). The RH - LH - RH profile at 0900UT indicates that the secondary source (LH waves) is approximately overhead of PS at this time, while the predominantly RH polarization evident at 0940UT is a result of waves ducted from a secondary source distant from PS. The RH bands in the low and high frequency sections of the 0900UT spectrogram represent signals ducted to the site from just north and south of it, respectively.

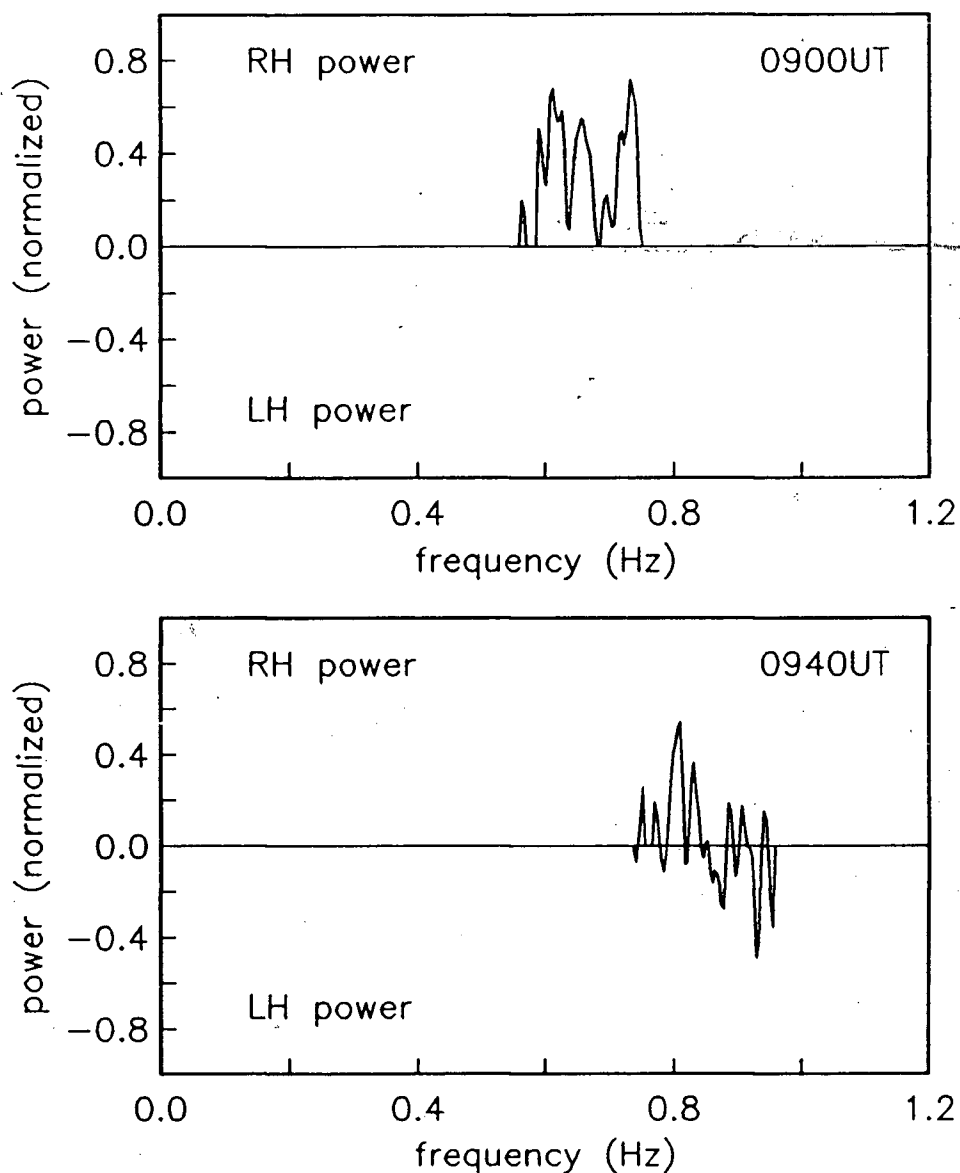


FIGURE 28.

Polarization spectrograms from LL for 0900UT and 0940UT (presented as in fig. 27). Here, the polarization is RH at 0900UT since the secondary source is near PS (cf. fig. 27) and is predominantly LH in the upper part of the IPDP frequency band at 0940UT, indicating that the secondary source has moved southward and is approaching LL.

Due to recording system problems in the X component at WS, IPDP signal power in only the Y data component can be compared between all three stations. These difficulties also eliminate the possibility of studying polarization spectrograms from WS. However, as part of a study of IPDP signal power variations along a north-south line of stations, the problem of differing power variations between the X and Y components along the line was examined by Koleszar (1980). The result was that the X and Y component variations were sufficiently similar to justify the use of one component only, though the distances from the secondary source concerned were less than 1.6° of latitude. This is confirmed by the similarity of the X and Y component power variations at LL during the Feb. 14 IPDP, as shown in figure 29. The likeness of the X and Y component power variations may, however, break down at larger distances from the secondary source since the polarization below the duct becomes linear along the meridian, or in the X-direction, with the Y component therefore becoming very small. Note that LL and WS are separated by $\approx 3^\circ$ of latitude. Althouse and Davis (1978) showed that the Y component is much weaker relative to the X component at a low latitude site than it is at sites $\approx 1000\text{km}$ to the north which are closer to the secondary source.

In order to quantitatively determine the latitudinal

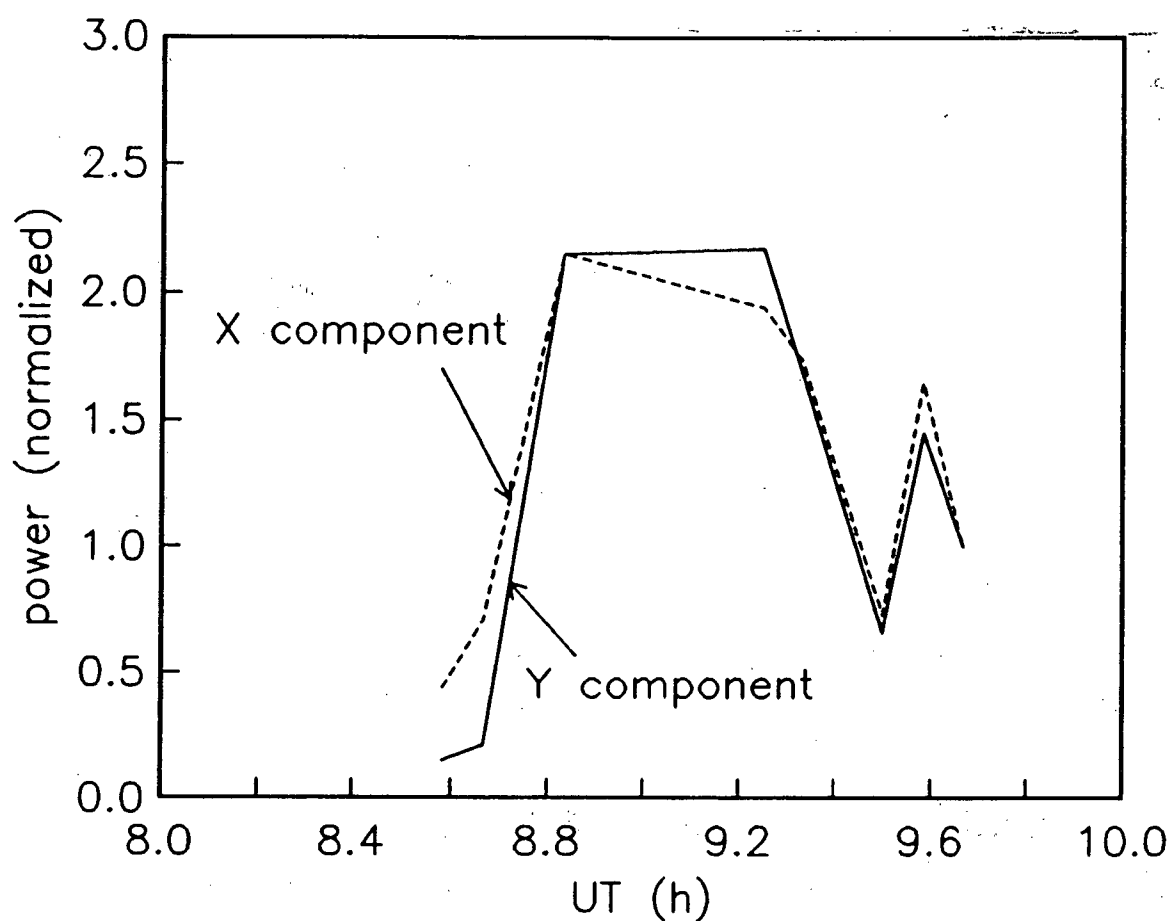


FIGURE 29.

Plots of the X and Y component peak power variations for the Feb. 14 IPDP. For ease of comparison, each component is normalized to its 0940UT level. The plots are generally quite similar, though the stronger X component before 0845UT may be indicating the beginning of the presence of linear polarization below the duct (see text).

position of the secondary source, we must know the attenuation factor for the ducted waves. This can be determined experimentally from the power ratios between ground stations and the known inter-station distances if the secondary source is known not to be between the two sites in question. This relative secondary source position can, in turn, be established from the polarization spectrograms and a qualitative examination of inter-station power ratios. For the Feb. 14 IPDP, the polarization spectrograms from PS exhibit the characteristic RH - LH - RH time profile of a southward moving secondary source with this source being north of, or in the vicinity of, PS until $\approx 0910\text{UT}$, and south of PS thereafter. An examination of the inter-station power ratios can, under some circumstances, provide confirmation as to whether or not the secondary source is actually between any two sites. For example, if the power ratio $LL/WS \approx 1$, then the secondary source would be approximately half way between WS and LL. This would be confirmed by having the ratios PS/WS and PS/LL both significantly greater than one (see fig. 35 for station locations), and would place the secondary source somewhere between PS and WS. This type of confirmation can be important, since near the secondary source, the polarization pattern can sometimes be more complex than the simple situation described above (cf. Appendix B).

Using the PS/LL power ratios before 0910UT (see above), we can then calculate the attenuation as follows:

$$\Lambda = \frac{1000}{139} \cdot 10 \text{ Log } \left[\frac{\text{PS}}{\text{LL}} \right] \quad (5.1)$$

where Λ is the attenuation in dB/1000km, which is the form commonly used to express duct attenuation (Manchester, 1966; Greifinger and Greifinger, 1973; Althouse and Davis, 1978), and 139 is the PS - LL separation distance in kilometers. The resulting attenuation factor is 21.5 ± 2.4 dB/1000km. Due to very weak signal strengths at WS after 0910UT, no attenuation calculations were possible using the PS/WS power ratios. There was no noticeable frequency dependence of the attenuation, though the frequency range covered in the above calculations was quite narrow (0.15Hz) as compared to some duct model calculations (cf. Appendix B).

This attenuation factor may now be used to calculate the position, along the meridian, of the secondary source when this source is between two stations. To facilitate this, theoretical power ratio versus north-south position profiles were calculated for each of the three station pairs of the Saskatchewan chain (PS/WS, PS/LL, and LL/WS) using Λ for the Feb. 14 event as calculated above. These profiles are shown in figure 30. For comparison, the experimental

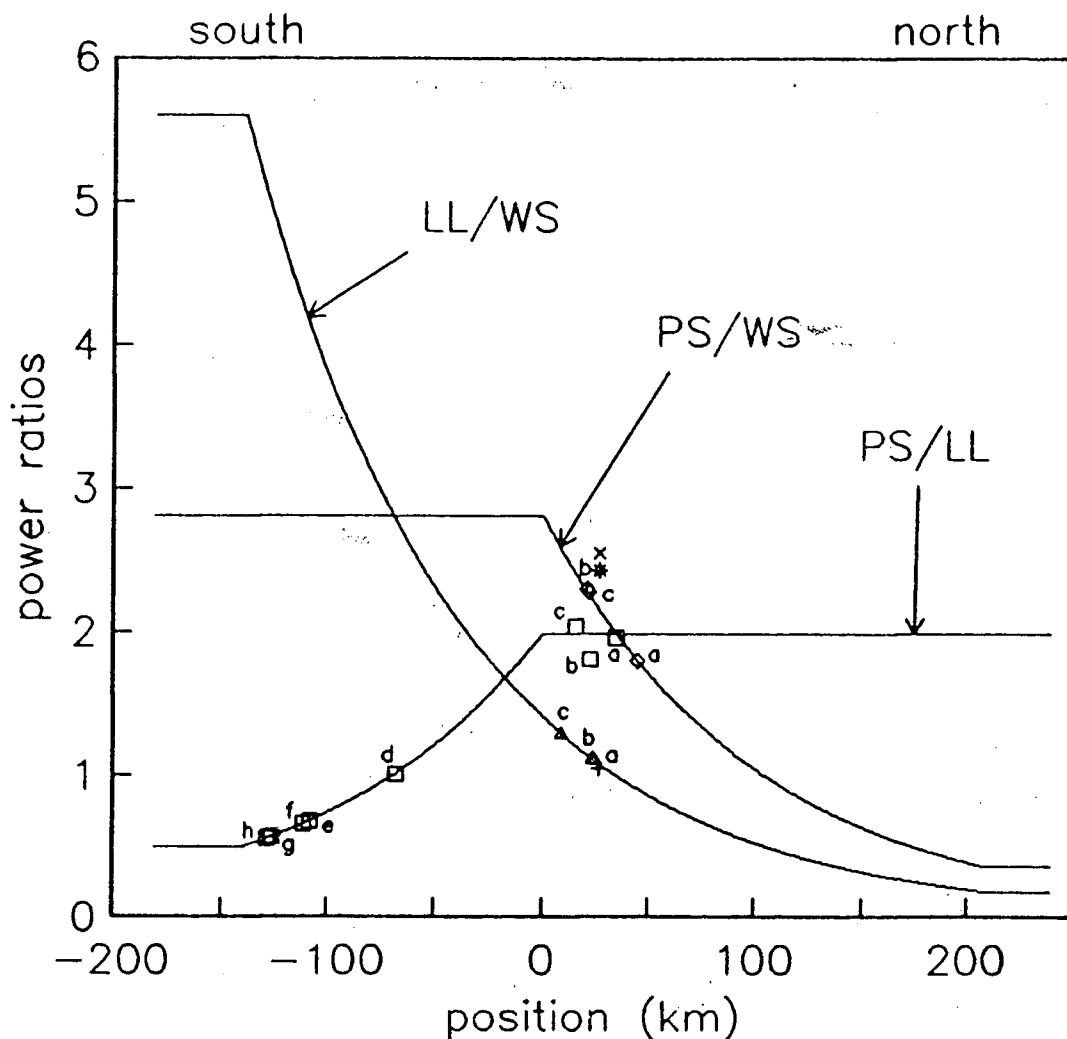


FIGURE 30.

Theoretical power ratio versus position curves for the PS/WS, PS/LL, and LL/WS station pairs. The Λ value used here is that calculated from the Y component of the Feb. 14 event. The letters (a-h) indicate the experimental points with times (UT) and frequency (Hz) as follows: a-0835,0.50; b-0840,0.56; c-0850,0.59; d-0915,0.75; e-0920,0.84; f-0930,0.87; g-0935,0.89; h-0940,0.89. The points indicated by x, *, and + are also from 0840UT, but different from the points labelled b above by being from a lower frequency band ($< 0.5\text{Hz}$) (see text). The positions for the points on the horizontal branch are determined from the other power ratio(s) for that time. Position in this plot is centered at PS.

power ratios are also marked in figure 30. Note that the theoretical plot shows that the PS/LL power ratio is constant while the secondary source is north of PS, and that the experimental PS/LL ratios are also relatively constant until $\approx 0910\text{UT}$, thus confirming the polarization spectrogram result that the secondary source is north of, or in the vicinity of, PS until $\approx 0910\text{UT}$. That these power ratios lie on or near the horizontal branch of the theoretical curve also demonstrates that the exponential signal decay model (cf. equation 5.1) is appropriate for the analysis of this event, or at least for the majority of it which has frequencies above 0.5Hz. If signal decay were due to geometrical spreading as expressed in equation 5.2, no such horizontal branch would exist and the PS/LL power ratios should decrease with increasing secondary source distance north of PS. Figure 30 also includes power ratios calculated from the signal band below 0.5Hz at 0840UT and indicated by x (PS/WS), * (PS/LL), and + (LL/WS). Since these signals are below 0.5Hz, they should not be affected by ionospheric propagation. Thus, as expected, they do not lie on the theoretical curves, except for the LL/WS ratio point. In the case of this LL/WS point, the secondary source position happens to be almost exactly half way between LL and WS resulting in a power ratio near 1 and a ratio position near the theoretical curve. The position estimate from this low

frequency point is 27km north of PS for 0840UT, just slightly different than the 23km north estimate made from the signal band above 0.5Hz. The method used for estimating secondary source positions when IPDP signal decay is due to geometrical spreading is described in detail in the discussion of the Feb. 15 event below (cf. section 5.1.2). It should also be noted here that the power and frequency values used in the secondary source position analysis are taken from the peaks in the spectra, the frequencies of which are generally near the IPDP mid-frequency.

The secondary source position can now be determined by matching the three station pair power ratios, when each is available, to the theoretical curves, and reading the position associated with that ratio from these curves. This method assumes that, on each meridian, the secondary source can be approximated by a point source. This is reasonable since the plasmopause, the primary source region (cf. section 4.1), is probably less than $0.15R_E$ across, with the plasma density increasing from 1 to 100 cm^{-3} over this distance (Jacobs, 1970). The main region of IPDP wave growth, (i.e. that part responsible for the spectral peak), likely covers only a small portion of this $0.15R_E$ range. If it covered only $\frac{1}{10}$ of this range, the radial dimension of this part of the magnetospheric generation region would be $\approx 100\text{km}$. When this range is mapped down the converging field

lines to Earth's surface, the range along the meridian becomes only $\approx 6\text{km}$, or 0.05° , at the latitude of PS.

For the Feb. 14 IPDP, secondary source positions have been determined before 0900UT using both the PS/WS and LL/WS power ratios. Reasonable agreement was obtained between the positions found from each of these two ratios at each point (see fig. 30). After 0910UT, however, only the PS/LL ratio was available, since the signal strength at WS was too weak to produce reliable results. Though spectral estimates were made from data blocks centered every five minutes throughout the event, source location points do not appear at each of these times. This is due to intervals of very low signal/noise ratio, and also to periods of mismatched, or dissimilar spectra at the various stations. These periods are possibly indicative of temporary poor signal propagation, slight signal differences caused by the small longitudinal differences between the stations (cf. sec. 5.4), or the L-spread of the IPDP source region mentioned earlier.

The positions of the IPDP secondary source, as determined by the above method, for the Feb. 14 IPDP are presented in figure 31 in terms of corrected geomagnetic latitude (Gustafsson, 1984). Also shown are the equivalent equatorial radial positions, in L, of the magnetospheric source region. In addition to these data points, a point at

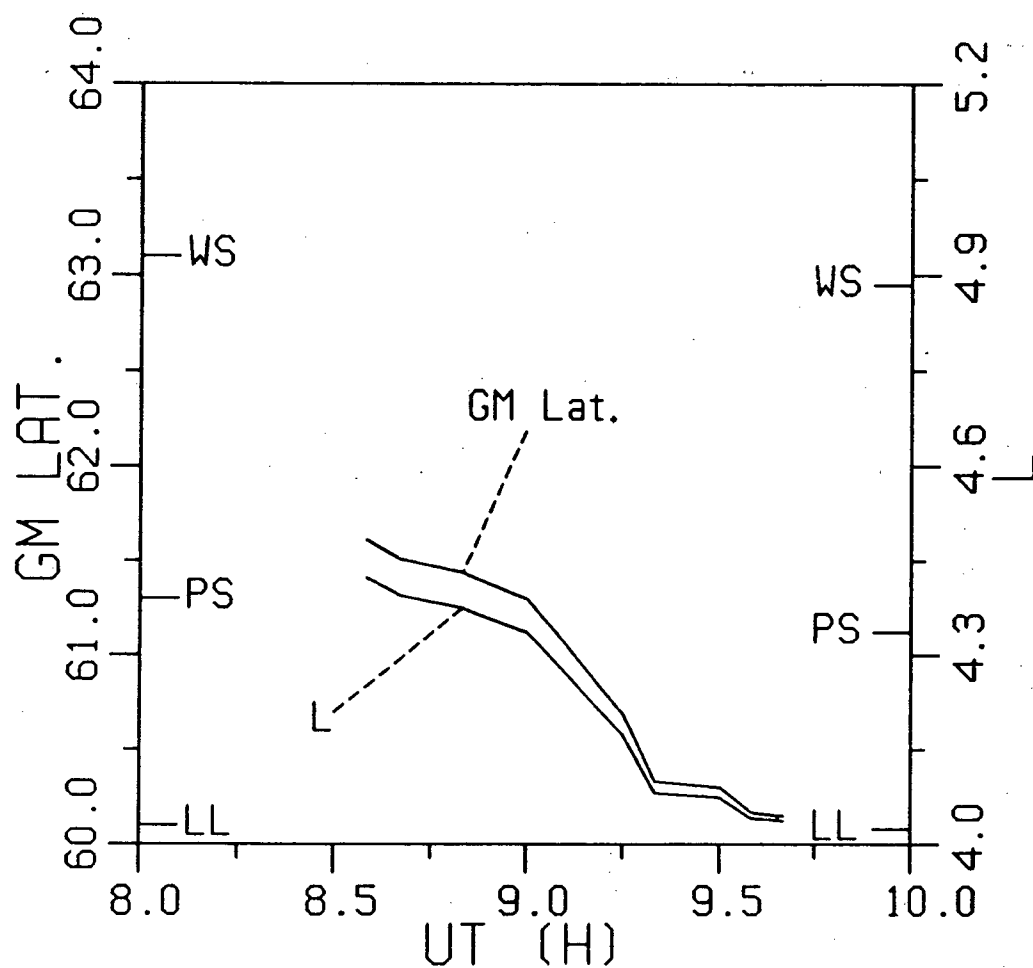


FIGURE 31.

Geomagnetic latitude and equatorial radial position (L), respectively for the secondary and magnetospheric sources; Feb. 14 IPDP. Station locations are also shown. The source region inward motion is clearly evident.

0900UT has been added directly over PS. The PS polarization spectrograms show LH polarization in the center of the IPDP frequency band at this time, which indicates that the secondary source is overhead of the site. These results show a clear inward motion trend for the magnetospheric source region of this IPDP event.

The effect of this inward motion on the IPDP event's frequency evolution can be estimated using equation 4.5 (cf. section 4.2.1). The frequency rise due to decreasing L predicted by this is shown in figure 32, along with the actual frequency rise observed during the Feb. 14 event. In this figure, and in all the following frequency shift analyses, we use frequency normalized to the initial value of the event under study (f/f_i). It is evident that the inward motion effect produces a significant amount, approximately $\frac{2}{3}$, of the frequency rise of this IPDP, but certainly cannot be said to account for it all.

5.1.2. Feb. 15 Event

The second event studied, that of Feb. 15, was also observed on the three southernmost stations of the Saskatchewan line. The analysis procedure for this IPDP is generally the same as that for the Feb. 14 event, including the necessity of using the Y component data only. However, some procedural adjustment is required by the different

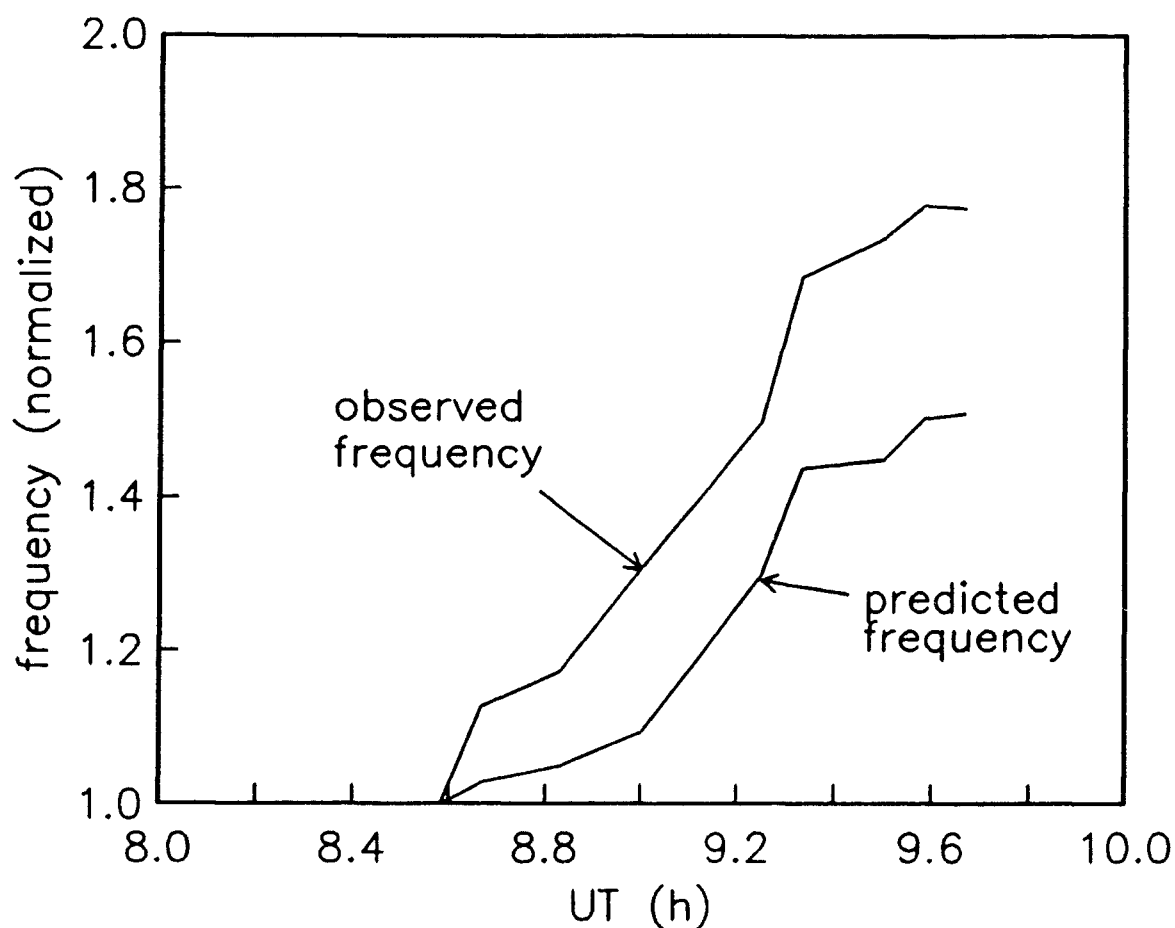


FIGURE 32.

Observed and inward motion predicted frequency profiles for the Feb. 14 event. The frequencies are normalized to the observed initial frequency of 0.50Hz at 0835UT. The inward motion predicted frequency rise accounts for $\approx \frac{2}{3}$ of the observed rise. Note that the forms of the two curves are quite similar, however.

signal characteristics of this event.

The inspection of polarization spectrograms for this event indicates that the lower cut-off frequency for ionospheric propagation is $\approx 0.25\text{Hz}$ (for example, see fig. 33), rather than $\approx 0.5\text{Hz}$ as for the previous event. Figure 34 shows polarization spectrograms from PS and LL at 2201UT, at which time the IPDP signal occupies the frequency band from ≈ 0.35 to $\approx 0.5\text{ Hz}$. These spectra show that both events are RH at this time, thus indicating that the secondary source is over neither site. (It is actually roughly half way between them, see below).

In spite of this lower cut-off, the entire event cannot be treated as a ducted wave problem since the initial IPDP frequency is $< 0.25\text{Hz}$. For the initial low frequency point, at 2149UT, the power decrease with distance from the secondary source is then likely due to geometrical spreading. In such a situation, with no propagation effects from the ionosphere or the Earth, the signal power (P) should depend on distance (d) as:

$$P \propto \frac{1}{d^x} \quad (5.2).$$

The exponent x would be 2 for a point source and 1 for an infinitely long line source. Since each station is likely to

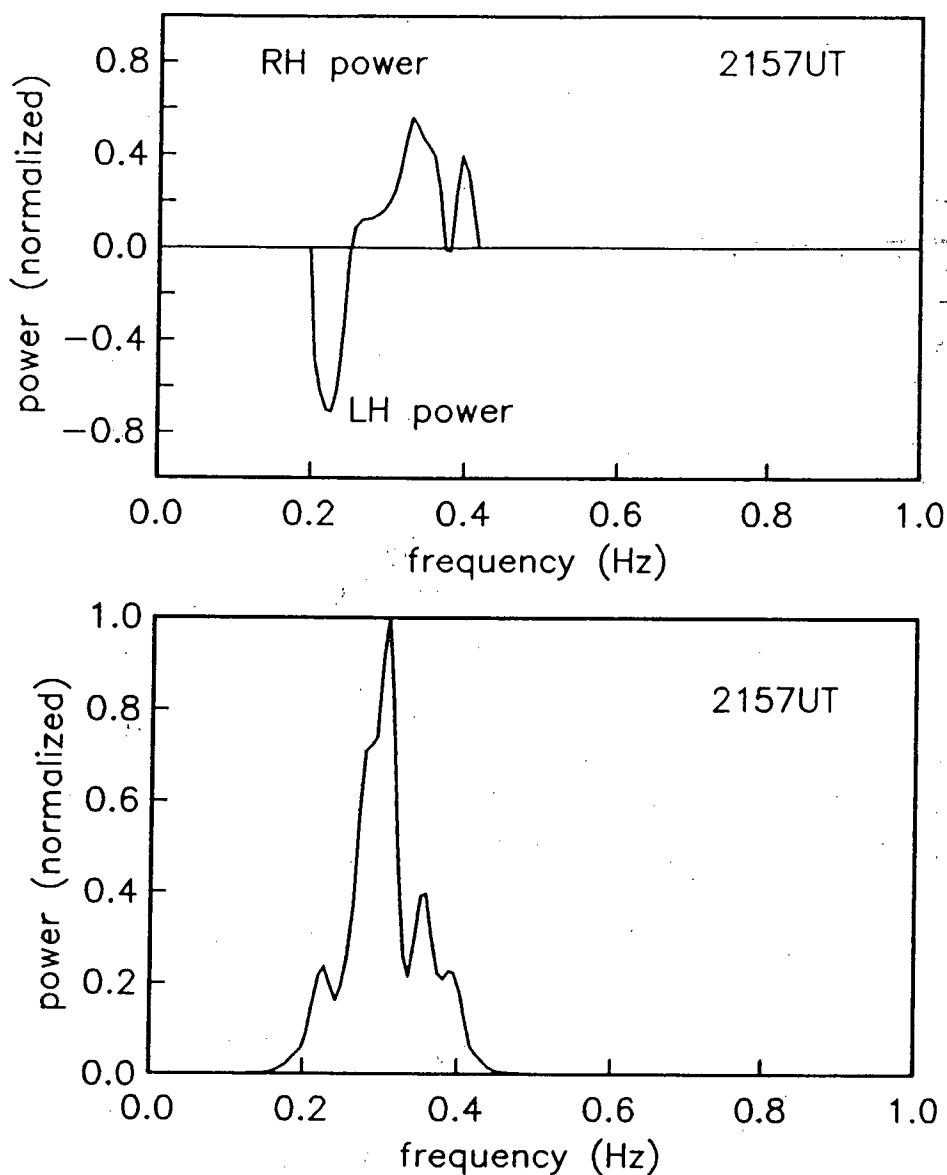


FIGURE 33.

Polarization spectrogram (top) and power spectrum (total horizontal component) (bottom) from PS for 2157UT, Feb. 15. The polarization spectrogram is again presented as [polarized power]/[horizontal component power]. The change from LH polarization at lower frequencies to RH polarization at ≈ 0.25 Hz indicates the position of the duct lower cut-off frequency.

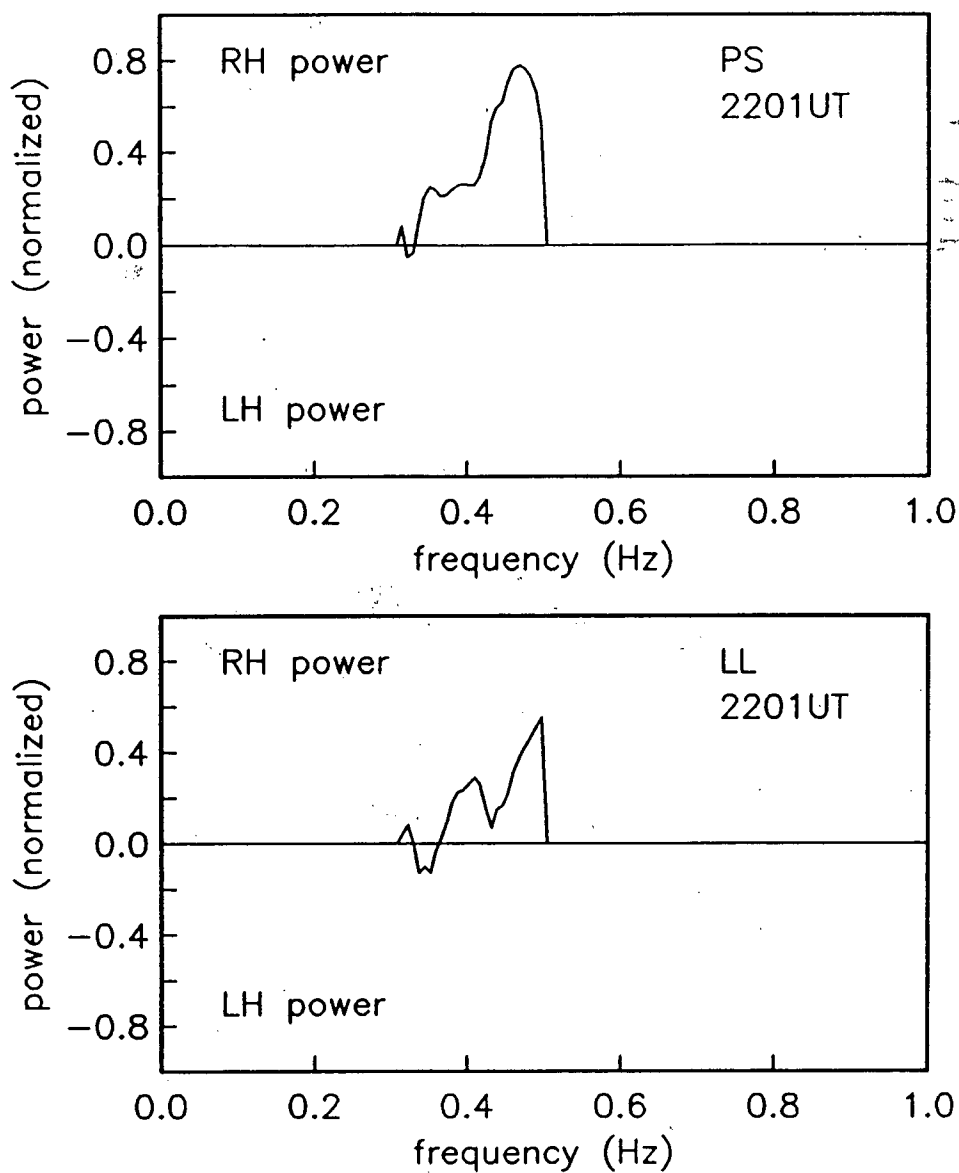


FIGURE 34.

Polarization spectrograms from PS (top) and LL (bottom) for 2201UT, Feb. 15. These spectrograms are presented as in figure 33. The secondary source is over neither site at this time.

be receiving signals from more than just its own meridian for non-ducted waves (see fig. 35), the actual exponent will fall in the range of $1 < x < 2$, that is, the source can be approximated by a line of finite length. Assuming a particular source location with respect to the stations along the stations' meridian, it is possible to write three equations for the secondary source position using the three power ratios. These equations express secondary source position in terms of distance north or south of PS. The following equations are for the geometry of figure 35:

$$d_1 = \frac{209}{(PS/WS)^y + 1} \quad (5.3a)$$

$$d_2 = \frac{139}{(PS/LL)^y - 1} \quad (5.3b)$$

$$d_3 = \frac{348}{(LL/WS)^y + 1} - 139 \quad (5.3c)$$

where $y = 1/x$ and the d_i 's represent distance north of PS. For each x between 0.20 and 4.00 (increment size = 0.01), each d_i above, plus the sum of the errors

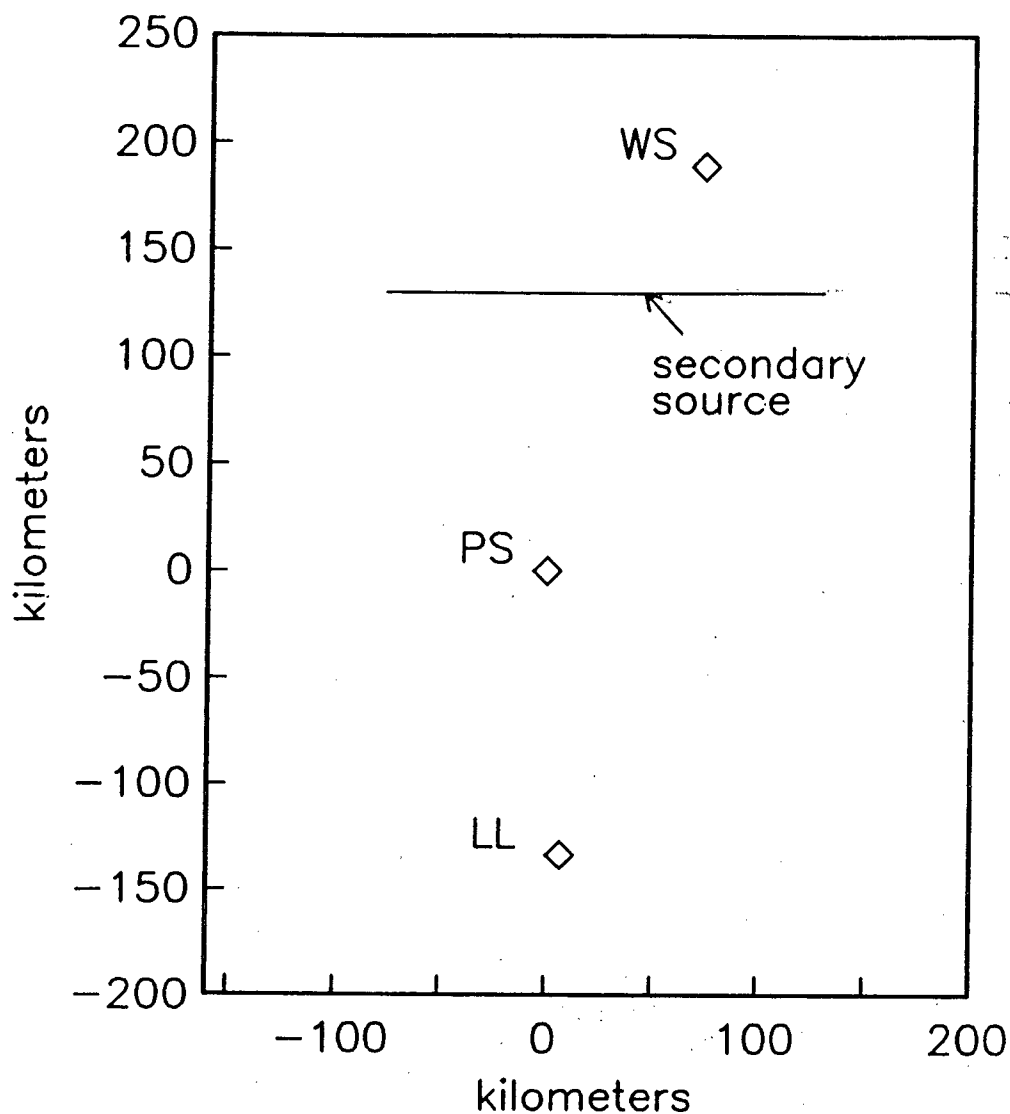


FIGURE 35.

Source - station geometry for the Feb. 15 IPDP at 2149UT. The secondary source line is a segment of the plasmopause mapped down field lines to the ground. The segment is assumed to be centered on the stations' meridian so the source distance calculations yield positions directly north or south of PS. The position of PS is centered at 0km, with LL 139km south and WS 209km north.

$$e = ((d_1 - d_m)^2 + (d_2 - d_m)^2 + (d_3 - d_m)^2)^{\frac{1}{2}}$$

(where $d_m = (d_1 + d_2 + d_3)/3$), were calculated. The result is shown in figure 36, indicating very good convergence of the three position estimates at $x = 1.44$ and $d = 152\text{km}$ north of PS. No convergence of the three position estimates occurs with other source-station geometries. For example, having the secondary source north of WS or south of LL, for which the equations 5.3a,b,c must be modified slightly, yields no consistent position estimate.

Also shown in figure 36 are the results of the same calculations carried out using the power ratios from 2157UT, a time when the IPDP signal is propagating in the ionospheric waveguide. Here, the exponent (x) giving the best d_i convergence is 0.76, outside the expected range, and e at this point (e_{min}) is 12.42km, 20 times greater than e_{min} for the 2149UT calculation. It should be noted at the e_{min} point for the 2157UT case, two of the d_i 's are virtually identical, while the third is significantly ($\approx 15\text{km}$) different. For this 2157UT calculation, when $x = 1.44$ (the 2149UT e_{min} point), $e = 130\text{km}$. These results, which are typical of all the data points after 2149UT, demonstrate that this method of secondary source determination is not appropriate when dealing with ducted waves.

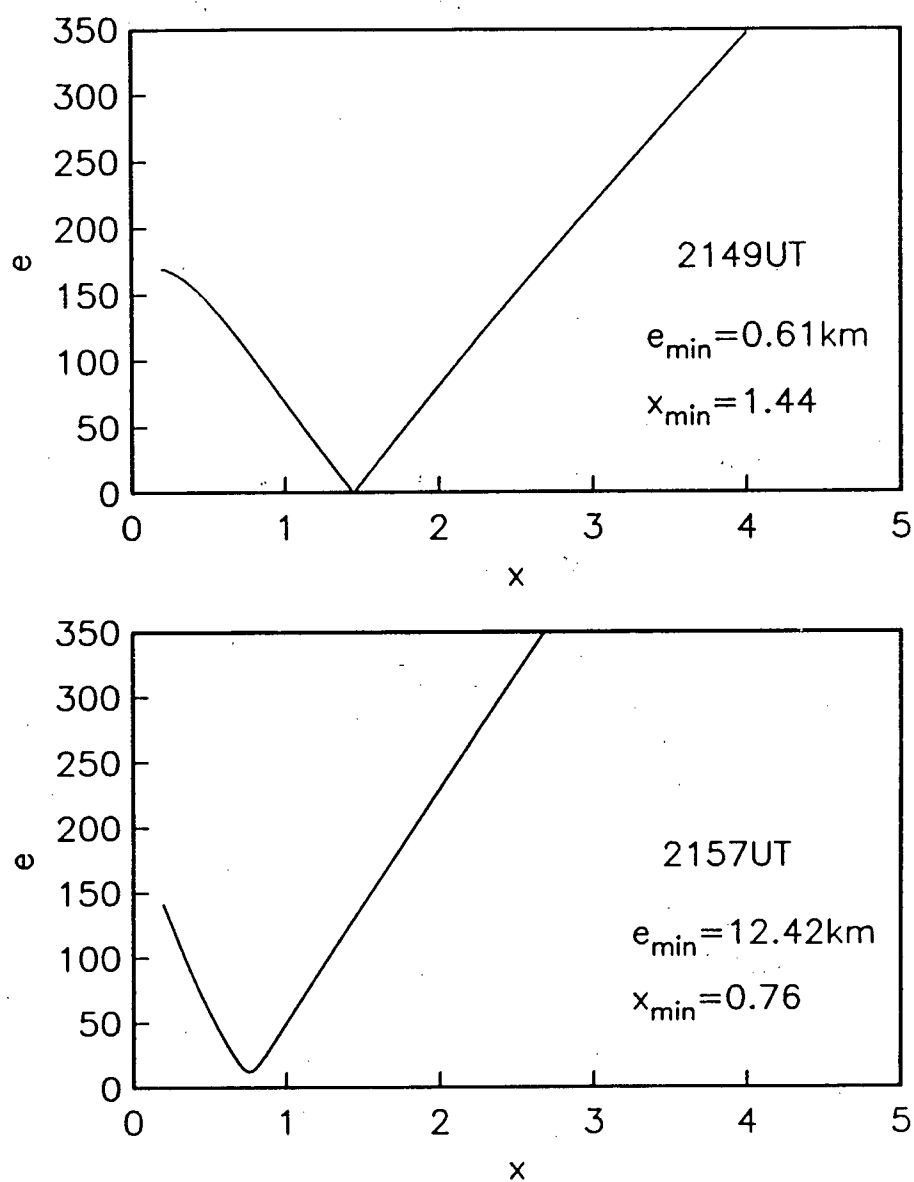


FIGURE 36.

Sum of the errors (e) versus exponent (x) for 2149UT (top) and 2157UT (bottom); Feb. 15 event. At 2149UT, e is minimum at $x = 1.44$, corresponding to a source position 152km north of PS (from equations 5.3a - 5.3c).

The above method was then necessary for only the first point of the Feb. 15 IPDP, at 2149UT. For the remaining four points, at 2152 to 2205 UT (cf. fig. 37 caption), the secondary source position was found using the same method as for the Feb. 14 event. The attenuation factor determined here was 30.6 ± 2.8 dB/1000km.

It is interesting to note that the ionospheric propagation conditions are quite different for this IPDP than for the Feb. 14 event. The attenuation is 50% greater here, and the lower cut-off frequency only $\frac{1}{2}$ that for the previous event. This may be a result of the different local times of the two events; the Feb. 14 event occurred during the night, while the Feb. 15 event appeared while the ionosphere was in sunlight, which can substantially alter the ionospheric plasma characteristics including the ducting parameters.

Figure 37 shows the power ratio profiles for $\Lambda = 30.6$ dB/1000km plus the experimental points for the Feb. 15 IPDP. As in the Feb. 14 event, the points on or near the horizontal branches in figure 37 show that the exponential decay model (cf. equation 5.1) is appropriate at frequencies above the cut-off of ≈ 0.25 Hz for this event. That the points for 2149UT in this figure are not on the theoretical power ratio curves also indicates that this low frequency point cannot be treated in this manner. If we were to interpret

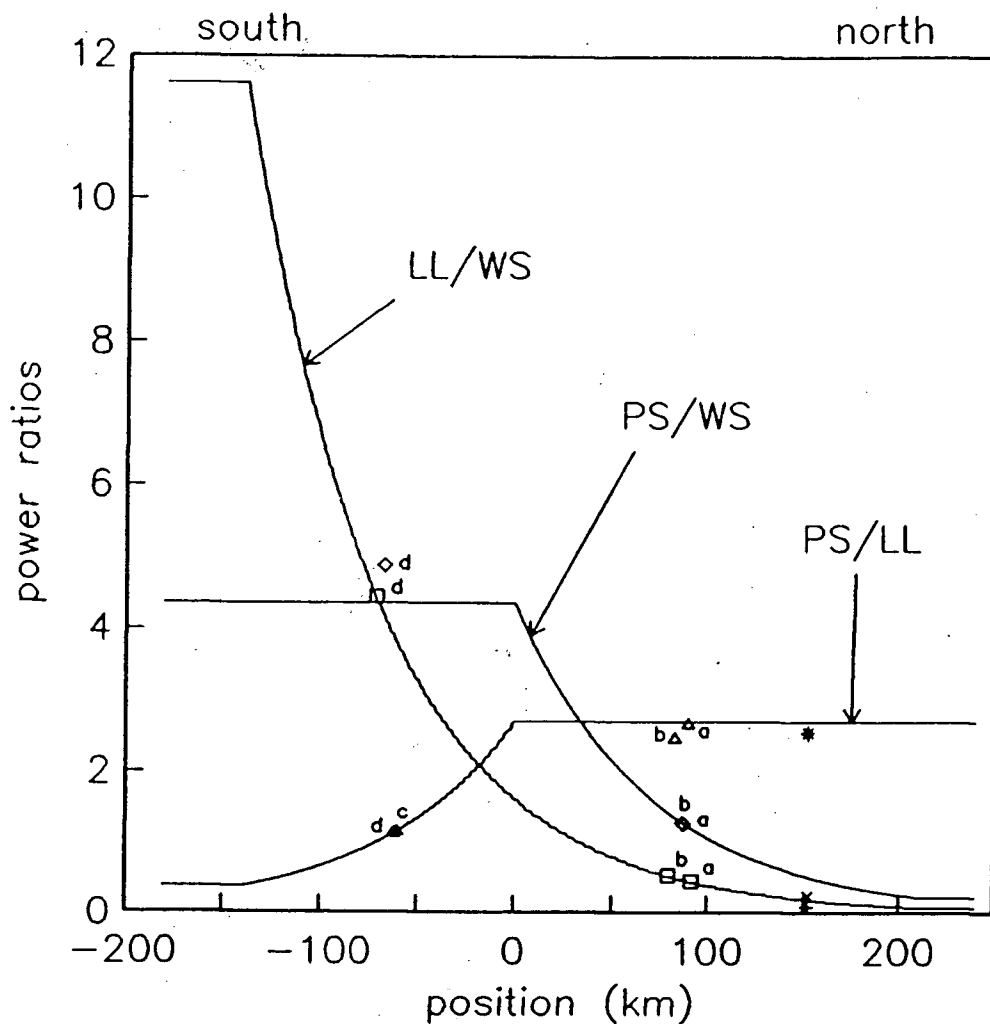


FIGURE 37.

Power ratio versus position profiles for the PS/WS, PS/LL, and LL/WS station pairs. The Λ value used here is that calculated from the Feb. 15 event. The letters (a,b,c,d) indicate the experimental points with times (UT) and frequencies (Hz) as follows: a-2152,0.27; b-2157,0.32; c-2201,0.47; d-2205,0.50. The points marked with x (PS/WS), * (PS/LL), and + (LL/WS) are from 2149UT (freq.=0.22Hz), when the IPDP frequency was below the ionospheric propagation cut-off for this day. The positions of the points on the horizontal branches are determined as in the Feb. 14 event (cf. fig. 30). Position in this plot is centered at PS.

the 2149UT point in terms of exponential decay, the secondary source position estimates would be somewhere north of PS, just south of WS, or somewhere north of WS, depending on the inter-station power ratios used.

The secondary source position results from the above analyses are shown in figure 38, along with the corresponding L positions of the magnetospheric generation region. The inward motion of the generation region is again clear from this plot. The real frequency rise and that predicted from the inward motion are presented in figure 39. Inward source motion accounts for a little more than half, $\approx 60\%$ in this case, of the total frequency rise of this IPDP.

In summary, then, in this section two new methods for determining IPDP source region inward motion using amplitude variations along a north-south line of ground stations have been presented. These methods have been applied to two events, with the results showing that the inward motion mechanism is capable of producing a major portion of an IPDP's frequency rise, though it is not always sufficient, of itself, to explain the entire observed rise of an event.

5.2. MAGNETIC FIELD CHANGES IN IPDP SOURCE REGION

It is evident from section 5.1 that the two IPDPs studied in detail require one or more additional frequency shift mechanisms contributing to their frequency rises

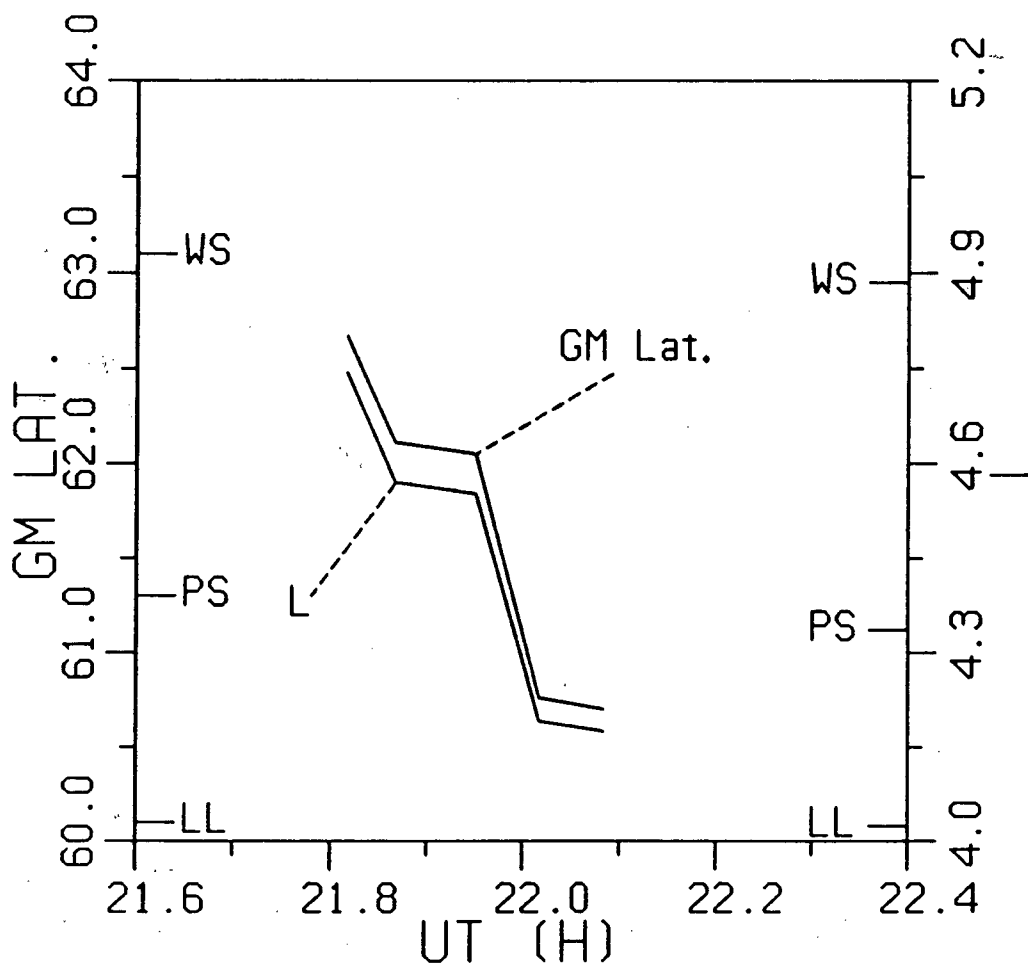


FIGURE 38.

Geomagnetic latitude and equatorial radial position (L), respectively for the secondary and magnetospheric sources; Feb. 15 IPDP. Station locations are also shown. As with the Feb. 14 event, this IPDP also shows clear source region inward motion.

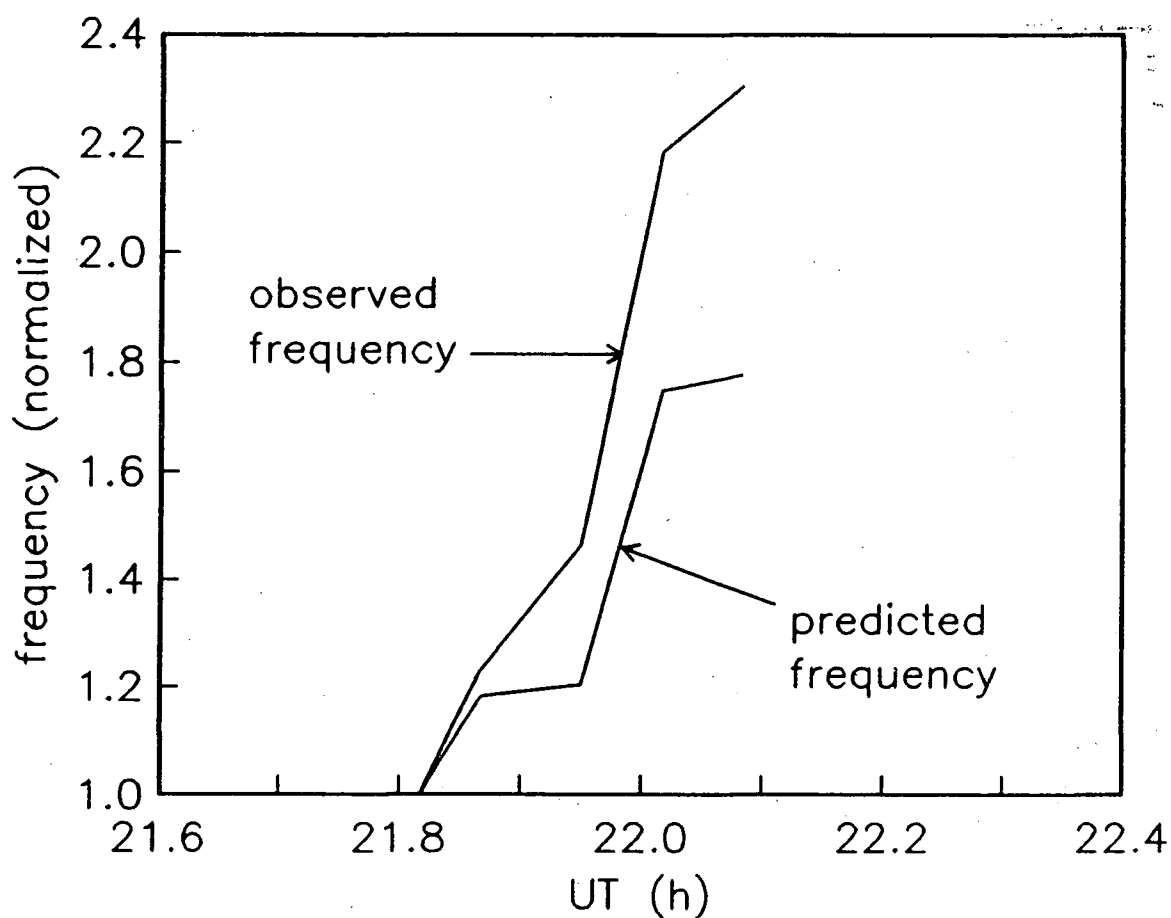


FIGURE 39.

Observed and inward motion predicted frequency profiles for the Feb. 15 event. The frequencies are normalized to the initial frequency of 0.22Hz at 2149UT. Here, the inward motion mechanism accounts for only $\approx 60\%$ of the observed frequency rise, though, as in the Feb. 14 event, the forms of the two curves are quite similar.

beyond the inward motion mechanism already discussed. In this section, the potential contributions of the increasing magnetic field mechanism to IPDP frequency shifts will be assessed, both in general and for the specific events examined in section 5.1. The magnetospheric processes producing the magnetic field changes in the IPDP source region are described below. The analysis of these processes here represents a more sophisticated approach than that discussed briefly in section 4.2.2, though the dependence of IPDP frequency on magnetic field strength is the same (cf. equation 4.6). Comparisons of geosynchronous satellite magnetograms, from GOES 2 and 3 (whose meridians correspond approximately to the Saskatchewan and British Columbia lines, respectively; cf. section 2.1), and Dst indices (cf. Appendix C) with the ground station IPDP records are used to gain some understanding of the effects of this frequency shift mechanism.

5.2.1. Ring Current Versus IPDPs

The IPDP generation region is typically in the evening sector between $L \approx 3$ and $5\frac{1}{2}$. The source of magnetic field variations in this region considered here is the ring current since this current can strongly influence magnetic field behaviour in the IPDP source region and its formation is directly related to the substorm processes which are also

necessary to create IPDPs (cf. section 4.1). This ring current forms during magnetospheric storms and is carried by westward drifting protons. Since the ring current is directed westward, the magnetic field is depressed earthward of the current and enhanced outside of it.

The magnetic effects of the ring current can be monitored both at geosynchronous orbit ($L = 6.6$) and at equatorial ground stations ($L = 1$). These records clearly show the magnetic field at $L = 6.6$ becoming depressed earlier than at the ground, and then recovering to near quiet time levels while the ground stations still show a strongly depressed field. This indicates that the ring current initially forms outside $L = 6.6$, and then, over the course of several hours, moves inward during the storm to $L < 6.6$ (Nishida, 1978). This result is also supported by the ring current observations and generation model of Lyons and Williams (1980). On the night side, the effect of the cross-tail current field, which is oppositely directed to the ring current field outside of the ring current, prevents the magnetic field at geosynchronous orbit from rising much above the quiet day level as the ring current moves inside $L = 6.6$. The magnetic field effect of this cross-tail current, is, however, small compared to the ring current field at lower L (Kawasaki and Akasofu, 1971). Therefore, it is the growth, movement, and decay of the ring current which

controls magnetic field changes in the IPDP source region, and it is these processes which are examined in order to understand the role of the increasing background magnetic field frequency shift mechanism.

Though IPDPs usually occur within $L = 6.6$, geosynchronous satellite magnetograms, along with the Dst index which reflects the effect of the ring current magnetic field at near-equatorial ground stations ($L = 1$), can be useful in estimating the magnetic field behaviour in the IPDP generation region. As the ring current forms outside $L = 6.6$, the field at $L = 6.6$ will be decreasing, though this current may not yet show up as a negative excursion of the ground-based Dst index. Since the magnetic field is either decreasing or constant at virtually all L 's at which an IPDP could be generated, an event occurring at this time should not take place during an interval of increasing magnetic field. Therefore, the increasing field mechanism could not account for the observed frequency rise of events occurring under these conditions. Even as the ring current moves earthward towards $L = 6.6$, the field at the lower L 's where most IPDPs are generated should not be increasing and the above conclusion holds true here as well. These types of conditions were quite likely in effect for those 83% of high latitude IPDP events which were observed by Bossen et al. (1976) simultaneously at the geosynchronous satellite ATS-1

and Tungsten, Northwest Territories, which is near the same field line as ATS-1, when the magnetic field at ATS-1 was either decreasing or constant (cf. section 3.5). Part (a) of figure 40 shows a sketch of the magnetic field changes that would occur as the ring current forms outside $L = 6.6$; in this example, at $L \approx 7$. Note that the changes from the pre-ring current formation level, represented by the solid line labelled t_0 in figure 40, to the point where the ring current has formed at $L \approx 7$, shown by the dashed line labelled t_1 , are negative at all L 's on which IPDPs are commonly generated. Though the diagrams in figure 40 are only sketches representing a rough guide to ring current magnetic field behaviour, the profile shapes follow approximately those calculated by Kawasaki and Akasofu (1971) and Berko et al. (1975).

If the ring current has moved inside $L = 6.6$, it becomes more difficult to follow the magnetic field behaviour in the IPDP generation region. In this case, an increasing field at geosynchronous orbit does not necessarily imply an increasing field everywhere Earthward of $L = 6.6$. The rise at $L = 6.6$ may simply be due to being on the outward side of the ring current, where the magnetic field is recovering back towards its normal level (see fig. 40, part (b)). Some light can still be shed on this situation with the use of the Dst index, however. Note that

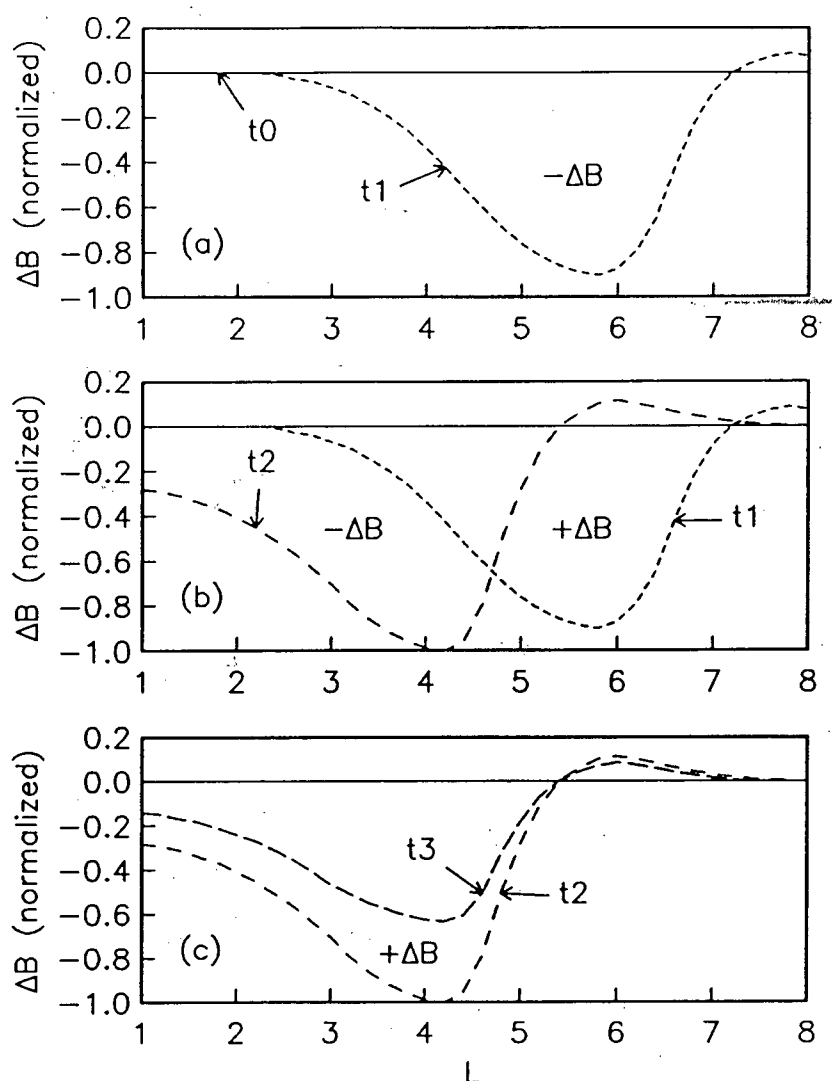


FIGURE 40.

Sketches outlining the magnetic field changes during ring current evolution, including the formation (a), the inward movement (b), and the decay of the ring current (c). The relative times of each of the ΔB profiles are labeled, with $t_0 < t_1 < t_2 < t_3$. The overall time scale for the magnetic field variations shown here is generally several hours to several days, depending on the storm conditions. The regions where the magnetic field is increasing or decreasing during each stage are also labelled.

the Dst index is composed of hourly values, which is also the time scale of many IPDP events. This does not pose a problem, however, because of the slow variation of the ring current, the primary source of longer term variations at the lower L-shells (Kawasaki and Akasofu, 1971) on which most IPDPs are generated, which makes hourly intervals sufficient to characterize it (Mayaud, 1980). If other, shorter period (<1 hour) magnetic field variations exist, they could adversely affect this type of IPDP analysis, though magnetograms from geosynchronous orbit showed no variations of this type large enough to significantly affect IPDP frequency during the events studied.

Discussed below are four possible Dst versus IPDP cases illustrating magnetic field behaviour in the IPDP source region during different phases of ring current evolution.

I. If the Dst index is positive, or negative but still near zero having just begun its stormtime decrease, then it is likely that the ring current is comparatively further out and is still developing. An IPDP occurring at this time would most likely see a decreasing or, if at low L where the current effects are not yet strongly felt, possibly constant magnetic field.

II. If the Dst index is well into its decrease, then the ring current should be further inward as well. Equatorial ground stations do not show a strong field

depression until the ring current has moved inside geosynchronous orbit ($L = 6.6$) (Nishida, 1978), and Lyons and Williams (1980) also infer ring current inward motion as the Dst depression is formed. IPDPs at higher latitudes, that is, higher L , would then be, if the ring current has already moved past their generation region, in an area of increasing magnetic field strength. Lower latitude IPDPs would still see a decreasing field as the current develops and moves inward towards, but not past, their magnetospheric source regions. Part (b) of figure 40 shows the effects of moving the ring current from $L \approx 7$ (t_1) to $L \approx 5$ (t_2), where the field depression reaches $L = 1$ implying that the Dst index is also depressed. Between times t_1 and t_2 the magnetic field has risen over the L range of 5 to 7, providing an increasing field during high L IPDPs, and dropped for $L < 5$, showing a decreasing field to any IPDPs generated within this range.

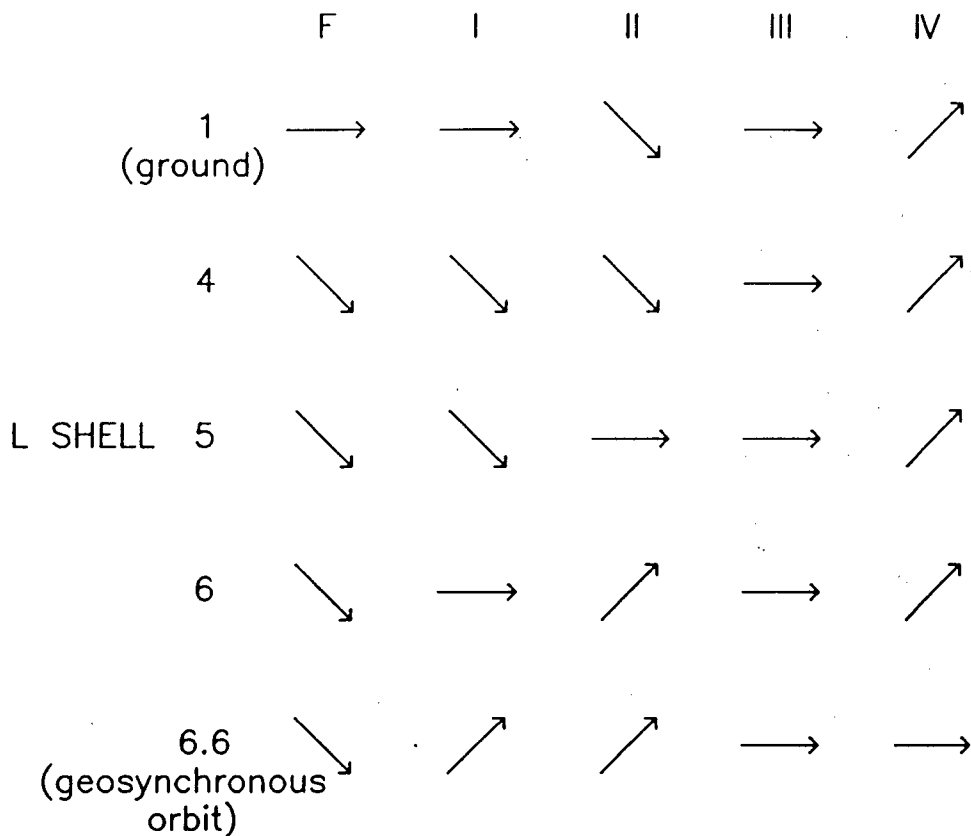
III. If the Dst index has completed its drop and is relatively stable, that is, the index changes relatively little during the event and any small changes which do occur are not part of a general increasing or decreasing trend, then the magnetic field will be essentially constant in all regions dominated by the ring current.

IV. If the Dst index is undergoing a general recovery back towards quiet time levels, then the field, which has

been severely depressed out to $L \approx 5-6$, will be rising in the IPDP generation region. This is illustrated in part (c) of figure 40. As the ring current weakens between times t_2 and t_3 , the magnetic field recovers towards quiet time levels at all affected L shells, including the Dst index at ground level ($L = 1$).

Figure 41 demonstrates these four cases, plus the initial ring current formation phase, indicating the field behaviour at the ground (Dst) and at four L shells as the ring current forms, moves inward, and decays. This figure should be regarded only as an approximate and qualitative guide to ring current magnetic field behaviour. Field profiles relevant to individual situations may vary to some degree from these cases. Also, the divisions among the case types are only roughly defined, and interpolation between these described situations would be necessary for a full understanding of all magnetic field behaviour patterns possible during IPDP events. It must be emphasized that this system of sorting IPDP events into these cases is intended for research convenience only, and does not indicate any fundamental differences in IPDPs across case boundaries.

In each of the cases I through IV above, the magnetic field at geosynchronous orbit will be seen to be increasing or constant (cf. fig. 41), yet only in cases II and IV is it possible that the field in an IPDP's generation region is



F. ring current forming

I. moving inward (early stage)

II. moving inward (later stage)

III. static

IV. ring current decaying

FIGURE 41.

Ring current related magnetic field behaviour in the IPDP generation region. The slope of the arrows indicates whether the field is decreasing, constant, or increasing at each L shell for each case. Case F is the ring current formational phase, and cases I through IV correspond to those discussed in the text.

actually rising as well, thereby contributing to the event's frequency rise. This clearly demonstrates the unreliability of using geosynchronous satellite magnetograms alone for assessing the increasing field mechanism for IPDP frequency shifts, as has previously been done, unless the secondary sources of the events considered are at very high latitude, that is, near 67° GM Lat. or $L = 6.6$ (geosynchronous orbit).

Figure 42 is a plot of Dst versus IPDP occurrence for the period of January 15 to February 25, 1980. Ten IPDPs occurred during this period, including examples of all of the four cases described above. Figure 43 shows a sample of each of these cases with an expanded scale. Even without further analysis it is obvious that an increasing magnetic field cannot be considered a necessary condition for IPDP frequency shifts to occur, because of the existence of case I and III events. The case IV events make it equally obvious, however, that there are situations where the increasing field mechanism can contribute to the IPDP frequency rise.

5.2.2. Individual IPDP Event Assessments

Using the four events from figure 43, a more detailed discussion of individual IPDP events, which exemplify each of the four IPDP versus Dst cases described above, follows.

Feb. 14 Event. The IPDP of Feb. 14 (event no. 6,

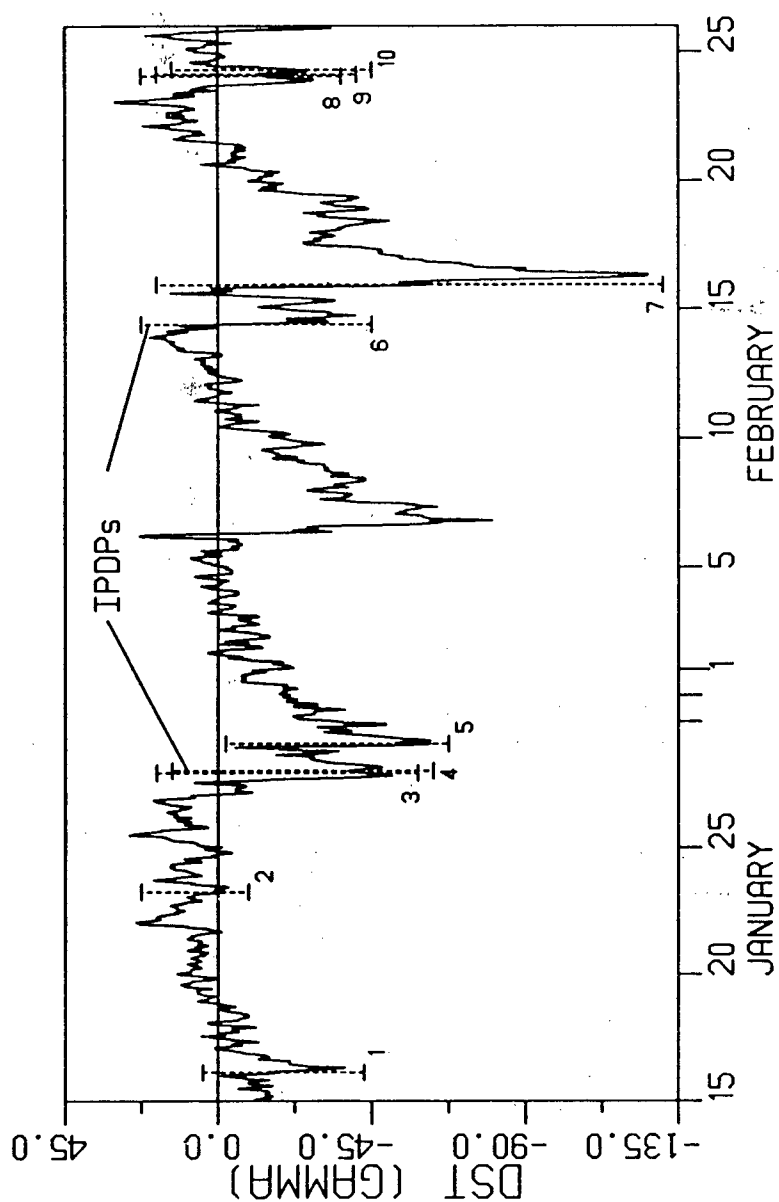


FIGURE 42.

IPDP occurrence versus the Dst index for the period January 15 to February 25, 1980. IPDPs occur in all phases of the ring current development and decay cycle. The IPDP events are numbered as listed in Table IV (Chapter Two).

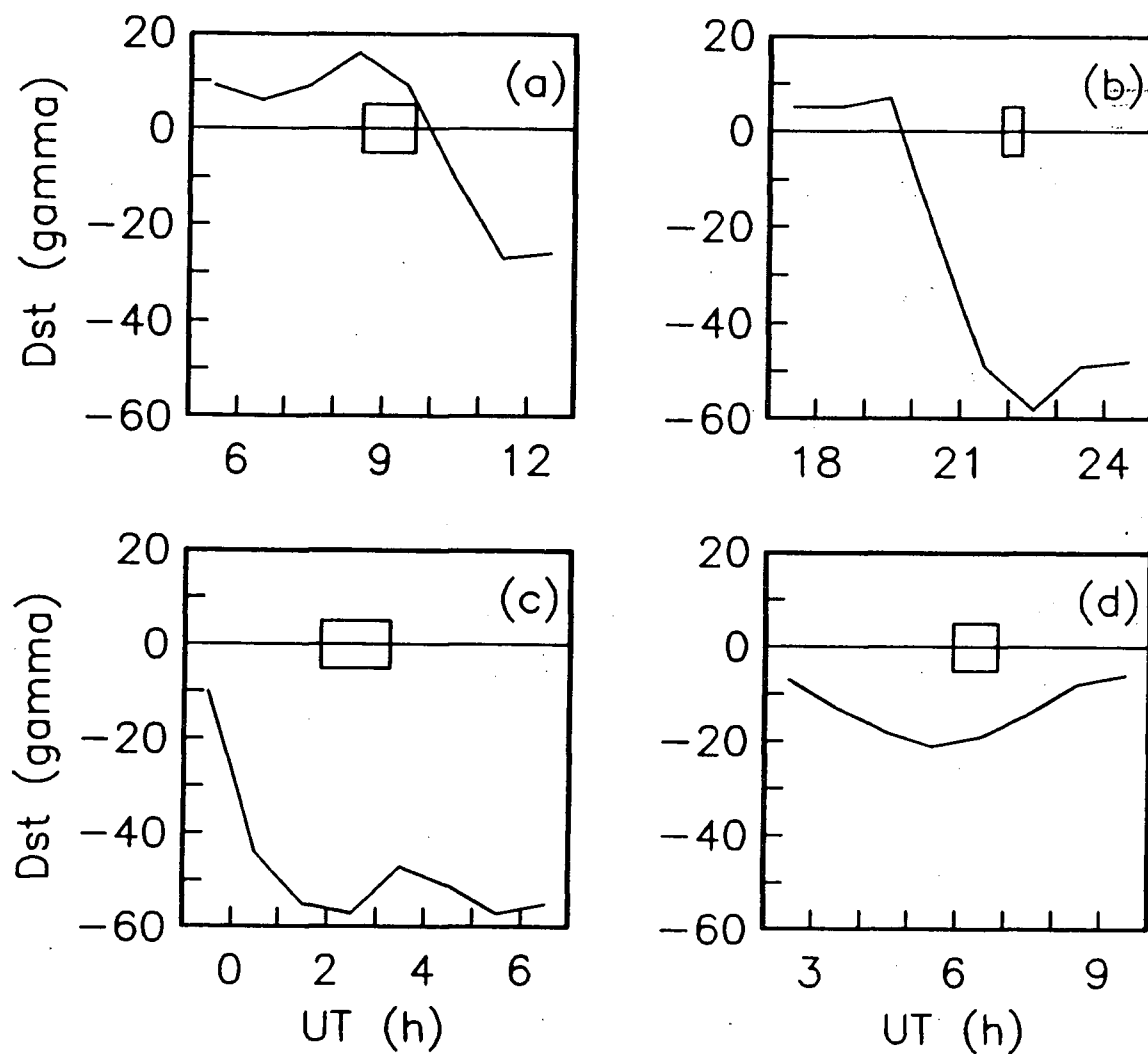


FIGURE 43.

Examples of each of the four IPDP versus Dst cases in larger scale; a) case I; Feb. 14 event, b) case II; Feb. 15 event, c) case III; Jan. 29 event, and d) case IV; Feb. 24c event. The IPDP events occurred in the intervals marked by the boxes.

fig. 42) is an example of a case I event, as are two other events, Jan. 28 and Feb. 24b. In figure 44, it can be seen that the Dst index is above zero for most of the IPDP event, beginning to fall into its large ring current created negative depression only near the event's end (see Appendix C for a discussion of the Dst zero level). Meanwhile, the field (total field strength) at geosynchronous orbit is rising throughout the IPDP event. This combination, according to figure 41, indicates a case I event with the ring current located just earthward of $L = 6.6$ and not yet well developed at lower L shells.

Ground based observations of this event indicate that it was generated within the L range of 4 to $4\frac{1}{2}$ (cf. section 5.1), which is most likely within the decreasing field regime for a case I event (cf. fig. 41). For an event at this low L to see a rising magnetic field, the ring current would have to be at very low L, such as $L \leq 4\frac{1}{2}$, and moving inward, which would create a large Dst depression. Recall that figure 40b, with the ring current moving in to $L \approx 5$, showed ΔB to be still negative at $L = 4 - 4\frac{1}{2}$ while also indicating a significant field depression at ground level (Dst). Since such a depression is not present during this IPDP, it is evident that the increasing field mechanism does not contribute to the frequency rise of this event. It is even possible that the background magnetic field is

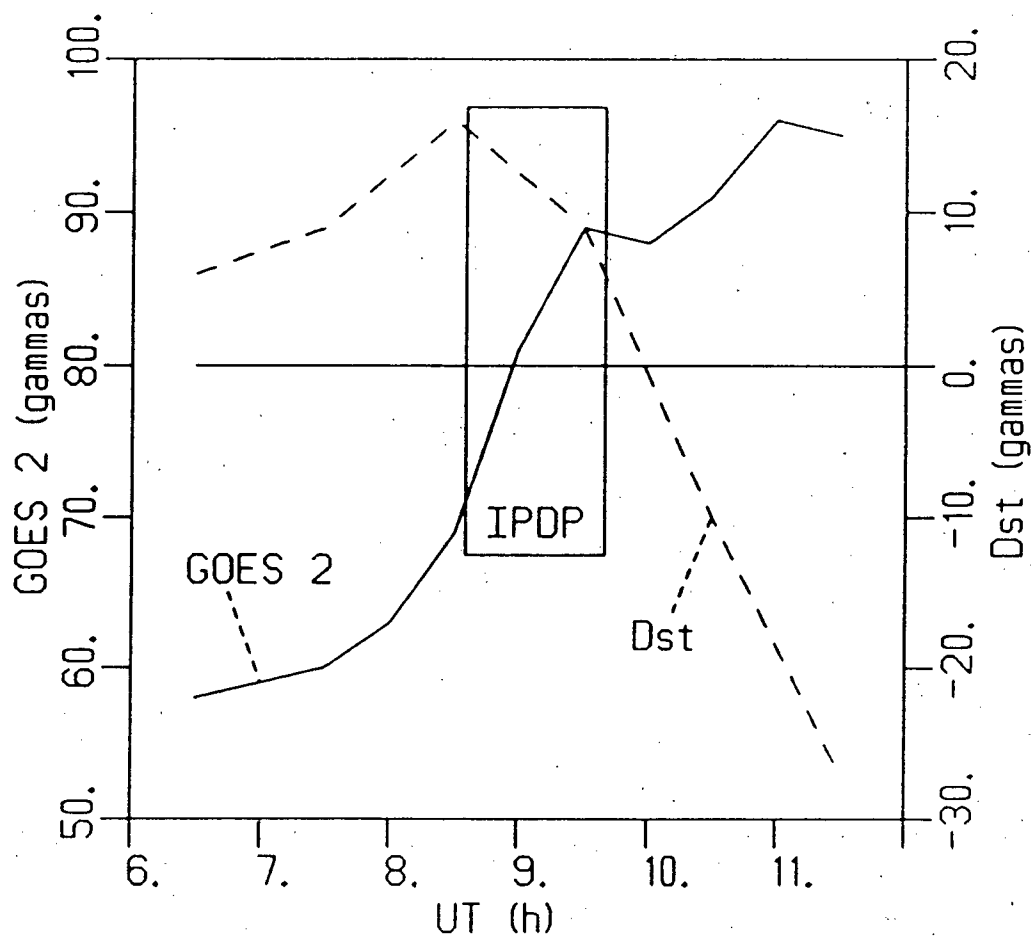


FIGURE 44.

Dst profile and GOES 2 magnetogram (total field strength, BT) for the Feb. 14 IPDP, with the IPDP occurrence time indicated by the box. This is a case I event.

decreasing a little in the IPDP source region, actually suppressing the frequency rise slightly, though due to the low L this is unlikely to be a significant effect for this event.

Feb. 15 Event. Case II is also seen in three events; Jan. 16, Jan. 23, and Feb. 15 (event no. 7, fig. 42). Figure 45 shows the Dst index and geosynchronous satellite magnetograms for the Feb. 15 event. Here, both the Dst and magnetogram are strongly depressed, though the magnetogram shows the beginning of a field recovery at $L = 6.6$ while the Dst continues to drop. This situation implies a case II event, with the ring current further in than the case I event discussed above. Note that the magnetogram is complicated by the onset of a second substorm during the IPDP as shown by the Great Whale River X-component magnetogram in figure 46. This second substorm causes the magnetic field at $L = 6.6$ to begin dropping again after only a slight recovery since the ring current is strengthened outside $L = 6.6$ in the early phase of the substorm (Nishida, 1978). It should be noted that the occurrence of the second substorm makes the proper case assignment less obvious for this event, though since the situation began as a typical case II type before the complications occurred, this (case II) assignment has been made.

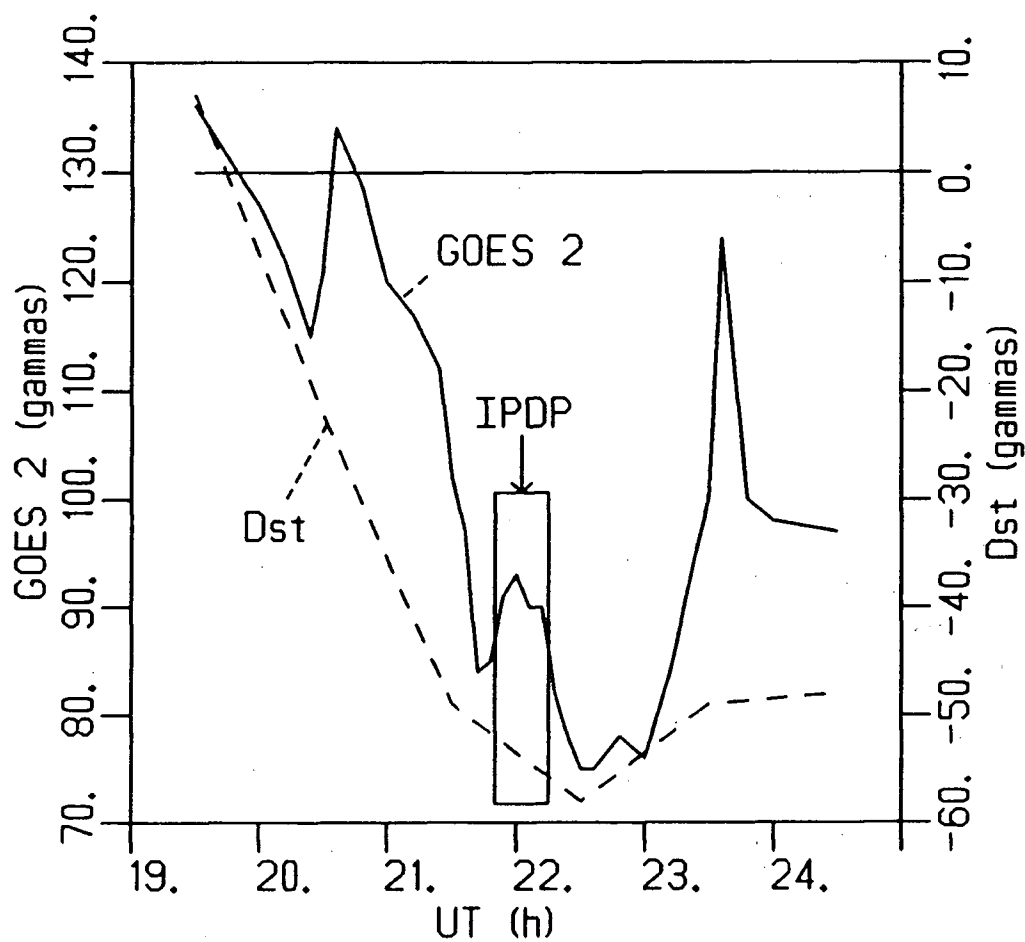


FIGURE 45.

Dst profile and GOES 2 magnetogram for the Feb. 15 IPDP, with the IPDP occurrence time indicated by the box. This is a case II event.

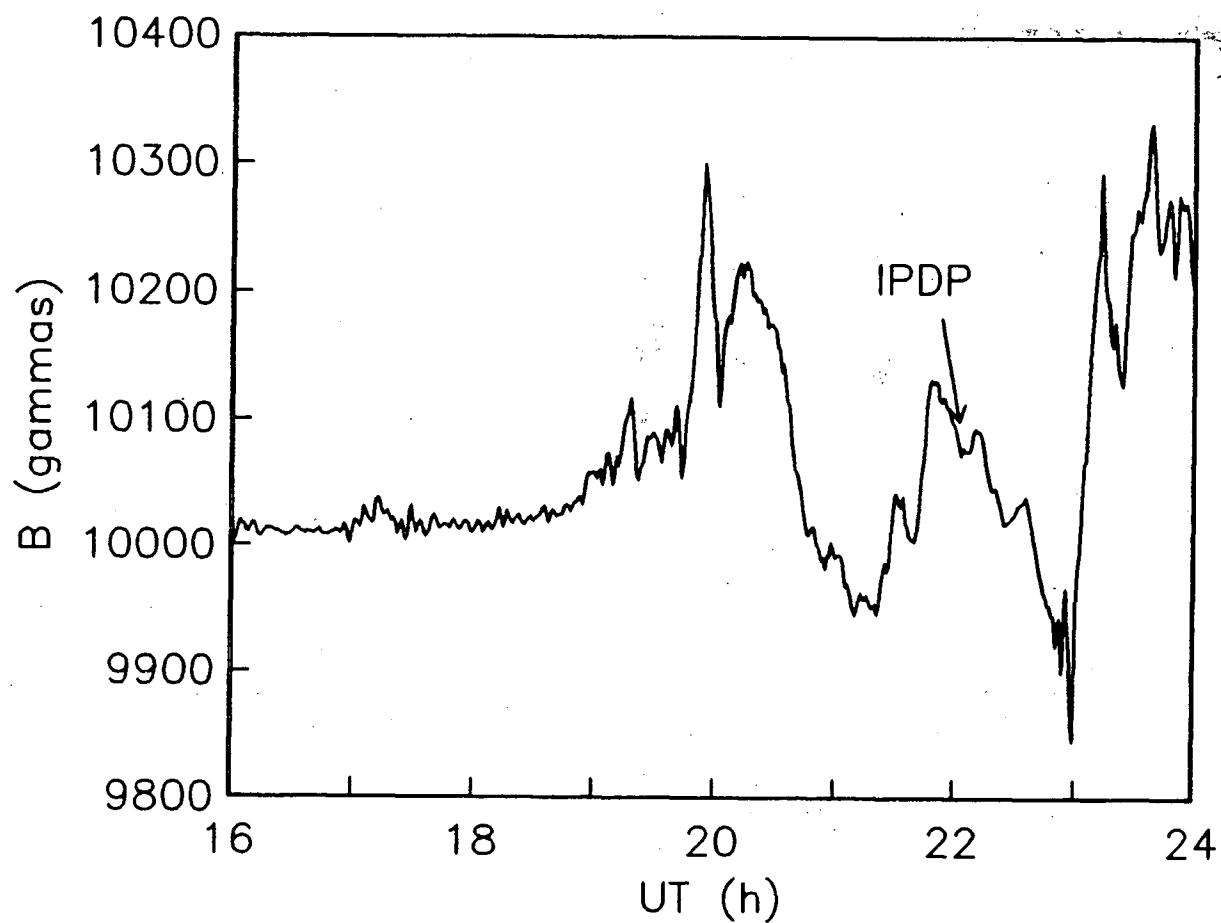


FIGURE 46.

X component magnetogram from Great Whale River, 1600 - 2400 UT, February 15, 1980. Note the onset of a second substorm during the IPDP event.

The Feb. 15 IPDP was generated within the L range of 4.1 to 4.8 (cf. sec. 5.1). In this situation, however, with the ring current at lower L (case II event, cf. fig. 40, 41), it is very difficult to estimate the magnetic field behaviour in the IPDP generation region, and therefore the effectiveness of the increasing field mechanism, without having further data on the ring current distribution. If the ring current is at very low L, it is possible that the magnetic field is increasing in the IPDP source region, though it is more probable (cf. fig. 41) that the magnetic field is decreasing or constant during this IPDP. In any case, the Feb. 15 IPDP is very short, with only a 16 minute interval studied in detail, and any magnetic field changes in this brief time are likely to be quite small, minimizing the effect of the increasing field mechanism.

Jan. 29 Event. The only event observed that qualified as a case III IPDP occurred on Jan. 29 (event no. 5, fig. 42). Both the Dst and geosynchronous satellite magnetograms were strongly depressed and had not yet begun their general recovery phases. Since they were each relatively stable (see fig. 47), the field in the IPDP generation region should have been similarly stable. Therefore the increasing field mechanism could not be responsible for this IPDP's frequency rise.

Feb. 24c Event. Three events, Jan. 27, Feb. 24a, and

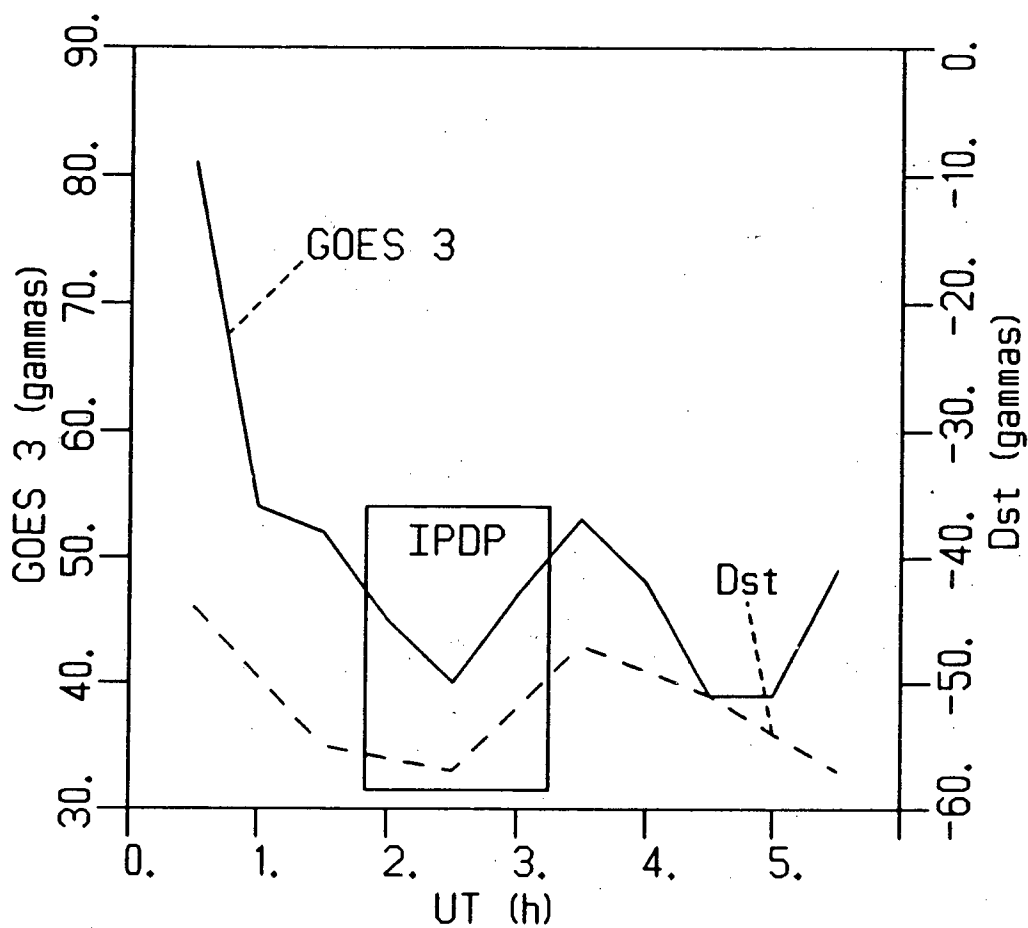


FIGURE 47.

Dst profile and GOES 3 magnetogram for the Jan. 29 IPDP, with the IPDP occurrence time indicated by the box. This is a case III event.

Feb. 24c (event no. 10, fig. 42), occurred when Dst is rising back towards zero. The third of the three IPDPs recorded on Feb. 24, event Feb. 24c, is shown in figure 48, along with its corresponding Dst indices and geosynchronous satellite magnetogram. The recovering Dst and geosynchronous magnetic field indicate a case IV event. The magnetic field should then also be increasing in the IPDP generation region. Therefore, for this event, the increasing field mechanism should contribute to the IPDP frequency shift.

Of the individual events discussed above, only the Feb. 24c event shows good indication that the increasing field mechanism contributes to its frequency rise. The question is how much of this event's frequency rise is attributable to this mechanism? In order to ascertain this, we must know the L shell of both the IPDP generation region and the ring current. The secondary source position could not be determined for this event (cf. section 5.1), however, the polarization spectrograms from PG ($L \approx 3.9$), first right-hand and then left-hand at the very end of the event, indicate that most of the event occurred to the north of the station ($L \approx 4+?$). Though the precise distribution of the ring current during this IPDP is unknown, models such as that of Kawasaki and Akasofu (1971), and measurements (Berko et al., 1975), show that this position is near the point of the greatest magnetic field depression of a typical ring

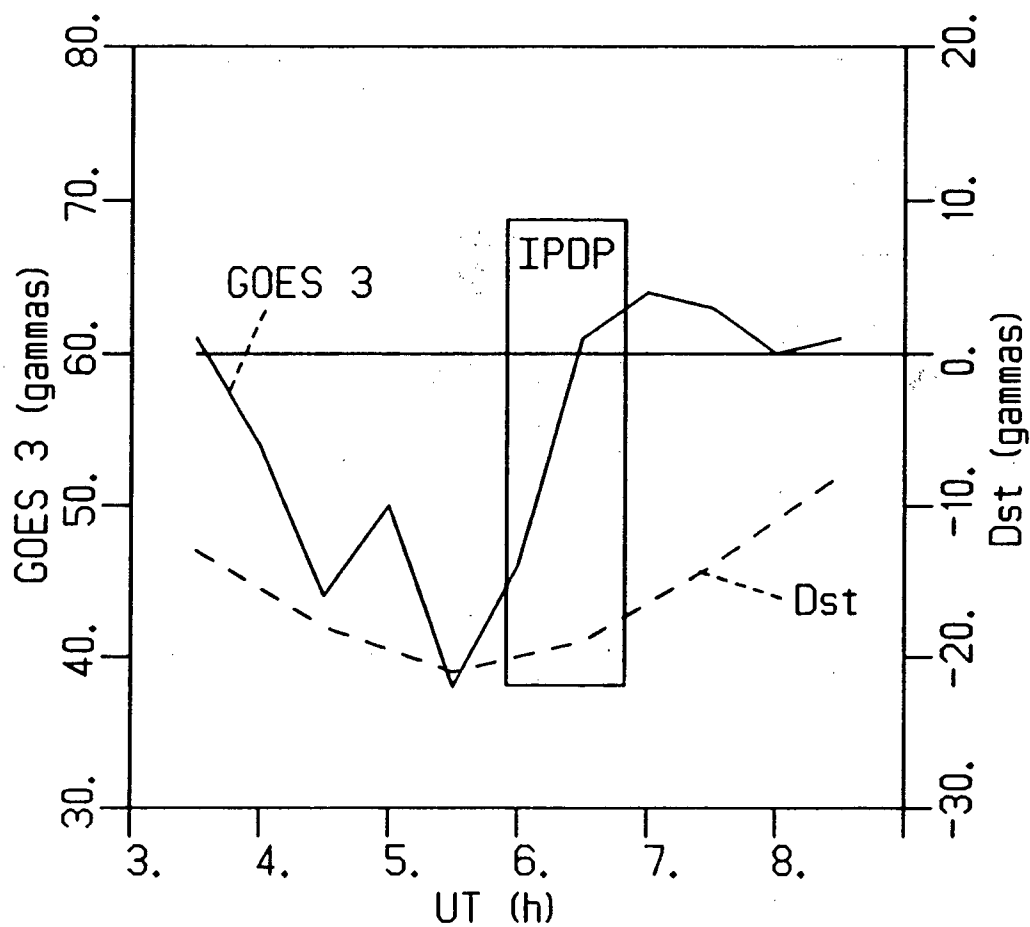


FIGURE 48.

Dst profile and GOES 3 magnetogram for the Feb. 24c IPDP, with the IPDP occurrence time indicated by the box. This is a case IV event.

current. This demonstrates that the field recovery in the IPDP generation region has the potential to be quite large. For this event, though, the small Dst depression indicates that the ring current may have been weaker and/or further out than normal. Note that Williams (1985) showed that the amount of Dst depression is related to ring current particle flux, and Lyons and Williams (1980) indicated that only large storms have significant ring current fluxes at lower L's. This situation indicates a correspondingly smaller field recovery in the IPDP generation region.

If a value for the field depression at $L \approx 4$ of -100γ were chosen for this event, then the field recovery in the IPDP generation region could be crudely estimated. Note that this field depression value is probably an overestimate for this weak Dst; Berko et al., (1975) observed values of -120γ near $L = 3\frac{1}{2}$ and -100γ near $L = 4$ for a Dst of -80γ . The magnetic field recovery during the IPDP can be gauged from the degree of recovery back towards their quiet time levels of the field at geosynchronous orbit, roughly -65γ to -45γ , or $\approx 30\%$, and of the Dst index, roughly -20γ to -16γ , or $\approx 20\%$. The field at $L \approx 4$ would most likely recover by a similar proportion during this time, assuming that the ring current changes only in strength and not in spatial distribution. Assuming Earth's magnetic field to be dipolar, its strength in quiet times at $L = 4$ should be:

$$B_0 = \frac{B}{L^3} \approx 484\gamma \quad (5.4).$$

Using the -100γ depression discussed above and a 30% recovery estimate, the magnetic field in the generation region should then rise from 384γ to 414γ during the IPDP. Using equation 4.6 from section 4.2.2, the frequency shift can then be estimated as:

$$\frac{f_f}{f_i} = \left[\frac{414\gamma}{384\gamma} \right]^{1.5} = 1.12 \quad (5.5).$$

For this event, however, the actual value is $f_f/f_i = 2.62$. Thus, in this crude estimate, the increasing field mechanism accounted for only $\approx 7\%$ of the total frequency rise for this IPDP. Though the field recovery figures used for this estimate are only very rough estimates, it is very unlikely that they could be altered enough to account for a large proportion of the frequency shift observed here. Increasing the initial depression to -150γ and the recovery factor to 50% would still only yield 22% of the observed frequency rise. Note that here the frequency rise referred to is a relative frequency rise from 1 (i.e. f_i/f_i) to f_f/f_i .

5.2.3. Ring Current and Inward Motion Mechanism

The calculations presented above for the increasing magnetic field effect on the Feb. 24c event assume that the IPDP source region is at constant L (cf. section 4.2.2). However, the pattern of polarization variations (see above) indicates that this is not the true situation. Therefore, in addition to the increasing field mechanism, it is also necessary to consider the effect of the depressed magnetic field environment in the IPDP source region on the inward motion frequency shift mechanism. The examination of the frequency effect of the inward motion mechanism under these conditions shows that there is another manner in which the ring current magnetic field can affect an IPDP's frequency rise independent of temporal changes in the ring current. If the ring current is in a state such that its magnetic field depresses the background magnetic field, this field depression will create a higher magnetic field strength ratio B_f/B_i than normal for a dipolar configuration. This then serves to increase the frequency shift effect due to the inward motion mechanism, as is illustrated below.

For the purpose of discussion only, we can assume reasonable choices for the amount of source inward movement, from, say, $L = 4.5$ to 3.9 during the Feb. 24c IPDP. In the absence of any ring current effects (field depressions), this motion would yield, from equation 4.5, $f_f/f_i = 1.90$.

Further, we can assume a field depression of -80γ at $L = 4.5$ and -100γ at $L = 3.9$ and a recovery factor of 25% during the IPDP. Again, these are reasonable choices made for the sake of discussion only. Using these values, the inward motion mechanism, in the depressed field environment (but with no field recovery), would produce a frequency rise as follows (from equation 4.6):

$$\frac{f_f}{f_i} = \left[\frac{(523-100)\gamma}{(340-80)\gamma} \right]^{1.5} = 2.08 \quad (5.6a)$$

where 523γ and 340γ are the dipolar field strengths (from equation 5.4) at $3.9L$ and $4.5L$, respectively, and 100γ and 80γ are the field depressions discussed above. This is an increase of 20% over the case with no ring current effects, demonstrating that, even with no temporal changes in the ring current field during an IPDP, it is still possible for the ring current to have an important effect on an IPDP's frequency rise, and it therefore cannot be ignored. Finally, the combined effect of the increasing magnetic field mechanism, using the 25% recovery factor, and the inward motion mechanism would yield the following frequency rise:

$$\frac{f_f}{f_i} = \left[\frac{(523-75)\gamma}{(340-80)\gamma} \right]^{1.5} = 2.26 \quad (5.6b).$$

This is only a 17% increase in the frequency rise over the inward motion only case discussed above (equation 5.6a). While some of the numbers used here represent assumptions only and may bear little relation to the actual parameters concerning this IPDP, parameters for which we have insufficient information to properly determine, they cannot be reasonably altered to produce a significantly larger increasing field mechanism contribution. Therefore, whether the IPDP generation region is assumed to be stationary or not, the increasing field mechanism makes only a relatively minor contribution to the frequency rise of the Feb. 24c IPDP.

In section 5.1 it was shown that, for both the Feb. 14 and Feb. 15 IPDPs, the inward motion mechanism was insufficient to account for the observed frequency rise of the IPDPs. Here, it has also been demonstrated that the increasing field mechanism makes only a minor, if any, contribution to the frequency shifts of these events (cf. section 5.2.2). However, the possible effects of the ring current created magnetic field depression on the inward motion mechanism's frequency shift contribution to these

events must still be considered.

For the Feb. 14 event this ring current effect is likely to be small since the ring current is probably not yet well developed in the source region L shells. The current is relatively weak in any case, as is demonstrated by the fact that the maximum field depressions observed during the entire magnetospheric storm period are only -50γ at $L = 6.6$ and only -35γ at $L = 1$ (Dst). Calculations similar to that of equation 5.6a show that a uniform field depression of -115γ would be necessary in order to enhance the inward motion produced frequency shift sufficiently to account for the entire frequency rise of this event. Such depressions are very unlikely to be present in such a case I event generated at low L (cf. section 5.2.1). Even with a constant field depression of -50γ in the generation region, probably still much larger than would be realistic, the inward motion mechanism could account for only $\approx 77\%$ of the IPDP's overall frequency rise, as opposed to $\approx 66\%$ with no ring current induced magnetic field depression.

It has already been noted that during the Feb. 15 event the magnetic field strength is unlikely to change much at constant L. It will, however, be strongly depressed in the IPDP source region, as indicated by the strong Dst depression (cf. fig. 45) and the form of typical ring current field profiles (cf. fig. 40, also Kawasaki and

Akasofu, 1971; Berko et al., 1975). It has been found that a source region field depression of -105γ would be necessary to enhance the inward motion produced frequency rise so that it would best match the observed rise of this IPDP. A field depression of this magnitude is quite possible for this event (see above), though it cannot be directly confirmed by observation. However, the depression should be greater than the Dst depression of $\approx -55\gamma$. Using this -55γ value as a lower limit on the source region field depression, the enhanced inward motion mechanism frequency shift can account for $\geq 75\%$ of the IPDP's overall frequency rise, compared to $\approx 60\%$ with no ring current field influence. Figure 49 compares the real frequency rise to those enhanced inward motion created frequency shifts calculated for source region magnetic field depressions of -105γ and -55γ .

5.2.4. Discussion of Ring Current Effects on IPDPs

A much larger number of IPDPs must be studied in order to gain a clearer picture of the proportion of events to which the increasing field mechanism is important. Here, based on the IPDP - ring current classification scheme discussed in section 5.2.1, this mechanism may have contributed to the frequency rise of between three, the class IV events, and six, the class II and IV events, of the ten IPDPs studied, with the contribution being either small

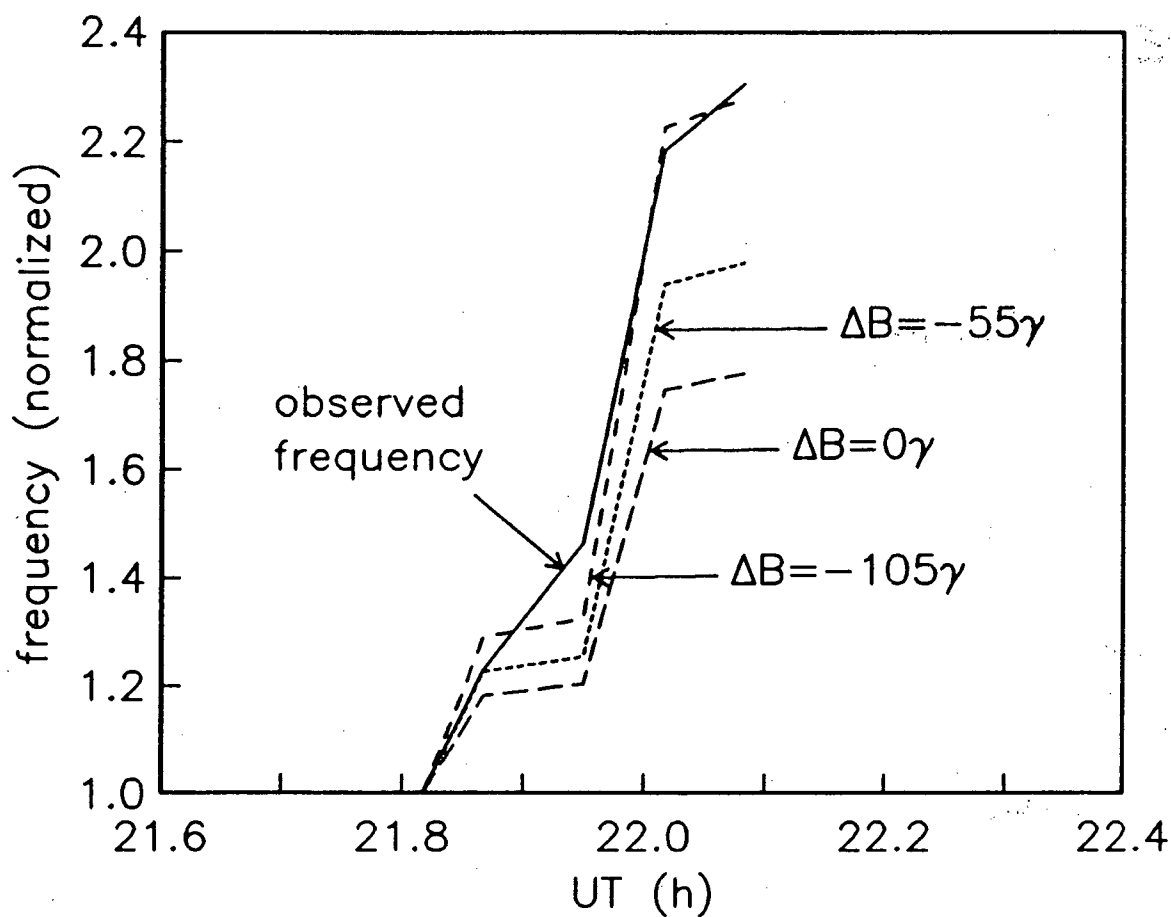


FIGURE 49.

February 15 IPDP: observed frequency rise and enhanced inward motion rises with magnetic field depressions (ΔB) of 0γ (no ring current), -55γ , and -105γ . This figure also clearly demonstrates how even static ring current induced field depressions can affect IPDP frequency shifts.

(Feb. 24c event) or unknown. The small contribution of the increasing field mechanism to the frequency shift of the Feb. 24c event is at least partially due to its low L and weak ring current, however.

It is clear, though, that the increasing background magnetic field mechanism is not required in order to produce IPDP frequency shifts. For the two IPDPs being studied in detail, the Feb. 14 and Feb. 15 events, the increasing field mechanism has been shown to have only a very minor influence, if any at all. For these events, the magnitude of the ring current induced field is more important than its changes. Though this effect is relatively minor in the Feb. 14 IPDP, raising the inward motion mechanism's contribution to $<77\%$ from $\approx 66\%$, it may be an important factor in explaining the Feb. 15 event, allowing the inward motion mechanism to account for $\geq 75\%$, and possibly up to 100%, of the frequency rise.

With respect to these two IPDPs, however, the conclusion is that we must look still further than the inward motion and increasing field mechanisms in order to fully understand the entire frequency shifts of these events.

5.3. AZIMUTHAL DRIFT EFFECTS ON IPDP FREQUENCY EVOLUTION

The third of the three IPDP frequency shift mechanisms considered in this thesis is the azimuthal drift effect (cf. section 4.2.3). From section 5.2, it is evident that contributions from this mechanism are required by at least one, and possibly both, of the IPDPs studied in order to fully account for their frequency shifts. This section will then examine the effects of the azimuthal drift mechanism on the Feb. 14 and Feb. 15 IPDPs.

Analysis of the azimuthal drift mechanism's effect requires a knowledge of the evolution of the energies of the protons involved in the ion-cyclotron instability in the IPDP magnetospheric source region above a ground station's meridian. Equation 4.3 (section 4.1) shows that in order to determine the energy (W) of the interacting protons, both L and the proton drift velocity (v_d) must be known. Though the L values were determined in section 5.1, v_d is unknown, and cannot be calculated without the time and position of the injection boundary formation being known. The time of formation can be estimated from auroral-zone ground station magnetograms (see below), but the boundary shape remains unknown. Note that the statistical relation describing injection boundary shape presented in section 4.1 (equation 4.1) cannot, in the form given, be fit satisfactorily into the description of the IPDP events considered here. This is

especially true in the case of the Feb. 14 event, since the boundary shape produced would not reach to low enough L to form the event as observed (for example, see fig. 55 (bottom)). Consequently, a method by which the boundary position and therefore the proton energy can be estimated for each IPDP is required. Such a method is described below. Since it was shown in section 5.2 that a ring current magnetic field depression in the IPDP generation region can have an important influence on an IPDP's frequency rise, this method allows for the effect of such a depression and yields an estimate of its magnitude.

In order to estimate the injection boundary position from IPDP data, the position of the source region (L,GMLT) and the westward drift arc of the protons between the injection boundary and the plasmapause ($\Delta L T$) must be known. The source region GMLT is equivalent to the GMLT of the observing ground station, and L is found as in section 5.1. The relative drift arcs $\Delta L T / \Delta L T_i$ can be found from a modified form of equation 4.8 (cf. section 4.3) as follows:

$$\frac{\Delta L T}{\Delta L T_i} = \left[\frac{t_d}{t_{di}} \right] \left[\frac{f_i}{f} \right]_{obs}^2 \left[\frac{L_i}{L} \right]^8 \quad (5.7a)$$

where f_{obs} represents the observed IPDP frequency and L is as found in section 5.1. This equation yields the $\Delta L T / \Delta L T_i$

necessary for the frequency rise predictions of the combined azimuthal drift and inward motion mechanisms to match the observed frequency shift of an IPDP. Note that equation 5.7a assumes a dipolar magnetic field configuration.

The proton drift times (t_d) required by equation 5.7a are estimated from auroral-zone station magnetograms and the injection expansion times of Arnoldy and Moore (1983) (cf. section 4.1). The substorm's onset time is determined from the magnetograms of the auroral-zone station which first sees a large negative bay in its X-component, a sign of the start of a new substorm, preceding the IPDP event, and is also confirmed by the occurrence of Pi 2 pulsations. The time of the beginning of the bay at this first station gives the onset of the substorm, and therefore the beginning of injection boundary formation (Arnoldy and Moore, 1983), near the station's meridian. This procedure then also provides a tentative estimate of the meridian of the initial injection at substorm onset. Since the boundary takes 10 to 15 minutes after substorm onset to complete its expansion to the west (cf. section 4.1), proton drift from the boundary should begin within 15 minutes after substorm onset. The actual time of drift onset for an IPDP's protons depends on how far to the west of the meridian of initial injection the section of the injection boundary forms from which these protons drift. The conclusion of the westward drift phase of the

protons concerned is marked by their involvement in the ion-cyclotron instability at the plasmopause generating the IPDP. The drift times to be used in equation 5.7a can then be found from the difference between the estimated injection time and the measured generation time.

Equation 5.7a can actually be replaced by a more versatile form by replacing L with the magnetic field strength (B) in the inward motion factor only. Thus, equation 5.7a then becomes:

$$\frac{\Delta LT}{\Delta LT_i} = \left[\frac{t_d}{t_{di}} \cdot \frac{L}{L_i} \right] \left[\frac{f_i}{f} \right]_{obs}^2 \left[\frac{B}{B_i} \right]^3 \quad (5.7b)$$

where B can now be calculated from L as

$$B = (B_{eq}/L^3) + \Delta B.$$

The replacement of L by B in the inward motion factor and the inclusion of the ΔB term in calculating B now permits the effect of magnetic field depressions, which alter the purely dipole field profile given by B_{eq}/L^3 by an assumed constant amount ΔB , on the inward motion mechanism to be taken into account. The simplifying assumption of constant ΔB in the IPDP generation region during the event is made here. It must also be noted that this form of equation 5.7 assumes that the field depression affects only the inward

motion mechanism, and does not influence the azimuthal drift process (i.e. $\Delta B = 0$ during the drift phase). At the beginning of the drift phase, ΔB can generally be assumed small since the ring current is often not well developed at this time. However, as the ring current develops (cf. section 5.2), the ΔB later in the drift phase may become larger. Determining drift velocities for this type of situation is quite difficult, especially since the information needed to estimate the ΔB 's affecting the proton drift is lacking. Therefore, the process has been idealized by setting $\Delta B = 0$ during the drift phase, then allowing ΔB to be non-zero (but uniform) during IPDP generation at the plasmopause. If non-zero ΔB is present during the drift phase, a reduced magnetic field strength (B) will increase drift velocities somewhat (cf. equation 4.2a), though this could be partially offset by an increased field line radius of curvature near the equator (cf. equation 4.2b). A very large ΔB would have to exist over most of the westward drift range in order to significantly affect the energies of the protons involved in IPDP generation, in which case the IPDP proton energies should be somewhat lower.

Equation 5.7b now produces the necessary $\Delta L_T / \Delta L_T$, for the combined frequency shifts from azimuthal drift and ΔB -adjusted inward motion mechanisms to match the observed frequency rise. However, since ΔB is not known with any

precision, a number of calculations must be carried out for a range of ΔB values, giving many possible $\Delta LT_i / \Delta LT_i$ sets for a single IPDP.

The next step required is the selection of the energy of the initial protons involved in the IPDP generation (W_i), allowing the calculation of ΔLT_i ($\Delta LT_i = t_{di} W_i L_i$). Here again, the actual initial energy is unknown, so we must repeat the calculation over a range of W_i values. Once ΔLT_i is known, all the ΔLT s can be determined from the ratios found from equation 5.7b above. These ΔLT s plus the source region GMLTs then yield the injection boundary local times at the L values of the IPDP source region.

The net result of all these calculations is that, for each pair of ($W_i, \Delta B$) values selected, we have a series of (L, LT) points which define a segment of an injection boundary which gives, for that W_i and ΔB , an exact match of the combined azimuthal drift and ΔB -adjusted inward motion predicted frequencies, henceforth termed the "combined mechanisms" predicted frequencies, to the observed IPDP frequencies. It must now be determined which of these ($W_i, \Delta B$) pairs and corresponding injection boundary segments best represents the actual magnetospheric situation involving the IPDP event in order to estimate the proper injection boundary position.

The boundary segments calculated by the above method

cover limited spans in L and LT compared to an entire injection boundary. Consider: if these prospective boundaries are extended to cover the full LT range typical of an injection boundary, do they resemble the descriptions provided by Mauk and Meng (1983) (cf. sec. 4.1)? This can be tested by fitting the boundary points to the expression for a single, duskward spiral injection boundary (Mauk and Meng, 1983):

$$LT = \frac{\kappa_1}{L} + \kappa_2 \quad (5.8)$$

where κ_1 and κ_2 are constants to be determined by the curve-fitting process. Note that this relation is essentially the same as that of equation 4.1, except that the constants remain to be determined.

It is now possible to plot a full injection boundary for each $(W_i, \Delta B)$ pair for which boundary points were determined. The new curve-fit injection boundaries allow us to recalculate the predicted frequency rise using these new boundary shapes from each $(W_i, \Delta B)$ pair, and to present some criteria for selecting the $(W_i, \Delta B)$ pair which best characterizes each IPDP event. These criteria, along with a few others, are:

- Boundary shape. Does the injection boundary, in terms of

the values of κ_1 and κ_2 in equation 5.8, approximate the descriptions derived from observation, and does its eastward end correspond to the injection onset GMLT observed by auroral-zone stations?

- Frequency match. How well do the combined mechanisms predictions, using the new curve-fit boundary shape, match the observed frequency rise?
- Boundary match. How well does the new injection boundary fit the original boundary points, that is, what is the error between the original points and the new boundary as calculated in the curve-fitting process? Note that this is separate from the boundary shape criterion since a good fit of the data to equation 5.8 does not necessarily imply that the shape of the boundary produced is reasonable.
- ΔB range. Does the ΔB for this boundary fall within a reasonable range? This range is determined by considering typical ring current ΔB profiles along with the depressions of the Dst index and the geosynchronous satellite magnetograms associated with an IPDP, and can be different for each IPDP.
- W range. Do the proton energies for the whole event lie within the broad range of ≈ 10 to ≈ 300 keV within which IPDPs are thought to occur?

These selection criteria can now be applied to the

results of the injection boundary calculations for each $(W_i, \Delta B)$ pair in order to choose the best pair. The first series of calculations performed for this purpose used a large $W_i, \Delta B$ grid spacing, with W_i varying by 20-30 keV and ΔB by 10-20 γ , in order to isolate the range of interest for each of the parameters. Then progressively finer grids, down to a grid spacing of 2keV by 2γ , are used until the best pair is obtained. The selection criteria discussed above are used to determine the best $(W_i, \Delta B)$ pair as follows. First, they are employed in a general manner to determine where to make calculations over finer grids, then in a more detailed manner on the results of the calculations from the finest grid spacing in order to select the best $(W_i, \Delta B)$ pair. This detailed evaluation of the selection criteria is performed in a quantitative manner using the boundary shape, frequency match, and boundary match criteria only. For the ΔB and W range criteria, the ΔB and W ranges for each IPDP are simply judged either acceptable or unacceptable, with the unacceptable pairs being rejected. For the quantitative evaluation, each of the three criteria for a particular $(W_i, \Delta B)$ pair are rated relative to that criteria from the other pair calculations. For example, the $(W_i, \Delta B)$ pair with the best frequency match would be assigned ten rating points, while that with the worst match, considering only the pairs for which detailed evaluations are being done,

would be given zero points. The other $(W_i, \Delta B)$ pairs considered would be assigned intermediate values within this range depending on the quality of their frequency matches. The same scheme is applied to the other two criteria. Finally, the rating points from each criterion for each $(W_i, \Delta B)$ pair are summed, and that pair with the largest sum is deemed to be the pair best describing the IPDP event's situation in that it has the best combination of injection boundary and frequency match. Note that the boundary shape and frequency match criteria are given double weight in the summing process.

Figure 50 contains a flow chart which summarizes the entire process, as described above, for determining the effects the azimuthal drift and ΔB -adjusted inward motion mechanisms have on an IPDP's frequency shift. This process represents an intuitive, practical approach to the problem of understanding IPDP frequency shifts, and, though still quite simple, is the best available and does give reasonable frequency shift estimates.

5.3.1. Feb. 14 Event

The above boundary selection process can now be applied to the two events studied in detail in sections 5.1 and 5.2. First, we will look at the Feb. 14 IPDP.

Before the boundary calculation can be made, however,

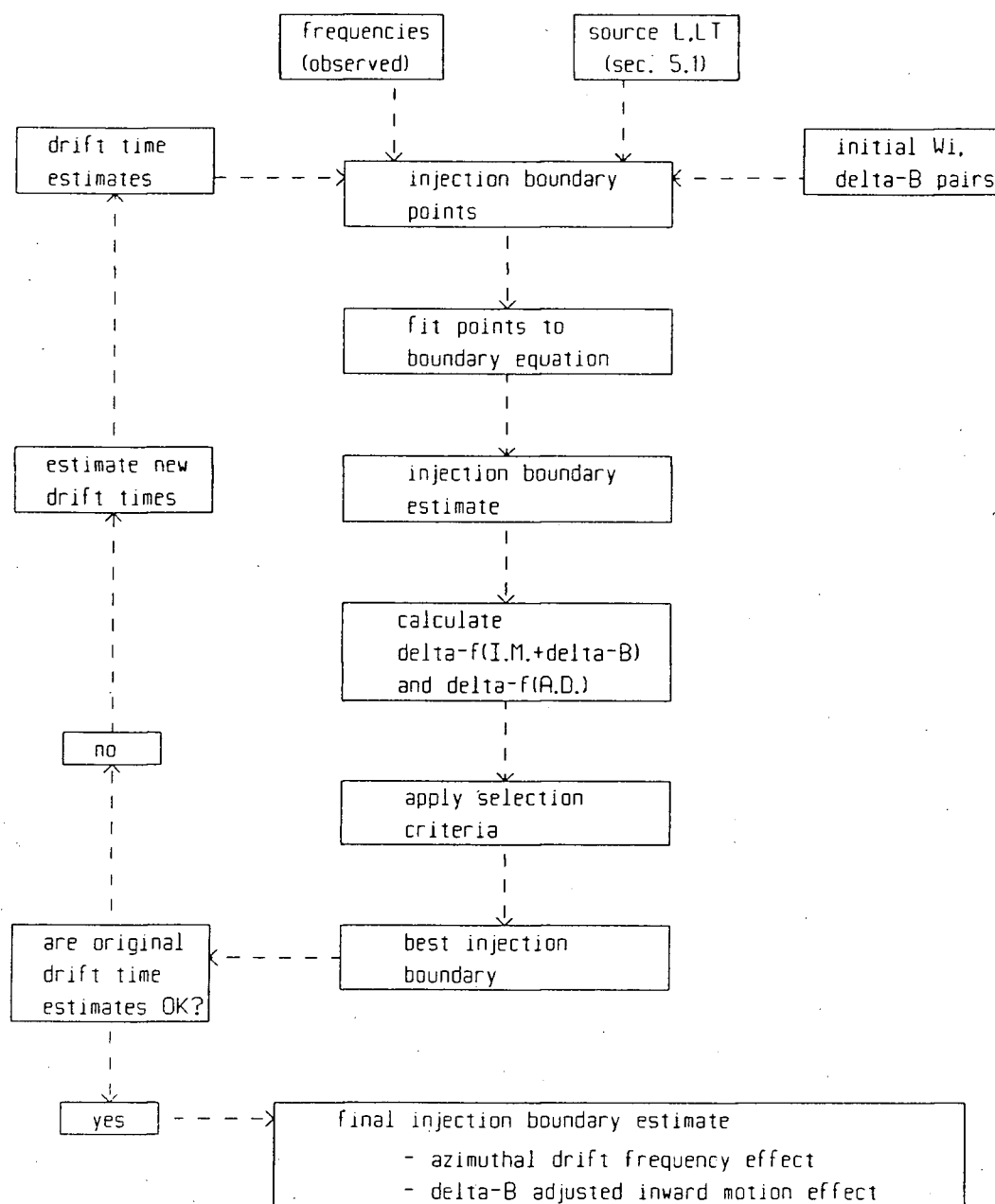


FIGURE 50.

Flow chart for the estimation of injection boundary position and the azimuthal drift and ΔB -adjusted inward motion frequency shift effects (see text for detailed description).

the drift times (t_d) must be estimated. For this event, the Great Whale River (GWR) magnetogram showed the substorm onset earlier than stations to the east or west, and therefore indicates that this substorm, and thus the plasma injection, start near 0807UT (see fig. 51), at 27.35 GMLT. The onset time is also confirmed by Pi 2 observations. For this IPDP then, the proton drift must start well after midnight, since the IPDP occurs after midnight. The drift is estimated to begin approximately 1 ± 1 minutes after the injection starts. This estimate is based on an injection boundary formation time of 12 minutes, starting from 27.35 GMLT and then expanding to the west through 10 hours of GMLT, with the IPDP drift onset time estimate being made by interpolation within this interval using a formation rate which is ten times faster at the eastern end than at the western end (cf. section 4.1). The uncertainty in drift start times is quite small when compared to the actual drift times of 27 to 92 minutes. The ΔB for this event is likely to be fairly small (cf. section 5.2), and therefore boundary calculations will be carried out over the range $0 \leq \Delta B \leq -60\gamma$. The W_i range used for these calculations is $10 \leq W_i \leq 140$ keV.

With these parameters, the best-fit injection boundary for the Feb. 14 IPDP was that calculated from the starting point of $W_i = 14\text{keV}$ and $\Delta B = -14\gamma$. This $(W_i, \Delta B)$ pair

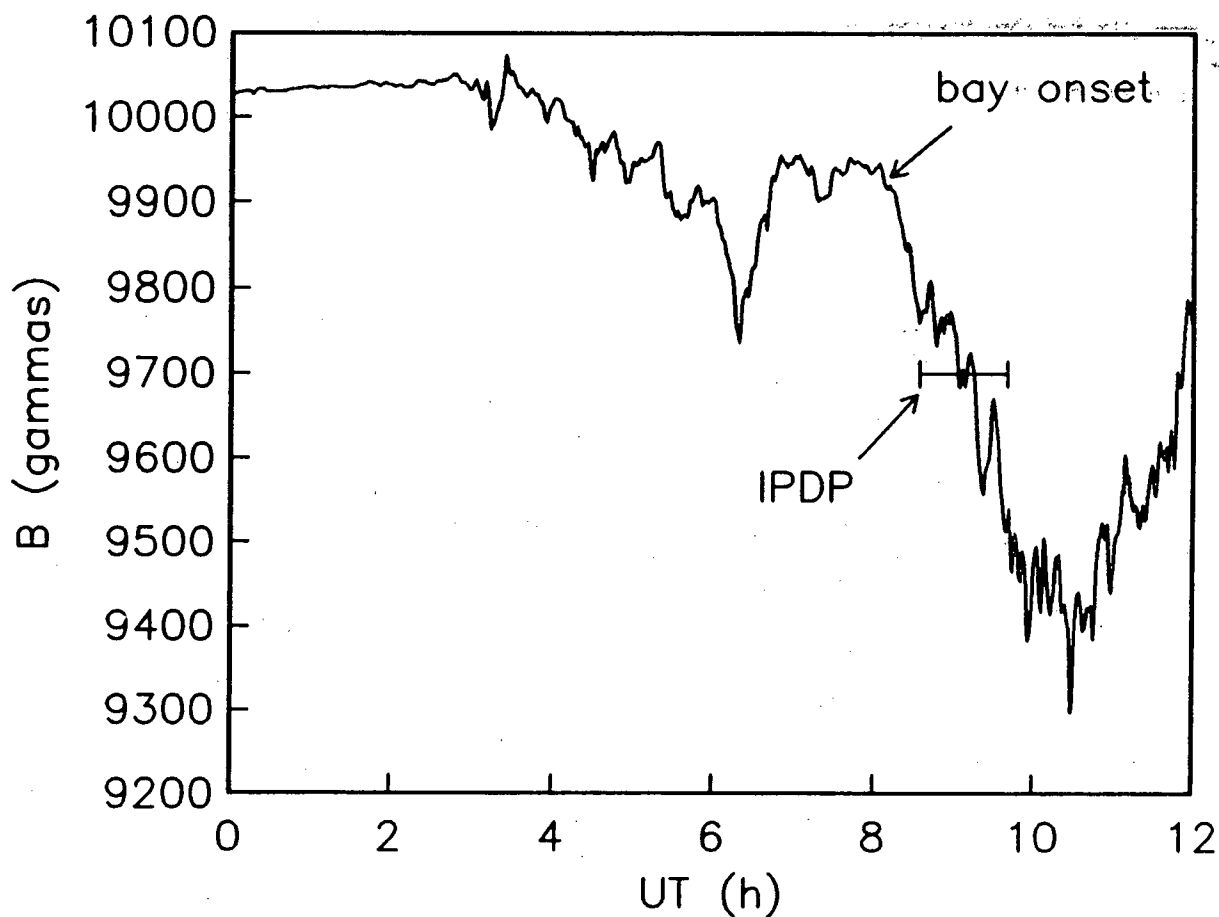


FIGURE 51.

X-component magnetogram from Great Whale River, 0000-1200UT, Feb. 14, 1980. Note the large negative bay beginning at 0807UT, shortly before the IPDP event starts.

produced the best combination of boundary shape and frequency match compared to the results for these criterion for the other ($W_i, \Delta B$) pair calculations. The W and ΔB range criteria are also satisfied, with the W values being within the range normally associated with IPDPs and the ΔB value being quite acceptable when compared to the Dst index and geosynchronous satellite magnetogram for Feb. 14 (cf. section 5.2). In addition, the boundary match (LT error between data points and curve: 0.163h) is also acceptable, falling approximately in the middle of the range of boundary curve-fit errors of 0.161 to 0.166 h produced by boundaries for which ratings sums were calculated. This injection boundary and the calculated plasmopause points associated with the IPDP are shown in figure 52.

Figure 53 illustrates the change in proton energy during the IPDP. This energy profile is found using the new boundary, as shown in figure 52, thus $W_i = 16\text{keV}$, not 14keV , due to the difference between the new curve-fit boundary and the original boundary points. Note that W_i , and not t_{di} , is altered to accomodate the new curve-fit boundary shape since t_{di} as estimated from the boundary formation time cannot change. The observed frequency rise and that predicted by the proton energy change (or azimuthal drift) effect, both normalized, are also shown in figure 53. The frequency shifts due to the hot proton energy changes are calculated

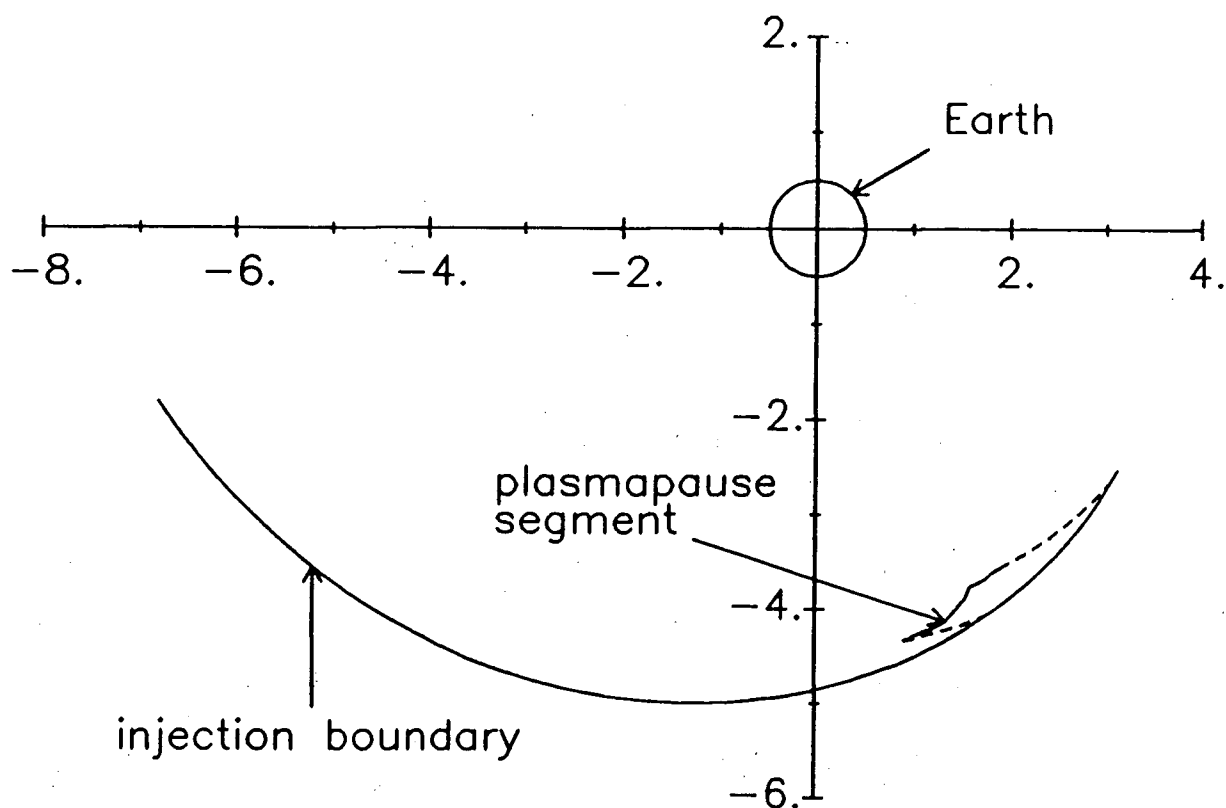


FIGURE 52.

Model plot for Feb. 14 event, showing the injection boundary selected and the plasmopause segment defined by the IPDP generation region (L,GMLT) coordinates. The region through which the protons drifted for this IPDP (as observed on the Saskatchewan line) is enclosed by the dashed lines. The sun is towards the top of the page, and the distance labels on the axes are in L (Earth radii). Note that the source region GMLTs of $\approx 0100-0200$ are quite late compared to typical IPDPs.

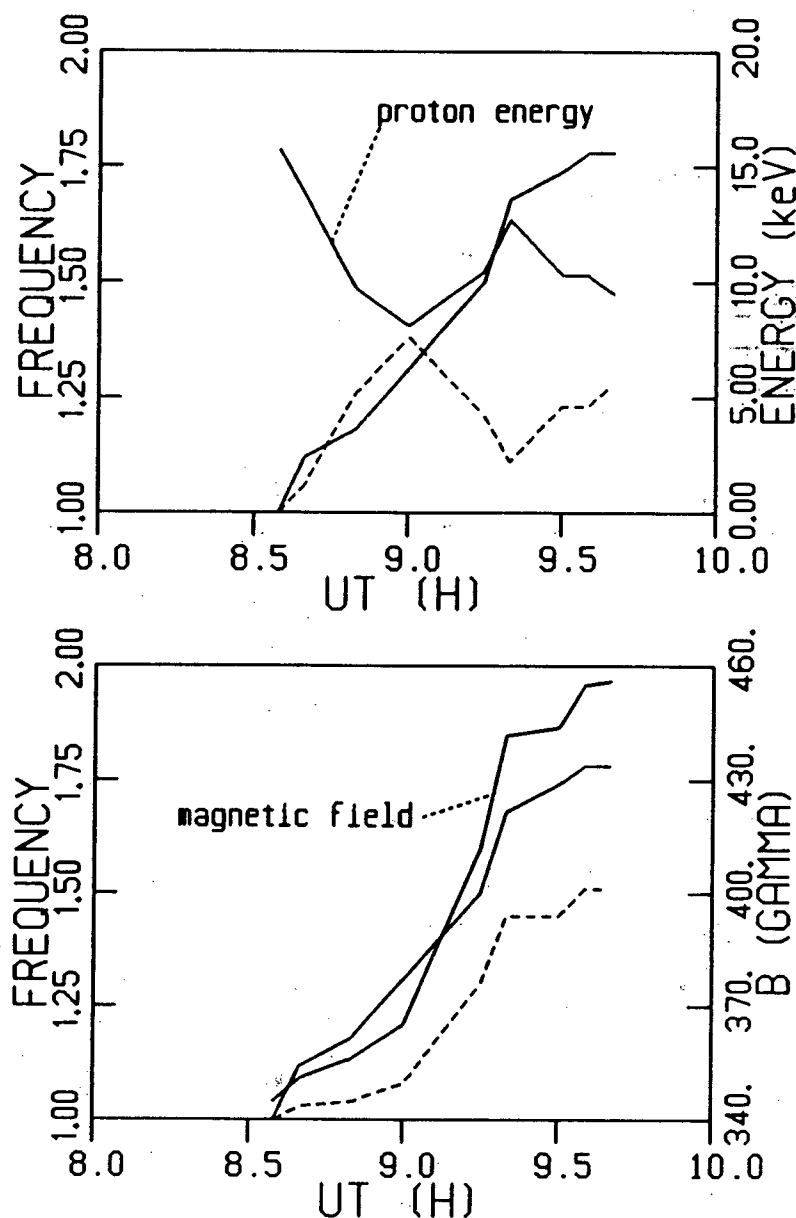


FIGURE 53.

Top: proton energy profile plus the observed (solid line) and azimuthal drift mechanism predicted (dashed line) frequency profiles (normalized) for the Feb. 14 IPDP. Bottom: magnetic field strength profile plus the observed (solid line) and ΔB -adjusted inward motion mechanism predicted (dashed line) frequency profiles for the Feb. 14 IPDP.

from equation 4.7.

It should be pointed out here that the frequency effects of changing proton energies and inward source motion cannot really be isolated in this manner, since inward motion occurs simultaneously with the proton energy changes. The calculation using equation 4.7 for the energy change frequency shift is then an hypothetical case only in which, for the purpose of discussion, inward motion is assumed to be zero. In this discussion we have also used the terms "azimuthal drift effect" and "hot proton energy change effect" interchangeably. Though the azimuthal drift effect creates hot proton energy changes (cf. section 4.2), it is not the only effect causing these changes since IPDP generation, as seen from a ground station, involves protons drifting on different L-shells at different times. The proton streams on these different L-shells have different velocities and different drift start and end times, and can therefore have different proton energies at any one time, demonstrating that crossing L-shells in to these different streams can also cause proton energy changes. Thus, henceforth we will use terms such as "hot proton energy change effect" instead of "azimuthal drift effect" when discussing energy change frequency shifts.

During the Feb. 14 IPDP, as shown in figure 53, the proton energy drops rapidly and the hot proton energy change

effect frequency shift increases significantly at the beginning of the event, and then they have little net change over the final $\frac{2}{3}$ of the IPDP. This reduction, and temporary reversal, of the rate of change of these profiles could be attributed to rapid inward motion of the plasmopause during the central part of the IPDP, requiring the protons to be more energetic in order to reach it within the drift time available.

Figure 53 also shows the magnetic field profile along with its predicted frequency rise and the observed rise for the Feb. 14 IPDP. The frequency rise due to the increasing magnetic field is determined by equation 4.6. The frequency rise predicted here is very similar to that shown in figure 32 for inward motion without a ΔB adjustment, though the increase is slightly larger in this case; 68% of the observed end frequency, up from 66%. The combined effects of the increasing B and generally decreasing W can be calculated from a rearranged version of equation 5.7b:

$$\frac{f}{f_i} = \left[\frac{\Delta L T_i}{\Delta L T} \cdot \frac{t_d}{t_{di}} \cdot \frac{L}{L_i} \right]^{0.5} \left[\frac{B}{B_i} \right]^{1.5} \quad (5.9).$$

This combined frequency rise is compared to the observed frequency in figure 54. The relatively good match between the two is, of course, a result of the $(W_i, \Delta B)$ pair

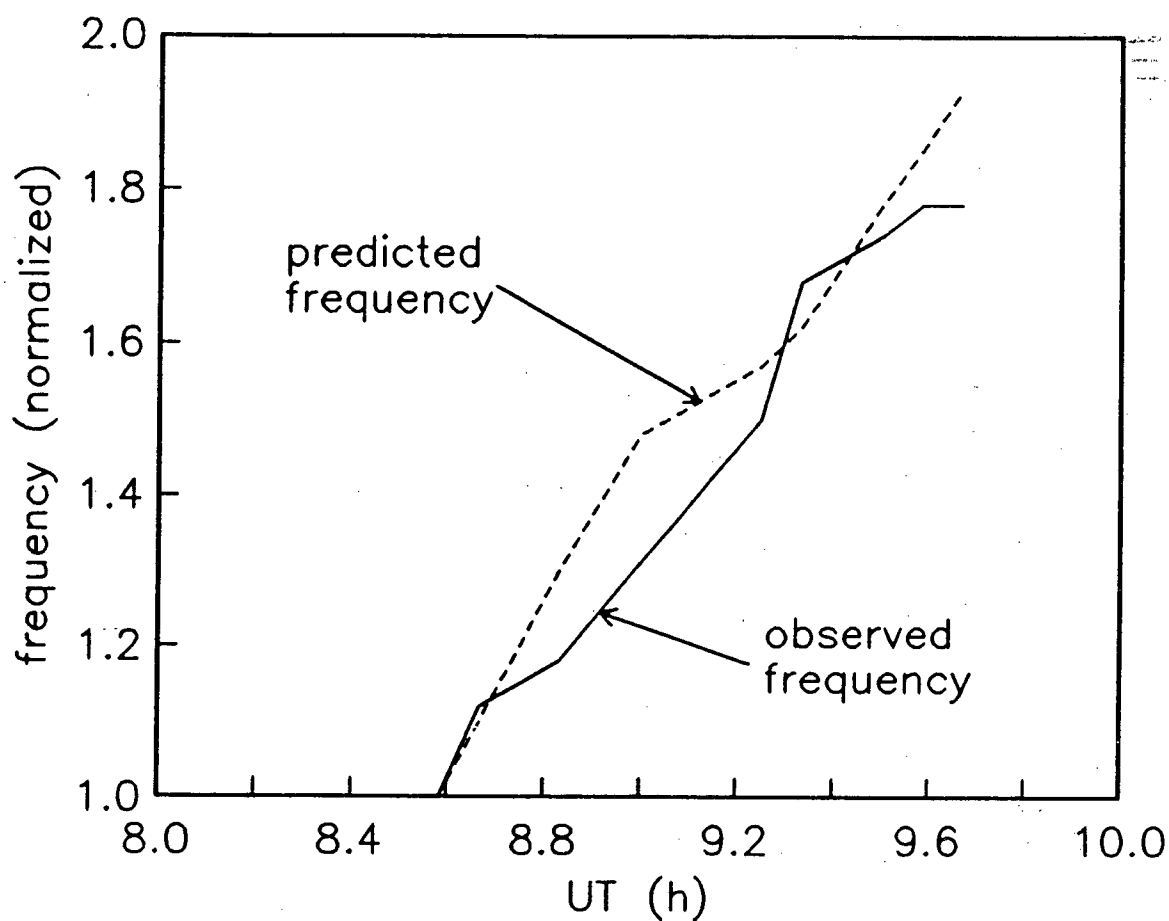


FIGURE 54.

The frequency rises as observed and as calculated for the combined azimuthal drift - ΔB -adjusted inward motion mechanisms for the Feb. 14 event, showing the good match between the two curves.

originally chosen.

In contrast to the best pair results discussed above, figure 55 shows the results of calculations using two different $(W_i, \Delta B)$ pairs. The top portion of this figure compares the predicted frequency rise found for $W_i = 10\text{keV}$ and $\Delta B = -10\gamma$ to the observed rise for the Feb. 14 IPDP. It is apparent that this frequency match is much poorer than for the best case pair, with the predicted frequency rise being generally much higher than the observations. The lower portion of figure 55 shows the injection boundary as calculated from $W_i = 22\text{KeV}$ and $\Delta B = -30\gamma$. The boundary shape produced by this pair could not actually yield the Feb. 14 IPDP when and where it was observed since it does not reach low enough L at its eastward end (cf. fig. 55) as determined by the meridian of substorm onset. Problems such as these two illustrated above appear consistently for boundary calculations using $(W_i, \Delta B)$ pair values which are not close to those producing the best case. The ratings sums for these calculations, respectively 18 and 20, are understandably quite poor when compared to the best case sum of 34, though on the other hand, they certainly do not represent the worst cases either.

For the Feb. 14 IPDP, we can now conclude that, overall, the dominant role in creating the event's frequency shift is taken by the inward motion mechanism, which is

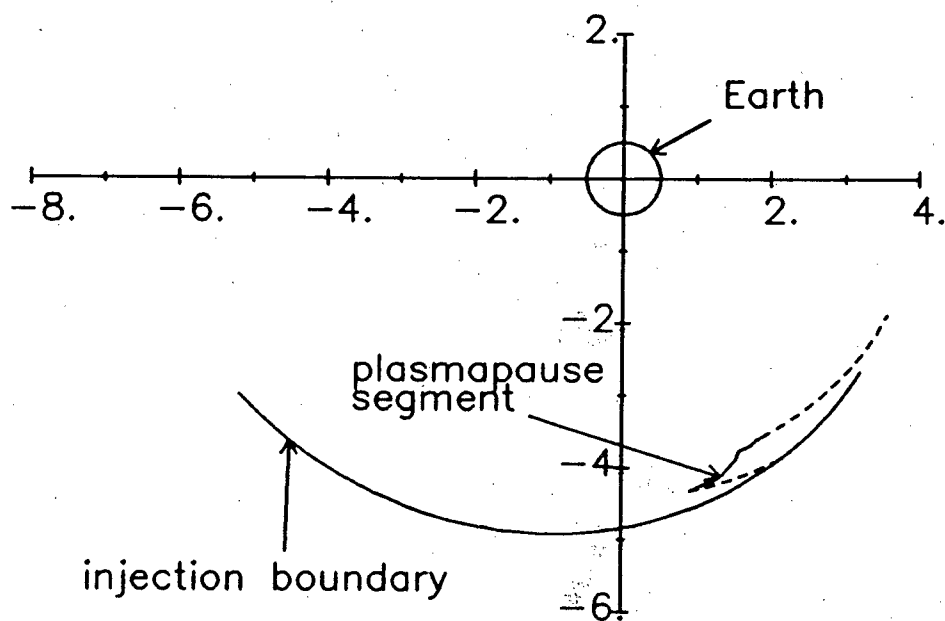
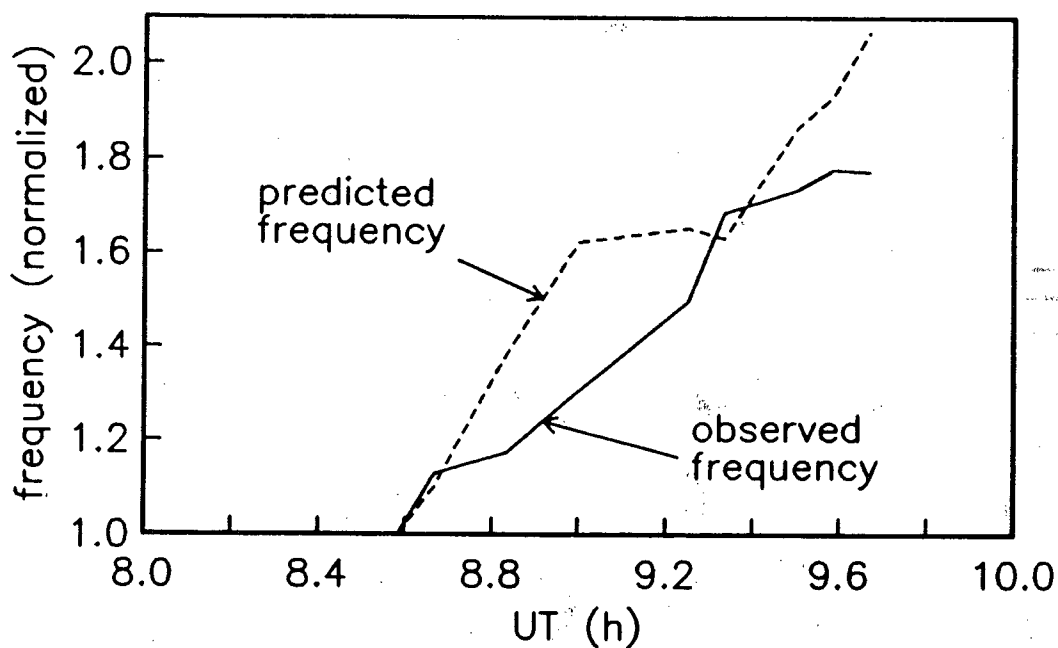


FIGURE 55.

Top: Predicted frequency rise for $W_i = 10\text{keV}$ and $\Delta B = -10\gamma$ for the Feb. 14 event. Bottom: Injection boundary for $W_i = 22\text{keV}$ and $\Delta B = -30\gamma$. These parameters produce results much worse than those for the best case.

further enhanced somewhat by a depressed (-14γ) magnetic field in the IPDP generation region. This cannot account for the entire frequency rise, though, and a secondary role is played by hot proton energy changes. However, for the first $\frac{1}{3}$ of the event, this hot proton energy change effect is actually the dominant factor in producing the frequency shift, with the inward motion mechanism occupying a secondary role. Recall that it was shown in section 5.2 that the increasing field mechanism is not important here.

5.3.2. Feb. 15 Event

As with the Feb. 14 event, before the injection boundary position is calculated the proton drift times must be estimated. For this event, the substorm and injection onset occurred east of the auroral-zone stations available to us. However, the substorm effects were observed to begin in the afternoon sector at GWR (GMLT = 1533) at 2036UT (fig. 56). From the onset of Pi 2 pulsations, though, the actual substorm onset occurred near 2028UT. The westward drift of the protons involved in the IPDP would then have started sometime after this time. In addition, the drift of the IPDP protons started from a boundary segment at lower L-shells, and therefore later GMLTs, than GWR, likely from the dusk sector. Based on a boundary formation time of approximately 8 minutes to the meridian of GWR and using a similar

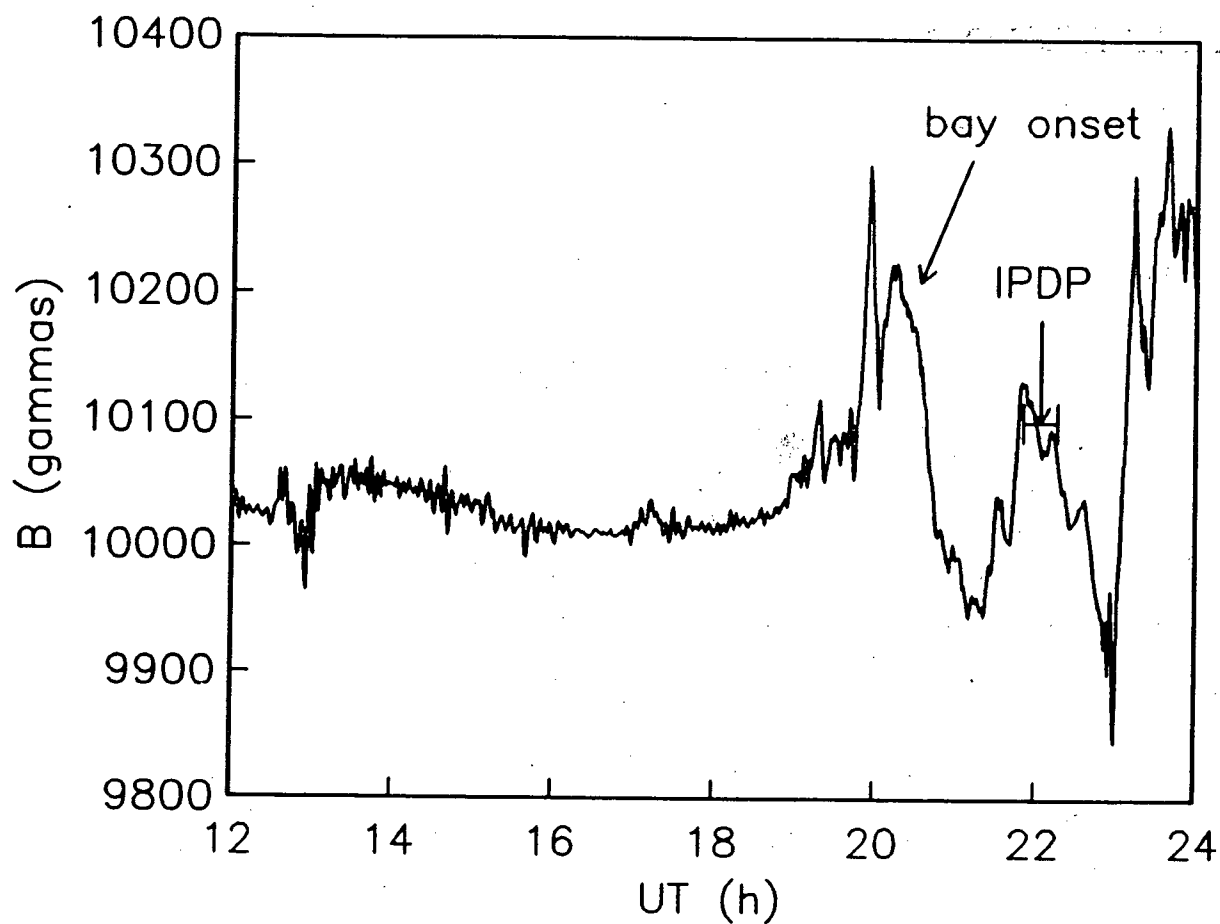


FIGURE 56.

X-component magnetogram from Great Whale River, 1200-2400UT, Feb. 15, 1980. Note the large negative bay beginning at 2036UT, when the station is at 1533GMLT.

interpolation process as for the Feb. 14 event, the drift start time is estimated at $\approx 3 \pm 1$ minutes after substorm onset. Note that in the absence of an estimate of the substorm onset meridian, a typical onset GMLT of 0130 (cf. section 4.1) has been used. The one minute uncertainty is still quite small when compared to the drift times for this event of 78 to 94 minutes, and tests have also shown that the calculated boundary shapes are not sensitive to small (≤ 5 min) changes in the drift time estimates. Since the Dst index and the geosynchronous satellite records indicate a much deeper ΔB for this event than for the Feb. 14 IPDP, a range of $0 \leq \Delta B \leq -160\gamma$ is used in the boundary estimation calculations. The W_i range covered is $10 \leq W_i \leq 300$ keV, virtually the entire range of energies possibly related to IPDPs.

From all the calculations over these parameter ranges, the optimum curve-fit boundary emerges as that calculated using $W_i = 30\text{KeV}$ and $\Delta B = -130\gamma$. This injection boundary produced the best ratings sum; 38 out of a maximum of 50. The boundary calculated from this pair had each of the boundary shape, frequency match, and boundary match criteria rated as among the best, resulting in the highest ratings sum. The ΔB and W values associated with the best case boundary are within the acceptable ranges for this IPDP. The model plot of the selected boundary is shown in figure 57.

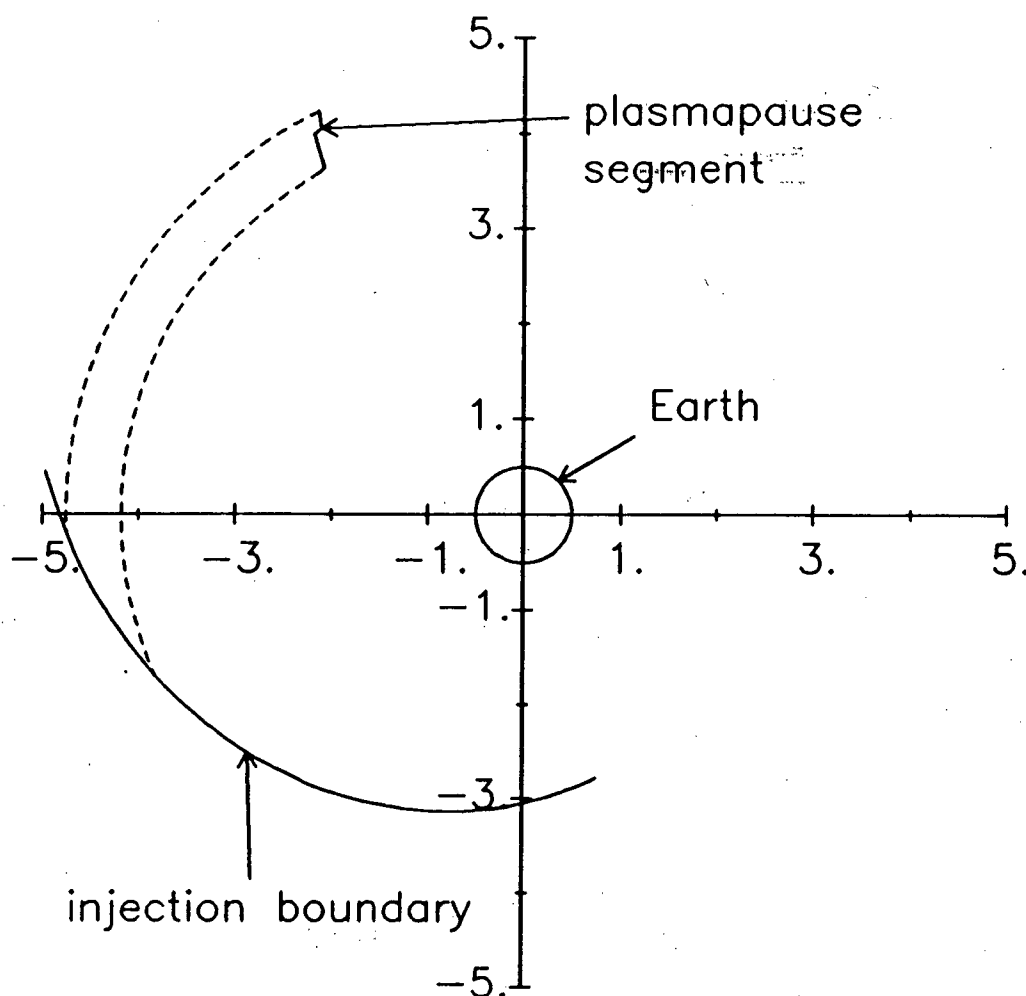


FIGURE 57.

Model plot for Feb. 15 event, showing the injection boundary selected and the plasmopause segment defined by the IPDP generation region (L,GMLT) coordinates. The region through which the protons drifted for this IPDP (as observed on the Saskatchewan line) is enclosed by the dashed lines. The sun is towards the top of the page, and the distance labels on the axes are in L (Earth radii). Note that the source region GMLTs (near 1400) are quite early compared to typical IPDPs.

Note that the IPDP protons begin their drift from a boundary segment in the latter part of the dusk sector, confirming the drift start time estimates discussed above.

The proton energy evolution for the Feb. 15 IPDP is shown in figure 58. For this IPDP, the energy is increasing with time, rather than decreasing as would have previously been expected (cf. section 4.2.3). As with the Feb. 14 event, a rapid inward movement of the plasmopause during the IPDP may be responsible for this unusual behaviour. Correspondingly, the frequency shift due to the hot proton energy change effect, also plotted in figure 58, must show a slight *decreasing* frequency trend.

The magnetic field strength profile and its corresponding frequency shift are also illustrated in figure 58, along with the observed frequency rise for comparison. In this case, the ΔB adjustment to the inward motion mechanism makes this frequency rise much larger than that for the unaltered, or $\Delta B = 0$, inward motion mechanism (cf. fig. 39); here it actually reaches 116% of the total observed IPDP frequency shift, as opposed to only 60% without the ΔB adjustment. The combined frequency effects of proton energy and magnetic field variations in the IPDP source region are plotted in figure 59, showing that the negative azimuthal drift effect brings the ΔB -adjusted inward motion frequency rise down into line with the

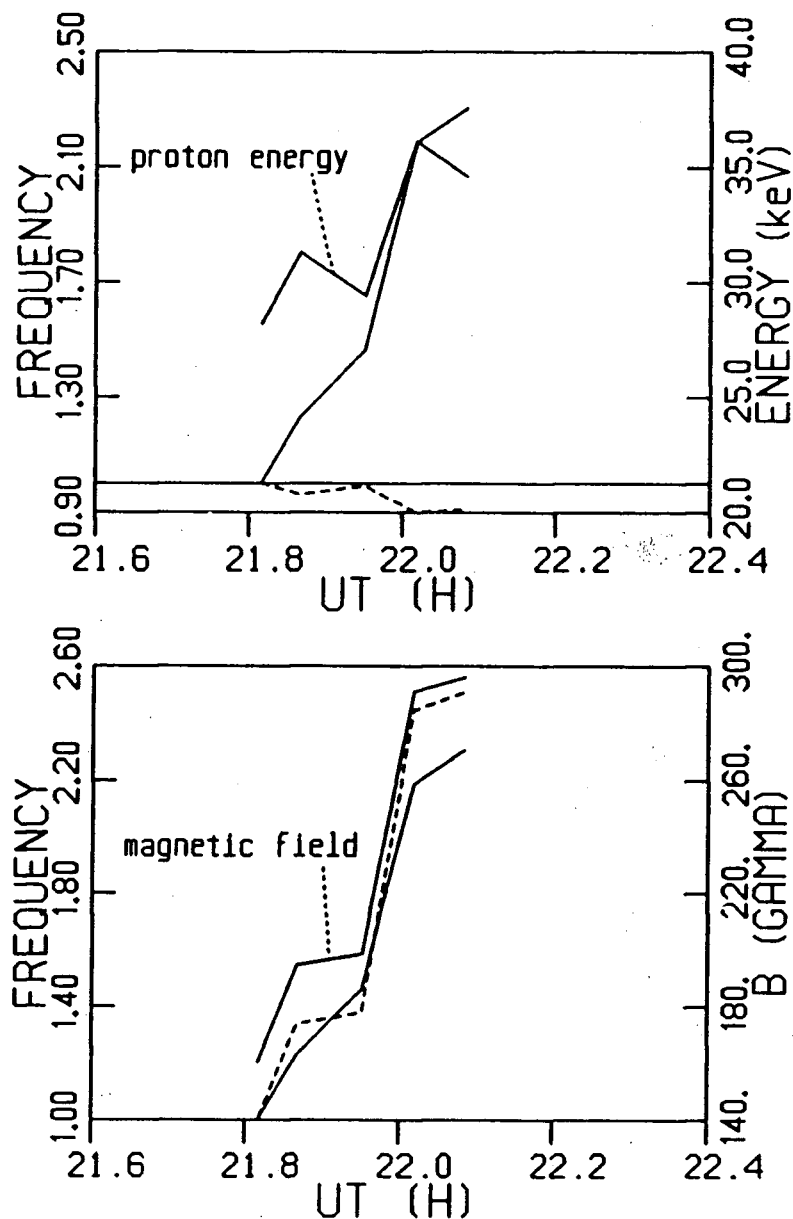


FIGURE 58.

Top: proton energy profile plus the observed (solid line) and azimuthal drift mechanism predicted (dashed line) frequency profiles (normalized) for the Feb. 15 IPDP. Bottom: magnetic field strength profile plus the observed (solid line) and ΔB -adjusted inward motion mechanism predicted (dashed line) frequency profiles for the Feb. 15 IPDP.

observed frequency shift of this event.

It can be concluded, then, that the Feb. 15 IPDP's frequency rise is produced solely by the inward motion mechanism operating in a depressed ($\sim 130\gamma$) magnetic field environment. The hot proton energy change effect does not contribute at all; instead, it actually depresses the frequency rise somewhat. Again, recall that the increasing field mechanism is likely a very minor player in this event (cf. section 5.2).

In summary, this section has presented a method for estimating the injection boundary position using ground based IPDP data, and then used it to assess the frequency effects of proton energy changes for two IPDPs. The results show that proton energy changes have a comparatively minor effect on the frequency rises of these events.

5.4. LONGITUDINAL IPDP DEVELOPMENT

In the previous sections of this chapter, IPDPs have been studied using a north-south line of stations. In this section, data from the southern east-west line (cf. section 2.1, fig. 3) is analysed in order to gain further insight into the longitudinal characteristics of the IPDP generation region. In addition to the two events studied in sections 5.1 and 5.3, a third IPDP is also analysed here; the Feb. 24c event. While data for the original two IPDPs are

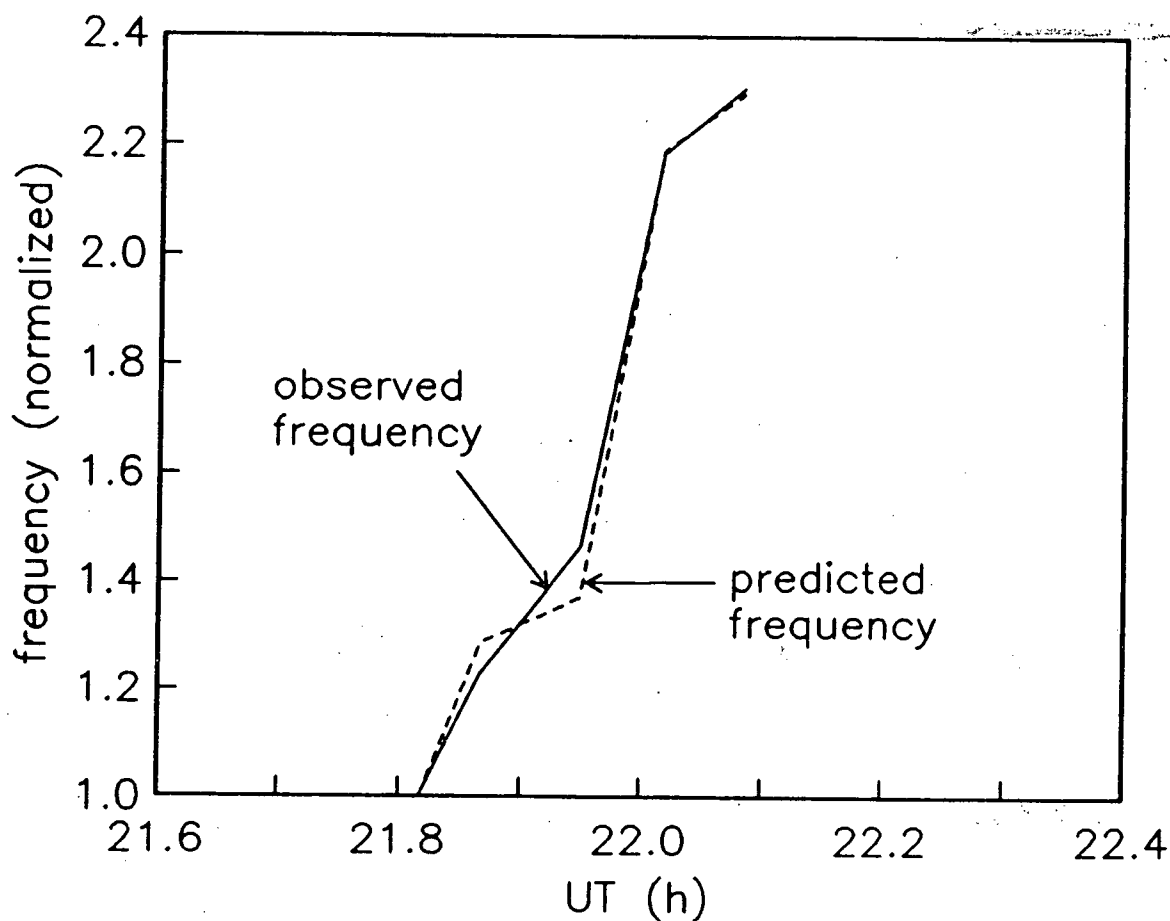


FIGURE 59.

The frequency rises as observed and as calculated for the combined azimuthal drift - ΔB -adjusted inward motion mechanisms for the Feb. 15 event, showing the excellent agreement between the two curves.

available only from GM and PS, the eastern and central sites in the southern east-west line, the Feb. 24c event has data available from all three sites in this line. Note that the longitudinal difference between GM and PS is only 14.6° , but that the longitudinal span of the line expands to 34.6° when PG, the westernmost station, is included.

The detailed longitudinal analyses are presented below for each event. They are followed by a discussion of the results of these analyses.

5.4.1. Feb. 14 Event

The first IPDP discussed is the Feb. 14 event. Figure 60 demonstrates the frequency evolution of this event at both GM and PS. Note that the frequency is generally higher to the east, at GM, averaging $\approx 0.06\text{Hz}$ above PS. The frequency slopes are similar, with that for GM, 0.43Hz/h , being slightly higher than the 0.36Hz/h slope at PS. However, as can be seen in figure 60, there are some shorter term variations in frequency slope which are not shared by both stations. The event was observed to begin at approximately the same time at GM and PS, $\approx 0835\text{UT}$, but it lasted ≈ 10 minutes longer, until 0950UT , at GM, the eastern station.

Comparisons between the IPDP signals as observed at GM and PS are made using cross-correlations. A series of 2048

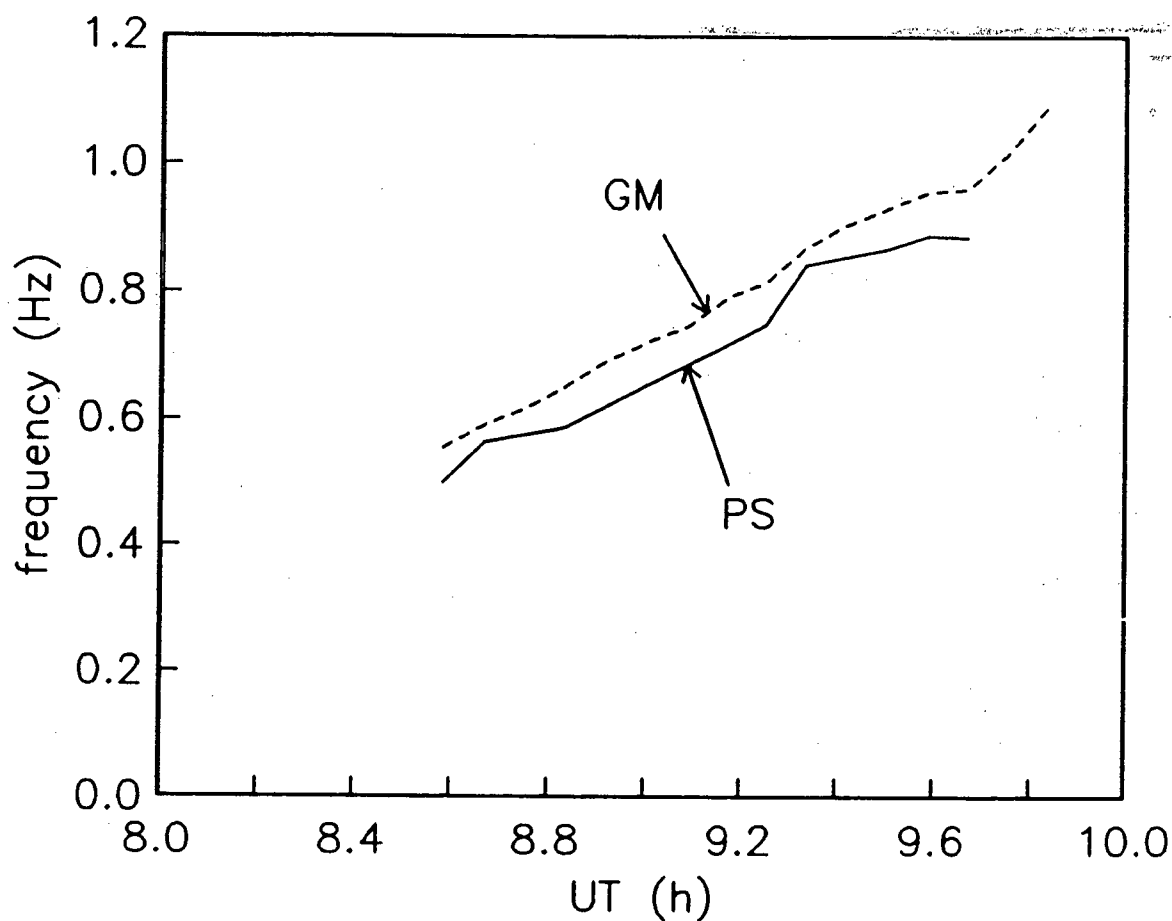


FIGURE 60.

Frequency evolution at both GM and PS for the Feb. 14 event. Note the higher frequencies at GM and the different local variations in slope at the two stations.

point (9.1 min) data windows, starting every five minutes, from GM were correlated with a 8192 point (36.4 min) data window, starting at 0845UT, from PS. The results show correlation coefficients to be ≤ 0.2 at all time shifts for each window, indicating no significant correlation between these stations. For comparison, stations on the same meridian, PS and LL, have records which appear to be very similar, with a correlation coefficient of 0.36 for a lead of only 1.3 seconds at LL using the same data window as above for PS correlated with a 9.1 minute window starting at 0855UT from LL. Note, however, that PS and LL are separated only by 1.2° of latitude (cf. section 2.1).

An examination of power spectra computed from the same time intervals at GM and PS shows the differences in the IPDP signal as observed by these two stations (see fig. 61); the spectra not only cover somewhat different bands, but the distribution of power within the bands is also dissimilar.

5.4.2. Feb. 15 Event

The frequency evolution of the Feb. 15 event is shown in figure 62, demonstrating that the frequency is again higher to the east, at GM, though by only an average of $\approx 0.02\text{Hz}$. As well, the slopes are very similar here, though the average slope is slightly higher at PS, 1.06Hz/h , than at GM, 1.01Hz/h . As for the Feb. 14 IPDP, the event onset

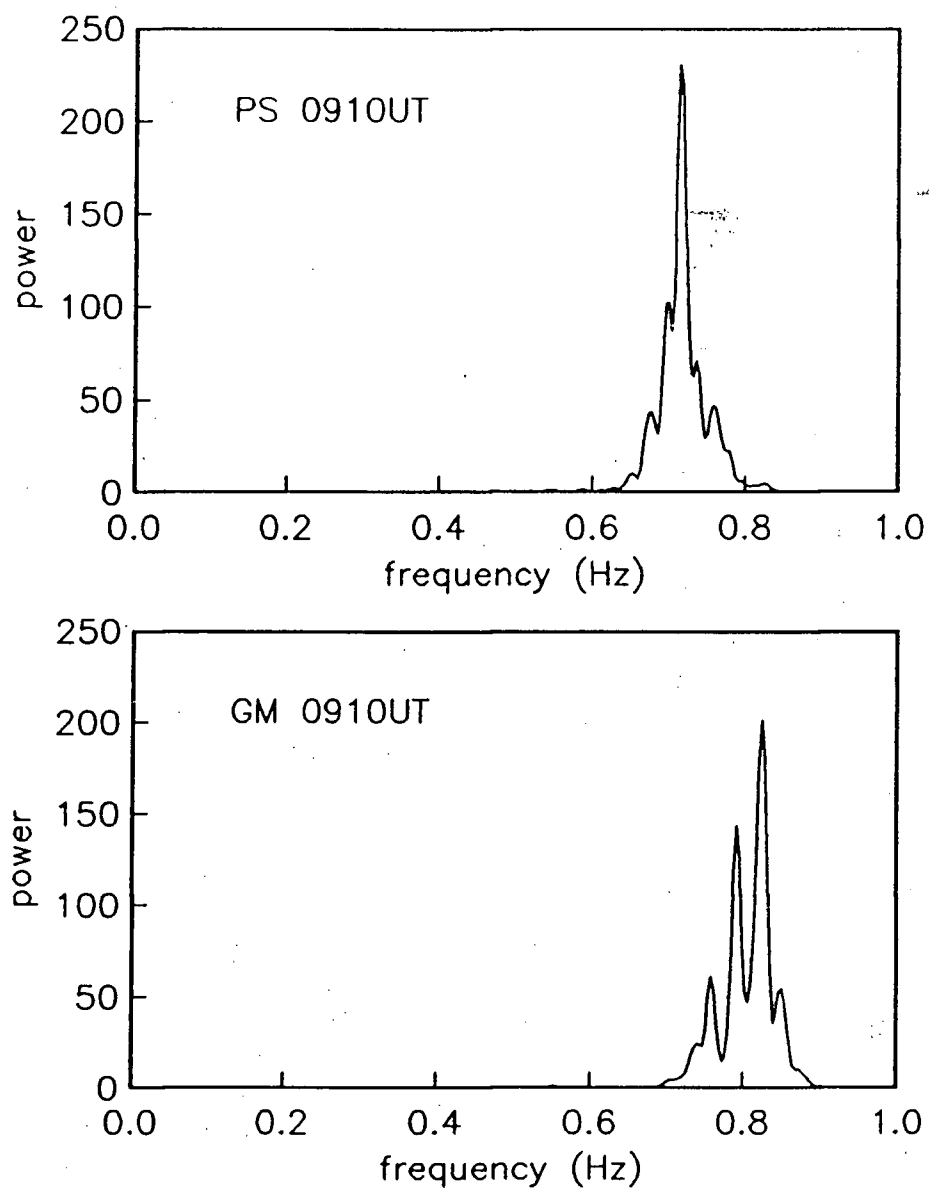


FIGURE 61.

Top: Power spectra from PS for 0910UT, February 14. Bottom: Power spectra from GM for same time period. Both spectra are of the total horizontal component from a 4.6 minute data window. Note the different signal bands and the different power distributions in these two spectra.

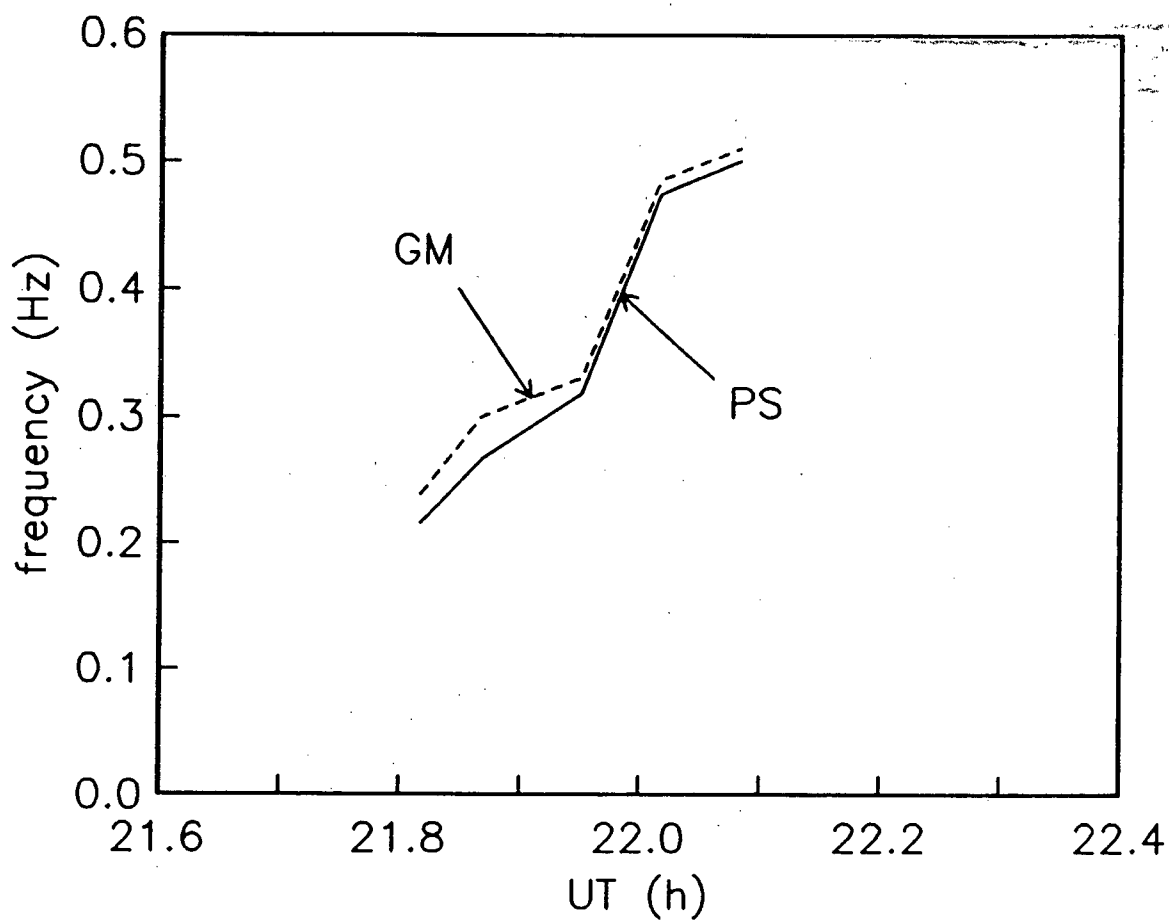


FIGURE 62.

Frequency evolution for GM and PS, Feb. 15 event. GM has the higher frequencies, but the slope is slightly lower than at PS.

times are essentially the same; 2147UT at GM and 2148UT at PS. However, in this case, the duration was longer at the western station, PS, at 25 minutes, as compared to 20 minutes at GM. Note that the detailed analysis of this IPDP in the previous sections was only carried out to 2205UT, since a very weak signal, and consequently poor signal/noise ratio, made the analysis results of the last section very difficult to interpret and therefore unreliable.

A comparison of the appearance of the IPDP signal as seen at GM and PS also yields a result unlike that for the Feb. 14 event. Here, each station exhibits similar high amplitude intervals on the magnetograms, though these intervals do not necessarily occur precisely simultaneously. Cross-correlational analysis shows that each interval at GM leads the corresponding one at PS by between 54 and 4 seconds, with the largest leads being earlier in the event. In contrast to this, these high amplitude intervals appear nearly simultaneously, the time shift always being <5 seconds, at PS and LL, which are separated only in latitude. The correlation coefficients of up to 0.60 are also much higher between PS and LL than between PS and GM, which show coefficients of up to only 0.39. For this event, the correlations are done using 1024 point (4.6 min) data windows from all stations. Note that the high amplitude intervals are short compared to the 4.6 minute data windows.

Correlations were performed on four windows with start times of 2150, 2154, 2158, and 2203 UT. Figure 63 shows sample correlations between PS and GM and between PS and LL from the 2154UT window. Different background noise conditions at each site and low amplitudes are believed to be responsible for the relatively low levels of the correlation coefficients.

The individual power spectra exhibit the same kinds of differences between GM and PS as they did for the Feb. 14 IPDP, even though the magnetograms from these two stations appear, at least at first glance, to be quite similar in this case.

5.4.3. Feb. 24c Event

This event was observed at all three stations in the southern east-west line (GM, PS, and PG). The frequency profiles from these stations are shown in figure 64. Though the PS and GM frequencies appear to be quite similar, to the west the PG station observed frequencies averaging 0.07Hz lower than the other stations. The average frequency slopes at each site are similar, lying near 0.3Hz/h, with PG being slightly higher and GM somewhat lower than this value. However, as figure 64 shows, there are different shorter term variations in slope within the event at each site which can make the slopes quite different between stations for

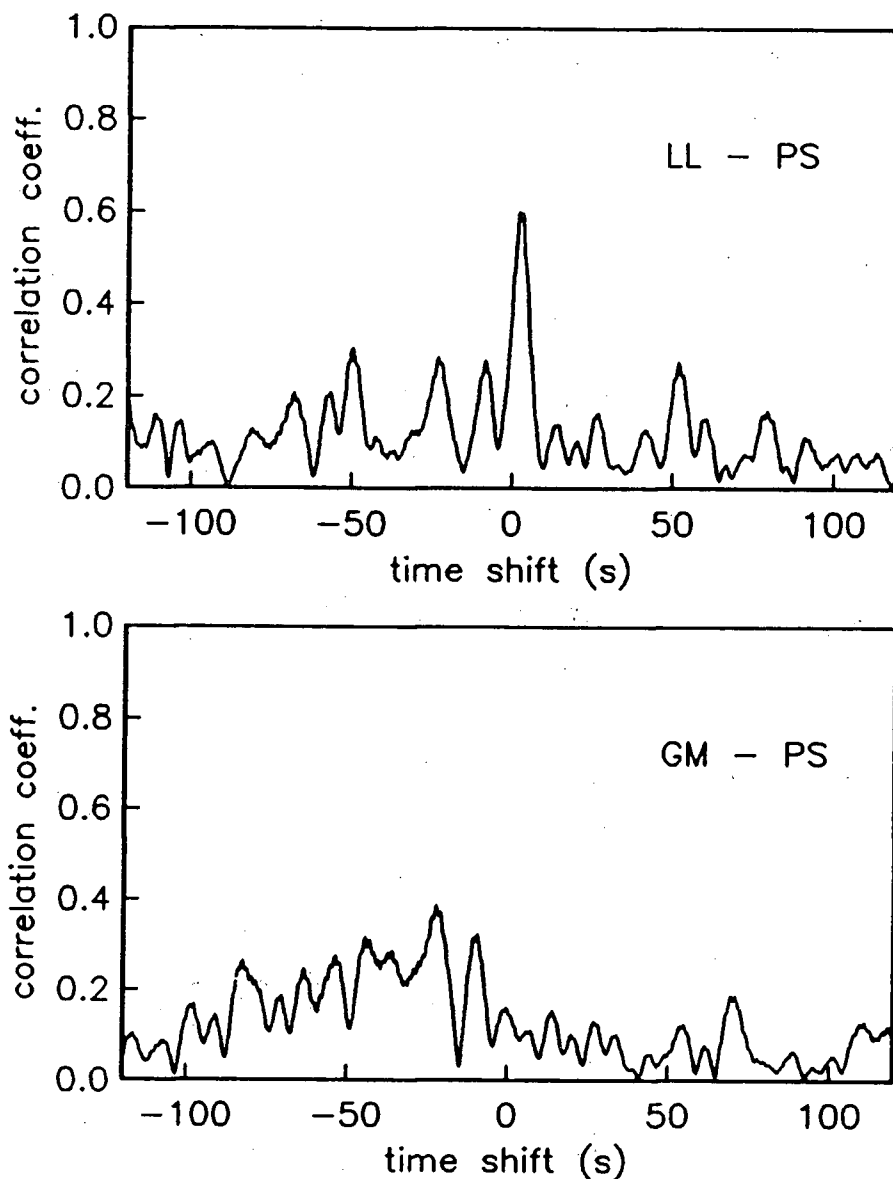


FIGURE 63.

Top: Sample cross-correlation between LL and PS from the Feb. 15 event, showing that the good correlation between these two sites, which are on the same meridian, is near zero lag. Bottom: Cross-correlation between GM and PS from the same time interval. Both correlations use the Y component only (with a 0.2-0.6 Hz bandpass filter). Note the significantly poorer correlation these two longitudinally separated sites. Here, GM leads PS by 22 seconds.

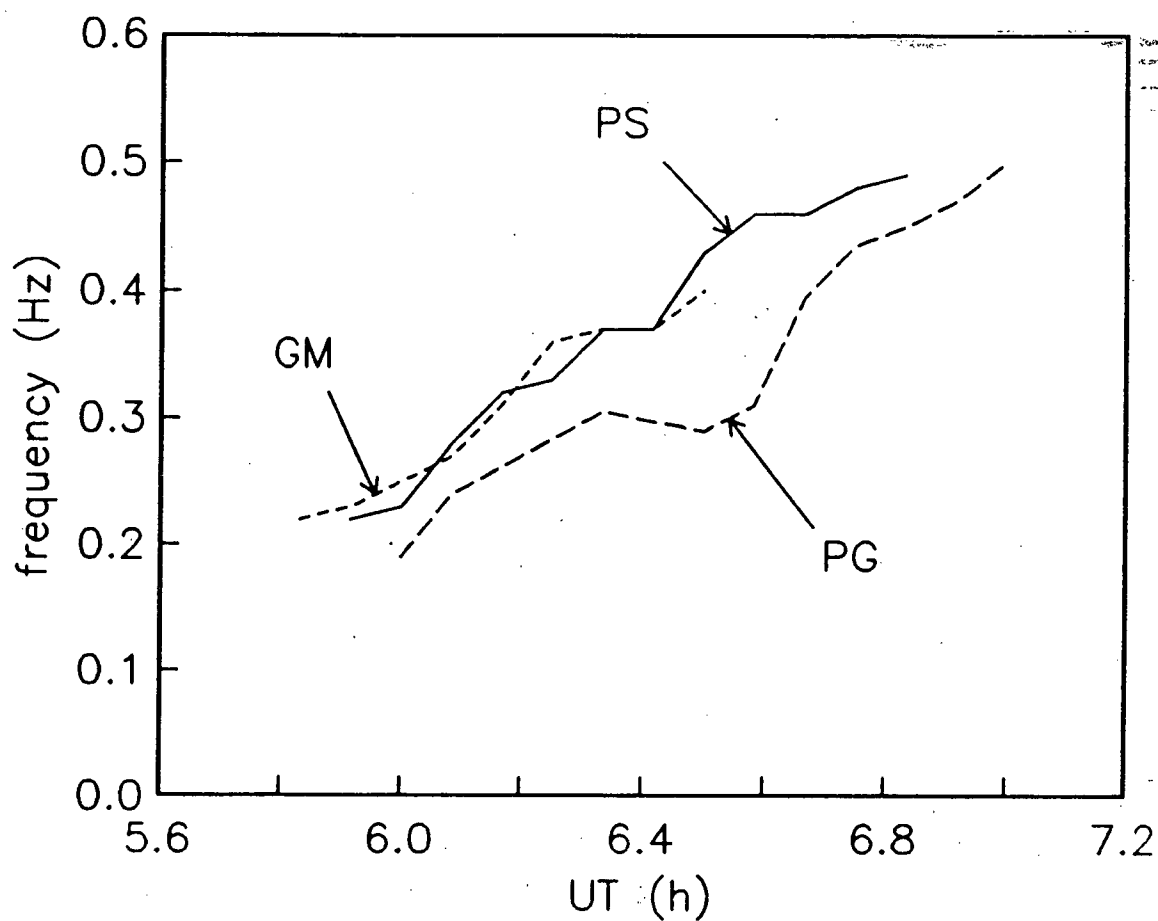


FIGURE 64.

Frequency evolution for all three stations observing the Feb. 24c IPDP. PG, in the west, has the lowest frequencies. Note also that there are significant local variations in slope between the stations.

some intervals during the IPDP. The event intervals observed at each site are: GM, 0550 to 0630 UT; PS, 0554 to 0650 UT; and PG, 0558 to 0700 UT. Note that the GM data were very noisy and difficult to interpret, making conclusions based on it less reliable.

As with the Feb. 14 event, but unlike the Feb. 15 IPDP, there does not appear to be any significant correlation of the signals between any of the three stations in the east-west line, since all correlation coefficients were again <0.2 . No other recording sites on any of the north-south lines are available for comparison for this event.

The power spectra for this event behave much as has been described for the previous two cases, with the frequency bands covered and the power distribution within the bands being notably different at each site for the same time intervals.

5.4.4. Discussion

All three events discussed here exhibit generally higher frequencies to the east. This implies generation on lower L-shells to the east, and thus indicates that the generation region follows the plasmopause shape which is at lower L at later, or more easterly GMLTs. Two of the three IPDPs, Feb. 15 and Feb. 24c, show longer durations to the

west and earlier onset times to the east. This is consistent with the model discussed in section 4.1, in which the later onsets imply longer drift times which create a larger GMLT spread in the drifting proton cloud, giving longer event durations. Note that very low amplitudes at the start or end of an event can make it very difficult to correctly pick the start or end times, which may be why the duration and/or onset time of the Feb. 14 IPDP does not fit the above pattern.

For all three events, individual power spectra calculated from identical time intervals show major differences between sites on the east-west line, but not for north-south line stations. Each event also shows temporary differences in slope exhibited by the stations on the east-west line. Two of the three IPDPs studied, Feb. 14 and Feb. 24c, show no significant correlation between stations on the east-west line, though the third event, the Feb. 15 IPDP, does show a weak east-west correlation. These results imply that each station receives the IPDP signals from a different part of the magnetospheric source region.

The east-west correlations exhibited by the Feb. 15 event could be caused by the magnetospheric source regions "above" each station receiving similar "packets" of drifting protons nearly simultaneously, thus creating similar high amplitude intervals at each station with time separations of

less than one minute. Note that good correlations are observed between stations separated in latitude only, illustrating good north-south ducting from a common secondary source.

In summary, the primary point of this analysis is to show that there are significant differences within an IPDP as observed on an east-west line of stations. These differences, which include variations in magnetograms, frequency, slope, and spectra, can be seen over as little as 15° GM Long., and imply that each site is seeing a separate magnetospheric source. The east-west pattern of these differences, which also include onset times and durations, is consistent with the model discussed in section 4.1, with simultaneous IPDP generation over a longitudinally extended area of the plasmopause after westward drift of the protons on different L-shells. Each ground station on the east-west line is then seeing the IPDP as generated on a different section of the plasmopause close to that station's meridian, resulting in the inter-station variations in the IPDP signal described above. Good north-south propagation within the ionosphere ensures that all sites on one meridian see the same signals from the same source, with only the polarization characteristics and amplitudes altered by this ionospheric propagation.

5.5. DISCUSSION OF EXPERIMENTAL RESULTS

In studying the frequency rise of IPDPs, we have tested three mechanisms capable of producing this effect; the inward motion of the magnetospheric source region, an increasing background magnetic field strength in the source region, and the proton energy variations produced during the azimuthal drift of the hot protons. The assessment of these mechanisms has been carried out in the context of the model described in Chapter Four.

In sections 5.1 through 5.3, it was shown that the inward motion was, for the events analyzed, the primary, though not always the entire, cause of the IPDPs' frequency rise. It is important to note that, for a proper assessment of this mechanism, the effect of the ring current magnetic field on the radial geomagnetic field profile must be taken into account, since it can, if the ring current is well developed, significantly enhance the magnitude of the frequency rise attributable to inward motion of the IPDP generation region. This represents a first, if simple, step beyond the purely dipole field model discussed in Chapter Four.

The inward motion of the source region has earlier been described as being due to the shape of the plasmopause, with the possible addition of inward motion of the plasmopause itself (cf. Chapter Four). The inward motion determined here

would be the sum of these two effects, if both are present. The irregular rate of inward motion demonstrated by both IPDPs studied could then be interpreted to mean that the plasmopause shape itself is somewhat irregular with the plasmopause moving either very little or at a constant rate during these events. Alternately, during the periods of faster motion exhibited during their central time spans by both IPDPs (cf. fig. 31, 38), additional plasmopause inward displacement could be superimposed on a relatively smooth inward motion due to a smoother plasmopause shape. That the plasmopause would move most during the middle of an IPDP event may not be unexpected, since the electric and magnetic fields which control the plasmopause position may also be changing at this time due to magnetospheric substorm effects. These effects, which include the changing plasma and field environments associated with the proton westward drift process, could have an effect on the plasmopause position, and if so then may affect the plasmopause most when the protons generating the IPDP are arriving there.

The ring current - IPDP model discussed in section 5.2, though significantly improved over previous models, is still quite simple. Nevertheless, the conclusion can be drawn from it that the increasing magnetic field mechanism for the IPDP frequency rise is not a necessary condition for IPDPs to occur, since case I and III events do occur (cf. section

5.2). It can, however, under certain circumstances, still contribute to the frequency shift of some IPDPs, such as case II and IV events. It is also shown that the geosynchronous satellite magnetograms alone cannot be used as a method of determining IPDP source region field behaviour unless the IPDP is being generated in the vicinity of $L = 6.6$.

The increasing field mechanism does not appear to have contributed significantly to the IPDPs examined here. For this mechanism, however, the assessment remains only a qualitative one due to the difficulty in quantitatively determining any changes in magnetic field strength in the IPDP source region from the information available. Lower altitude, that is, $L < 6.6$, satellite magnetic field measurements in the generation region during an IPDP would be necessary to evaluate quantitatively the increasing field mechanism effect on IPDP frequency shifts.

The hot proton energy change effect played a secondary role in creating the IPDP frequency shifts observed here. In one event, it actually had the unusual effect of suppressing the frequency rise. Section 5.3 showed that both the ring current induced magnetic field depression and the injection boundary position must be estimated in order to find the energies of the protons generating the IPDP. This estimation process requires the assumption that only the proton energy

effect and the ΔB -adjusted inward motion mechanism are operating, and would be inappropriate if applied to an IPDP to which the increasing field mechanism was believed to be making a significant contribution. It should also be pointed out that the selection process by which the best field depression value and injection boundary position are chosen is partially subjective, especially with regards to the weights assigned to each of the selection criteria.

The analysis of the longitudinal structure and development of IPDPs presented in section 5.4 indirectly supports the frequency rise results discussed above by supporting the model from which they are produced. In addition, the detailed analyses of the IPDPs showed that longitudinal variations within IPDP events exist over much smaller longitudinal separations than previously reported (cf. section 3.3).

In considering the overall significance of the results discussed above, it must be remembered that only two IPDP events have been studied in detail. From just two events, strong conclusions regarding the relative importance of the different frequency shift mechanisms cannot be extended to reliably apply to all IPDP events. For example, the degree of influence of each mechanism may change with varying magnetospheric conditions and/or IPDP source region

locations. It is interesting to note that the two IPDPs studied here did occur at disparate GMLT locations and under diverse levels of magnetospheric activity. While both exhibited strong inward motion mechanism contributions, their hot proton energy change effects were of opposite sign, indicating that such systematic variations in the frequency shift mechanisms' contributions are at least a possibility. To study potential traits such as these, the analysis of many more events would be required. The negative frequency shift from the hot proton energy change effect displayed by one IPDP here (cf. fig. 58) has not been previously reported and was termed unusual above, yet, without an extended study covering many events, it is not really known how rare such behaviour actually is.

It is also necessary to be somewhat cautious when considering the details of the individual results. We must bear in mind such things as the incomplete data set on which the analyses were performed, the somewhat simplistic application of ionospheric duct theory necessary, and the simplifying assumptions involved in the IPDP generation model. These aspects can affect not only the accuracy of the IPDP source position determination and inward motion frequency shift estimate, but also the azimuthal drift frequency shift estimate, since this depends, in part, on the source inward motion results. The azimuthal drift

estimate also depends on the assumption that all injection boundaries take the form expressed by equation 5.8. However, barring any major shifts in our general understanding of such processes as injection boundary formation, ring current development, or ionospheric duct propagation, the general conclusions regarding the relative importance of each of the frequency shift mechanisms to the events studied here should be valid.

CHAPTER 6. CONCLUSION

We have made a quantitative study of two IPDP frequency shift mechanisms, supported by a qualitative assessment of the role of a potential third mechanism. Within the framework of a magnetospheric IPDP generation model, it has become evident that the inward motion of the magnetospheric source region is the dominant cause of the IPDP frequency rise, with the hot proton energy variations contributing to a lesser degree. The model considered consists of a westward drift of energetic protons from a substorm injection boundary and subsequent wave amplification by these protons at the plasmopause through the proton-cyclotron instability. These conclusions are the outcome of the detailed analyses of the two events studied here.

These results are supported by model calculations (section 4.4), which also show the inward motion mechanism generally contributing significantly more than the hot proton energy change effect. In addition, model calculations show that the inward motion can be largely due to the shape of the plasmopause, as opposed to inward displacement of the plasmopause. These model calculations also show that the possibility exists that eastward developing IPDPs, opposite to what is now considered the normal trend, may occur.

We have shown that previous methods of interpreting the increasing magnetic field mechanism's effect on IPDPs gave

insufficient attention to the differences in temporal field behaviour between geosynchronous orbit and the somewhat lower IPDP source regions as caused by the dynamic nature of the storm time ring current. When even a simple description of ring current dynamics is used, including the ring current's growth, inward displacement, and decay during the course of a magnetic storm, it becomes evident that the increasing field mechanism may enhance, suppress, or have no effect on an IPDP's frequency rise depending on the event's source region location and the storm phase during which it occurs. However, this mechanism is never a required process upon which an IPDP's existence depends.

In contrast to this, due to plasmopause geometry, some inward motion of the IPDP source region will always exist. However, actual plasmopause inward displacement will not necessarily always take place. This inward motion mechanism is, though, the only mechanism which will always be present, as shown by the fact that one of the two events studied displayed hot proton energy variations which resulted in a slight suppression of the frequency rise. In spite of the fact that azimuthal drift velocities will always produce a softening proton energy spectrum as observed at constant L , rapid cross- L motion of the source can reverse this trend, as "seen" by a ground station, yielding an increasing energy trend whose effect acts to depress an IPDP's frequency rise.

Due to limitations of the 1980 IPDP data set used here (cf. sec. 2.1), only two events were studied in detail and even these suffered from incomplete station coverage. Despite this, it has still been possible to gain new insights into the generation processes of IPDPs. In addition, new methods for the study of IPDPs have also been developed, as described in sections 4.4 through 5.4, which provide a good basis for future work using more complete data sets.

As noted in Chapter One, IPDPs have often been touted as a potentially useful tool for the diagnosis of magnetospheric conditions. Unfortunately, this has not been realized to any large extent as yet. Now, however, with a better understanding of the frequency shift mechanisms, we can begin to realize some of the potential of the study of IPDPs. It has been demonstrated here that the detailed study of individual IPDP events can yield information on plasmopause position and movement, drifting proton energies, injection boundary shapes, and ring-current created magnetic field depressions in the IPDP generation region. This is only a beginning, however. The quality and reliability of such information could be improved and other uses of IPDPs made if our understanding of these micropulsations were to be solidified and extended. To do this would require the analysis of many well recorded events from station networks

which include two or more adjacent north-south chains of sites, allowing the development of a two-dimensional picture of IPDP generation founded on experiment. It would also be necessary to include satellite magnetograms from $L < 6.6$ and/or a much more sophisticated ring current model to quantitatively understand the role of temporal magnetic field variations in IPDP generation. If such concerns can be satisfied by future work, IPDPs may finally take their place as a useful type of micropulsation in magnetospheric physics.

REFERENCES

- Althouse, E.L., and J.R. Davis, 1978, Five-station observations of Pc 1 micropulsation propagation: J. Geophys. Res. 83, 132-144.
- Altman, C., and E. Fijalkow, 1980, The horizontal propagation of Pc1 pulsations in the ionosphere: Planet. Space Sci. 28, 61-68.
- Arnoldy, R.L., P.B. Lewis, and L.J. Cahill, 1979, Polarization of Pc 1 and IPDP pulsations correlated with particle precipitation: J. Geophys. Res. 84, 7091-7098.
- Arnoldy, R.L., and T.E. Moore, 1983, Longitudinal structure of substorm injections at synchronous orbit: J. Geophys. Res. 88, 6213-6220.
- Barkova, E.S., and S.I. Solov'ev, 1984, The excitation of geomagnetic pulsations of the Pc 1-2 and ODP type during periods of microsubstorms: Geomag. Aeron. 24, 385-388.
- Berko, F.W., L.J. Cahill, and T.A. Fritz, 1975, Protons as the prime contributors to storm time ring current: J. Geophys. Res. 80, 3549-3552.
- Bossen, M., R.L. McPherron, and C.T. Russell, 1976, Simultaneous Pc 1 observations by the synchronous satellite ATS-1 and ground stations: implications concerning IPDP generation mechanisms: J. Atmosph. Terrest. Phys. 38, 1157-1167.
- Boteler, D.H., 1980, An investigation of polar substorms observed at Halley Bay, Antarctica: M.Sc. thesis, Univ. of British Columbia, Vancouver, 135 pp.
- Campbell, W.H., and T.C. Thornberry, 1972, Propagation of Pc 1 hydromagnetic waves across North America: J. Geophys. Res. 77, 1941-1950.
- Carpenter, D.L., 1966, Whistler studies of the plasmopause in the magnetosphere, 1, Temporal variations in the position of the knee and some evidence of plasma motions near the knee: J. Geophys. Res. 71, 693-709.
- Chappell, C.R., K.K. Harris, and G.W. Sharp, 1971, The dayside of the plasmasphere: J. Geophys. Res. 76, 7632-7647.

- Cornwall, J.M., F.V. Coroniti, and R.M. Thorne, 1970, Turbulent loss of ring current protons: J. Geophys. Res. 75, 4699-4709.
- Cornwall, J.M., and M. Shulz, 1971, Electromagnetic ion-cyclotron instabilities in multicomponent magnetospheric plasmas: J. Geophys. Res. 76, 7791-7796.
- Dobnaya, B.V., E.T. Matveyeva, V.A. Troitskaya, and F.Z. Feygin, 1984, Oscillations of diminishing period on the morning side of the magnetosphere: Geomag. Aeron. 24, 804-808.
- Duffus, H.J., P.W. Nasmyth, J.A. Shand, and C. Wright, 1958, Sub-audible geomagnetic fluctuations: Nature 181, 1258-1259.
- Fraser, B.J., 1975a, Ionospheric duct propagation and Pc 1 pulsation sources: J. Geophys. Res. 80, 2790-2796.
- Fraser, B.J., 1975b, Polarization of Pc 1 pulsations at high and middle latitudes: J. Geophys. Res. 80, 2797-2807.
- Fraser, B.J., and S. Wawrzyniak, 1978, Source movements associated with IPDP pulsations: J. Atmosph. Terrest. Phys. 40, 1281-1288.
- Fukunishi, H., 1969, Occurrence of sweepers in the evening sector following the onset of magnetospheric substorms: Rept. Ionos. Space Res. Japan 23, 21-34.
- Fukunishi, H., 1973, Occurrence of IPDP events accompanied by cosmic noise absorption in the course of proton aurora substorms: J. Geophys. Res. 78, 3981-3986.
- Fukunishi, H., T. Toya, K. Koike, M. Kuwashima, and M. Kawamura, 1981, Classification of hydromagnetic emissions based on frequency-time spectra: J. Geophys. Res. 86, 9029-9039.
- Fukunishi, H., and T. Toya, 1981, Morning IPDP events observed at high latitudes: J. Geophys. Res. 86, 5701-5709.
- Gendrin, R., 1970, Substorm aspects of magnetic pulsations: Space Sci. Rev. 11, 54-130.

- Gendrin, R., M. Gokhberg, S. Lacourly, and V.A. Troitskaya, 1966, Apparition simultanee de pulsations magnetiques d'ultrabasse frequence en phase en deux points conjugees: C. R. Acad. Sci. 262, 845-848.
- Gendrin, R., S. Lacourly, A. Roux, J. Solomon, F.Z. Feigin, M.V. Gokhberg, and V.A. Troitskaya, 1971, Wave packet propagation in an amplifying medium and its application to the dispersion characteristics and to the generation mechanisms of Pc 1 events: Planet. Space Sci. 19, 165-194.
- Gendrin, R., S. Lacourly, V.A. Troitskaya, M. Gokhberg, and R.V. Shepetnov, 1967, Caracteristiques des pulsations irregulieres de periode decroissante (I.P.D.P.) et leurs relations avec les variations du flux des particules piegees dans la magnetosphere: Planet. Space Sci. 15, 1239-1259.
- Gomberoff, L., and S. Cuperman, 1982, Combined effect of cold H^+ and He^+ ions on the proton cyclotron electromagnetic instability: J. Geophys. Res. 87, 95-100.
- Greifinger, P., 1972, Micropulsations from a finite source: J. Geophys. Res. 77, 2392-2396.
- Greifinger, C., and P.S. Greifinger, 1968, Theory of hydromagnetic propagation in the ionospheric waveguide: J. Geophys. Res. 73, 7473-7490.
- Greifinger, C., and P. Greifinger, 1973, Wave guide propagation of micropulsations out of the plane of the geomagnetic meridian: J. Geophys. Res. 78, 4611-4618.
- Gustafsson, G., 1984, Corrected geomagnetic coordinates for epoch 1980: Magnetospheric currents, Ed.: T.A. Potemra, American Geophysical Union, Washington, D.C., 357 pp.
- Hakura, Y., 1965, Tables and maps of geomagnetic coordinates corrected by the higher order spherical harmonic terms: Rep. Ionos. Space Res. Jap. 19, 121-157.
- Hayashi, K., S. Kokubun, T. Oguti, K. Tsuruda, S. Machida, T. Kitamura, O. Saka, and T. Watanabe, 1981, The extent of Pc 1 source region in high latitudes: Can. J. Phys. 59, 1097-1105.

- Hayashi, K., T. Yamamoto, S. Kokubun, T. Oguti, T. Ogawa, N. Iwagami, T. Araki, T. Kitamura, O. Saka, K. Makita, N. Sato, T. Watanabe, R.E. Horita, D.J. McEwen, J.S. Kim and A. Egeland, 1988, Multi-station observation of IPDP micropulsations - two-dimensional distribution and evolution of the source regions: J. Geomag. Geoelectr. **40**, 583-619.
- Heacock, R.R., 1967, Evening micropulsation events with a rising midfrequency characteristic: J. Geophys. Res. **72**, 399-408.
- Heacock, R.R., 1971, Spatial and temporal relations between Pi bursts and IPDP micropulsation events: J. Geophys. Res. **76**, 4494-4504.
- Heacock, R.R., 1973, Type IPDP magnetospheric plasma wave events: Nature Phys. Sci. **246**, 93-96.
- Heacock, R.R., D.J. Henderson, J.S. Reid, and M. Kivinen, 1976, Type IPDP pulsation events in the late evening-midnight sector: J. Geophys. Res. **81**, 273-280.
- Higel, B., and W. Lei, 1984, Electron density and plasmopause characteristics at 6.6R_E: a statistical study of the GEOS 2 relaxation sounder data: J. Geophys. Res. **89**, 1583-1601.
- Horita, R.E., J.N. Barfield, R.R. Heacock, and J. Kangas, 1979, IPDP source regions and resonant proton energies: J. Atmosph. Terrest. Phys. **41**, 293-309.
- Jacobs, J.A., 1970, Geomagnetic micropulsations: Springer-Verlag, New York, N.Y., 179 pp.
- Jacobs, J.A., and T. Watanabe, 1962, Propagation of hydromagnetic waves in the lower exosphere and the origin of short period geomagnetic pulsations: J. Atmosph. Terrest. Phys. **24**, 413-434.
- Jackson, J.D., 1975, Classical electrodynamics: John Wiley & Sons, Inc., New York, 848 pp.
- Kamide, Y., F. Yasuhara, and S.I. Akasofu, 1976, A model current system for the magnetospheric substorm: Planet. Space Sci. **24**, 215-222.
- Kanasewich, E.R., 1981, Time sequence analysis in geophysics, third edition: University of Alberta Press, Edmonton, Alberta, 480 pp.

- Kangas, J., L. Lukkari, and R.R. Heacock, 1974, On the westward expansion of substorm-correlated particle phenomena: J. Geophys. Res. 79, 3207-3210.
- Kawasaki, K., and S.I. Akasofu, 1971, Geomagnetic storm fields near a synchronous satellite: Planet. Space Sci. 19, 1339-1347.
- Kivelson, M.G., 1976, Magnetospheric electric fields and their variation with geomagnetic activity: Rev. Geophys. Space Phys. 14, 189-197.
- Knafllich, H.B., and J.F. Kenney, 1967, IPDP events and their generation in the magnetosphere: Earth Planet. Sci. Lett. 2, 453-459.
- Koleszar, T.W., 1980, An investigation of the frequency shift mechanisms of IPDP type pulsations: M.Sc. thesis, Univ. of British Columbia, Vancouver, 79 pp.
- Lukkari, L., J. Kangas, and H. Ranta, 1977, Correlated electron precipitation and magnetic IPDP events near the plasmopause: J. Geophys. Res. 82, 4750-4756.
- Lyons, L.R., and D.J. Williams, 1980, A source for the geomagnetic storm main phase ring current: J. Geophys. Res. 85, 523-530.
- Maltseva, N.F., A.V. Gul'yel'mi, and V.N. Vinogradova, 1970, Effect of westward frequency drift in the intervals of pulsation with decreasing period: Geomag. Aeron. 10, 745-746.
- Maltseva, N.F., L.T. Afanasyeva, V.A. Troitskaya, T. Pikkarainen, H. Ranta, A. Ranta, and J. Kangas, 1985, On the radial displacement of sources of ODP (oscillations of decreasing period) and localized outpourings of high-energy electrons: Geomag. Aeron. 25, 359-364.
- Maltseva, N., V. Troitskaya, E. Gerazimovitch, L. Baransky, S. Åsheim, J. Holtet, K. Aasen, A. Egeland, and J. Kangas, 1981, On temporal and spatial development of IPDP source region: J. Atmosph. Terrest. Phys. 43, 1175-1188.
- Manchester, R.N., 1966, Propagation of Pc 1 micropulsations from high to low latitudes: J. Geophys. Res. 71, 3749-3754.

- Manchester, R.N., 1968, Correction of Pc 1 micropulsations at spaced stations: J. Geophys. Res. 73, 3549-3556.
- Mauk, B.H., and C.E. McIlwain, 1974, Correlation of Kp with the substorm-injected plasma boundary: J. Geophys. Res. 79, 3193-3196.
- Mauk, B.H., and C.I. Meng, 1983, Characterization of geostationary particle signatures based on the 'injection boundary' model: J. Geophys. Res. 86, 3055-3071.
- Mayaud, P.N., 1980, Derivation, meaning, and use of geomagnetic indices: American Geophysical Union, Washington, D.C., 154 pp.
- Maynard, N.C., and J.M. Grebowsky, 1977, The plasmopause revisited: J. Geophys. Res. 82, 1591-1600.
- McIlwain, C.E., 1974, Substorm injection boundaries: Magnetospheric physics, Ed.: B.M. McCormac, D. Reidel Publishing Company, Dordrecht, Holland, 399 pp.
- McPherron, R.L., 1981, Substorm associated micropulsations at synchronous orbit: ULF pulsations in the magnetosphere, Ed.: D.J. Southwood, Center for Academic Publications Japan, Tokyo, Japan, 145 pp.
- Nishida, A., 1978, Geomagnetic diagnosis of the magnetosphere: Springer-Verlag, New York, N.Y., 256 pp.
- Nishida, A., 1982, Origin of magnetospheric plasma: Magnetospheric plasma physics, Ed.: A. Nishida, Center for Academic Publications Japan, Tokyo, Japan, 348 pp.
- Oguti, T., S. Kokubun, K. Hayashi, K. Tsuruda, S. Machida, T. Kitamura, O. Saka, T. Watanabe, and R.E. Horita, 1982, Multi-station f-t spectra of short period ULF waves during the Aurora-ULF-VLF campaign (Jan.-Feb. 1980) in Canada: Science Council of Japan, Tokyo, Japan, 44 pp.
- Oppenheim, A.V., and R.W. Schaffer, 1975, Digital signal processing: Prentice-Hall, Inc., Englewood Cliffs, New Jersey, 585 pp.
- Perraut, S., R. Gendrin, and A. Roux, 1976, Amplification of ion-cyclotron waves for various typical radial profiles of magnetospheric parameters: J. Atmosph. Terrest. Phys. 38, 1191-1199.

- Perraut, S., R. Gendrin, A. Roux, and C. de Villedary, 1984, Ion cyclotron waves: direct comparison between ground-based measurements and observations in the source region: *J. Geophys. Res.* **89**, 195-202.
- Pikkarainen, T., J. Kangas, B. Kiselev, N. Maltseva, R. Rakhmatulin, and S. Solovjev, 1983, Type IPDP magnetic pulsations and the development of their sources: *J. Geophys. Res.* **88**, 6204-6212.
- Pikkarainen, T., J. Kangas, H. Ranta, A. Ranta, N. Maltseva, V. Troitskaya, and L. Afanasieva, 1986, Riometer absorption events in the evening-to-afternoon sector of the auroral and sub-auroral zone and movements of the IPDP source: *J. Atmosph. Terrest. Phys.* **48**, 585-596.
- Prince, C.E., and F.X. Bostick, 1964, Ionospheric transmission of transversely propagated plane waves at micropulsation frequencies and theoretical power spectrums: *J. Geophys. Res.* **69**, 3213-3234.
- Roxburgh, K.R., 1970, A theory for the generation of "intervals of pulsation of diminishing period": Ph.D. thesis, Univ. of British Columbia, Vancouver, 92 pp.
- Rudenko, G.V., S.M. Churilov, and I.G. Shukhman, 1985, Excitation of the ionospheric waveguide by a localized packet of alfvén waves: *Planet. Space Sci.* **33**, 1103-1108.
- Saito, T., 1969, Geomagnetic pulsations: *Space Sci. Rev.* **10**, 319-412.
- Soraas, F., J.Å. Lundblad, N.F. Maltseva, V. Troitskaya, and V. Selivanov, 1980, A comparison between simultaneous I.P.D.P. groundbased observations and observations of energetic protons obtained by satellites: *Planet. Space Sci.* **28**, 387-405.
- Stewart, A.M., 1861, On the great magnetic disturbance which extended from August 28 to September 7, 1859, as recorded by photography at the Kew Observatory: *Terr. Mag.* **2**, 105.
- Tepley, L., and K.D. Amundsen, 1964, Notes on sub-ELF emissions observed during magnetic storms: *J. Geophys. Res.* **69**, 3749-3754.

- Tepley, L., and R.K. Landshoff, 1966, Waveguide theory for ionospheric propagation of hydromagnetic emissions: J. Geophys. Res. 71, 1499-1504.
- Thorne, R.M., and C.F. Kennel, 1971, Relativistic electron precipitation during magnetic storm main phase: J. Geophys. Res. 76, 4446-4453.
- Thorne, R.M., and T.R. Larsen, 1976, An investigation of relativistic electron precipitation events and their association with magnetospheric activity: J. Geophys. Res. 81, 5501-5506.
- Troitskaya, V.A., 1961, Pulsation of the earth's electromagnetic field with periods of 1 to 15 seconds and their connection with phenomena in the high atmosphere: J. Geophys. Res. 66, 5-18.
- Troitskaya, V., and M. Melnikova, 1959, About characteristic intervals of pulsations of diminishing periods: Dokl. Acad. Nauk CCCP 128, 917.
- Troitskaya, V.A., R.V. Shchepetnov, and A.V. Gul'yelmi, 1968, Estimate of electric fields in the magnetosphere from the frequency drift of micropulsations: Geomag. Aeron. 8, 634.
- Williams, D.J., and L.R. Lyons, 1974a, The proton ring current and its interaction with the plasmopause: storm recovery phase: J. Geophys. Res. 79, 4195-4207.
- Williams, D.J., and L.R. Lyons, 1974b, Further aspects of the proton ring current interaction with the plasmopause: main and recovery phases: J. Geophys. Res. 79, 4791-4798.
- Williams, D.J., 1985, Dynamics of Earth's ring current: theory and observation: Space Sci. Rev. 42, 375-396.

APPENDIX A. THE ION-CYCLOTRON INSTABILITY AND IPDP FREQUENCY

In order to comprehend how the IPDP frequency rise is produced, we must understand which physical factors affect the frequency of waves amplified by the ion-cyclotron instability mechanism as well as the magnitude of the effect of each of these factors. The dispersion relation for a left hand polarized ion-cyclotron wave propagating parallel to the background magnetic field in a two component, proton and electron, plasma is (Jacobs, 1970):

$$(k/\omega)^2 c^2 = 1 - \frac{\omega_{pe}^2}{\omega(\omega + |\Omega_e|)} - \frac{\omega_{pp}^2}{\omega(\omega - \Omega_p)} \quad (\text{A.1})$$

where ω_p is the plasma frequency, Ω is the gyrofrequency, and the subscripts (_e) and (_p) refer, respectively, to the electron and proton components.

For a cold plasma, the proton-cyclotron resonance occurs when the phase velocity $v_{ph} = \omega/k = 0$. From equation A.1, this happens when $(\omega - \Omega_p) = 0$, or $\omega = \Omega_p$. For the IPDP case, however, in which the interaction is between waves and warm protons with a non-zero streaming velocity v_u , the resonance condition can be expressed as (Jacobs, 1970):

$$\omega_{obs} - kv_{\parallel} - \omega_{em} = 0 \quad \text{or} \quad \omega - kv_{\parallel} - \Omega_p = 0 \quad (\text{A.2})$$

where ω_{obs} is the observed frequency and ω_{em} is the emitted frequency in the proton "rest frame", since the wave frequency (ω_{obs} or ω) must be doppler shifted, in the proton "rest frame", to match the proton gyrofrequency (ω_{em} or Ω_p). The proton rest frame mentioned above is that reference frame moving with velocity v_{\parallel} along the background magnetic field line in such a way that the proton parallel velocity is zero within the reference frame.

By substituting the above IPDP resonance condition into equation A.1, we can eliminate the k dependence, and therefore study the effects on the resonance frequency (ω) of parameters such as background magnetic field strength (B_0), and hot proton density (n_p) and energy (W). In order to do this, we consider the following: m_e is negligible as compared to m_p , ω is negligible as compared to ω_{pe} , the plasma is neutral ($n_e = n_p$), and the proton "parallel energy" is given by $W_{\parallel} = m_p v_{\parallel}^2/2$. The result is:

$$\omega^2 = \frac{B_0^4}{n_p W_{\parallel}} \cdot \frac{q^2}{8\pi m_p^2 c^2} \left[1 - \frac{\omega}{\Omega_p} \right]^3 \quad (\text{A.3})$$

where q represents the electric charge of the resonating

particles. Since $\omega < \Omega_p$, equation A.3 can be further simplified to (Roxburgh, 1970):

$$\omega \approx \kappa \cdot \frac{B_0^2}{(n_p W_{\parallel})^{\frac{1}{2}}} \quad (\text{A.4a})$$

where $\kappa = (q^2 / (8\pi m_p^2 c^2))^{\frac{1}{2}}$. Another common simplifying assumption is that $n_p \propto B_0$ (Roxburgh, 1970; Gendrin et al., 1971; Perraut et al., 1984). In addition, the total proton energy W can be related to W_{\parallel} by $W_{\parallel} = W \cos^2 a$, where a is the proton pitch angle. Then, substituting for n_p and W_{\parallel} , equation A.4a becomes:

$$\omega \propto \frac{(B_0)^{\frac{3}{2}}}{W^{\frac{1}{2}}} \quad (\text{A.4b})$$

Equation A.4b clearly shows the effects of background magnetic field strength and hot proton energy on IPDP frequency, and thus allows us to examine the problem of IPDP frequency shifts in terms of changes in these parameters. This result is used in the study of IPDPs in Chapters Four and Five.

APPENDIX B. THE IONOSPHERIC WAVEGUIDE

Micropulsations with frequencies in the upper part of the Pc 1 range, which includes many IPDPs, are commonly observed at low latitudes even though their source field lines are usually at $L \geq 4$, indicating that they reach the surface at $\geq 60^\circ$ GM latitude. Since these waves propagate down to the ionosphere as field-guided left-hand (LH) polarized hydromagnetic waves, also termed slow mode hm waves, they must reach these lower latitudes through horizontal propagation from higher latitudes in the ionospheric waveguide. Considerable experimental evidence exists for propagation in such a waveguide along the geomagnetic meridian, though the presence of ducting in off-meridian directions is less clear. (Tepley and Landshoff, 1966; Campbell and Thornberry, 1972; Fraser, 1975a,b; Althouse and Davis, 1978; Hayashi et al., 1981).

The ability of the ionosphere to trap and guide hm waves is due to its height-dependent ionization structure (see fig. 65). The pronounced peak in ionization creates an Alfvén velocity minimum there, and it is within this layer that ducting can take place. Note that figure 65 also shows that the ionization peak is sharper at night, resulting in lower duct attenuation than during the day.

As mentioned above, slow, or ordinary, mode waves are field guided, and so cannot cross the magnetic field lines.

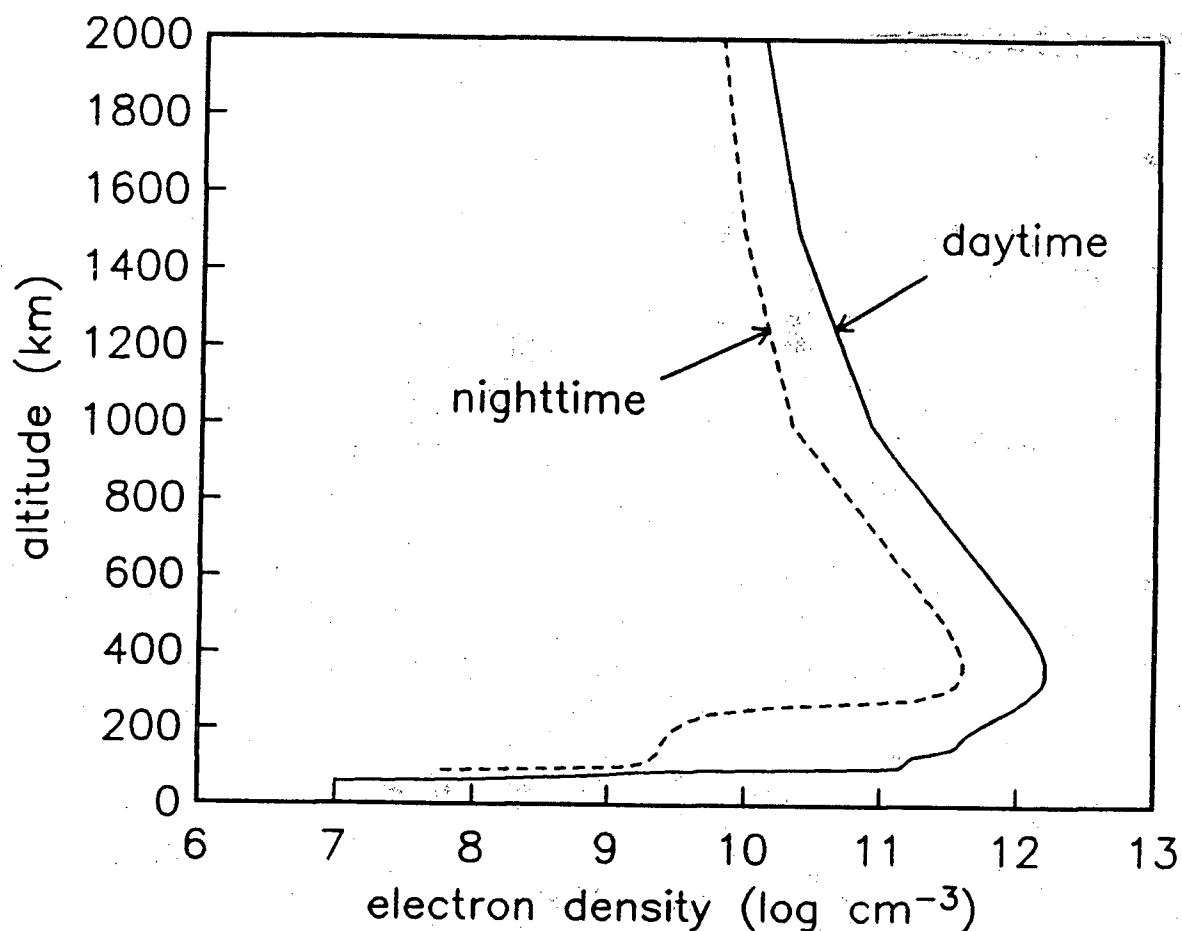


FIGURE 65.

Electron density profiles for both day and night sunspot maximum conditions (Prince and Bostick, 1964). Note that at night, the F2 layer ionization is, relative to the daytime profile, much stronger than the layers beneath it.

This, therefore, cannot be the mode propagating horizontally in the ionospheric duct, since, except near the equator, the geomagnetic field lines cut obliquely across the duct. The mode believed to carry the energy horizontally in the duct is the fast, or extraordinary, mode. Propagation of this fast mode is isotropic, and since it is not guided by the ambient magnetic field, it can travel horizontally within the duct.

The coupling between these two modes, which is necessary for energy injection into the duct, has been attributed to the finite extent of the area of ionospheric incidence, also termed the secondary source, by Jacobs and Watanabe (1962). It is also said to be a consequence of altitude-dependent variations in polarization of the incoming slow mode wave as it traverses the F-layer (Altman and Fijalkow, 1980). Numerical analysis presented in the latter work also suggests that energy injection into the duct is most efficient at higher latitudes ($\geq 45^\circ$), and that it takes place over the entire altitude range of the F2-layer duct. Other ionospheric waveguide models (such as Manchester, 1966, 1968; Greifinger and Greifinger, 1968) have not specifically treated the problem of injection into the duct other than to say that mode coupling takes place in the lower ionosphere.

Once in the ionospheric duct, the trapped wave

propagates horizontally in a series of reflections from the upper and lower duct walls, as illustrated in figure 66. This figure shows that most of the energy is reflected from narrow altitude ranges at both the top and bottom of the duct, giving a well defined duct region. The reflection coefficients at these walls for the trapped fast mode wave are typically 0.5 - 0.85 (Altman and Fijalkow, 1980) (see fig. 66). Estimates of attenuation in the duct vary somewhat depending on the ionospheric waveguide model considered; Manchester (1968), attributing attenuation primarily to absorption, estimated ≤ 4 db/1000km, while Altman and Fijalkow (1980) found a rate of 6-9 db/1000km due to fast-to-slow mode coupling in the duct. A diurnal variation in duct attenuation is also produced by those models considering the daily variations in ionospheric structure. The appearance of the E region in the daytime ionosphere strongly affects the ionization profile (cf. fig. 65), resulting in increased duct attenuation during the day. This increase, relative to nighttime attenuation, has been calculated to be of roughly an order of magnitude (Greifinger and Greifinger, 1968) or more (Manchester, 1966). The experimental results of Althouse and Davis (1978) yielded a typical attenuation of ≈ 6.5 db/1000km during the early morning hours, though the values were quite variable from day to day and reached as high as 13 db/1000km.

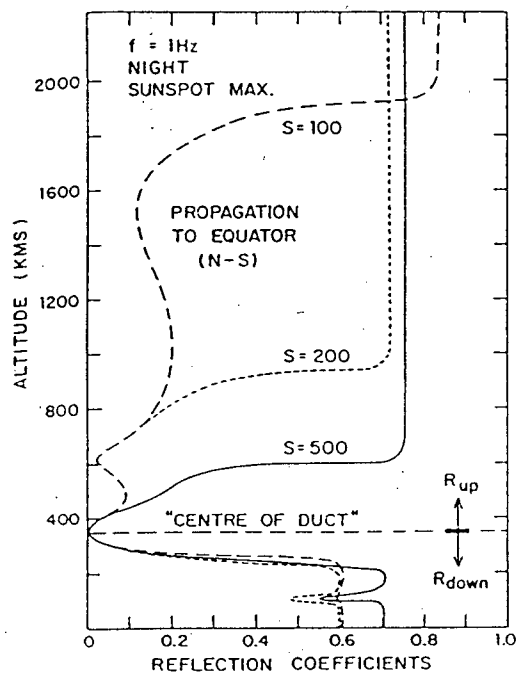
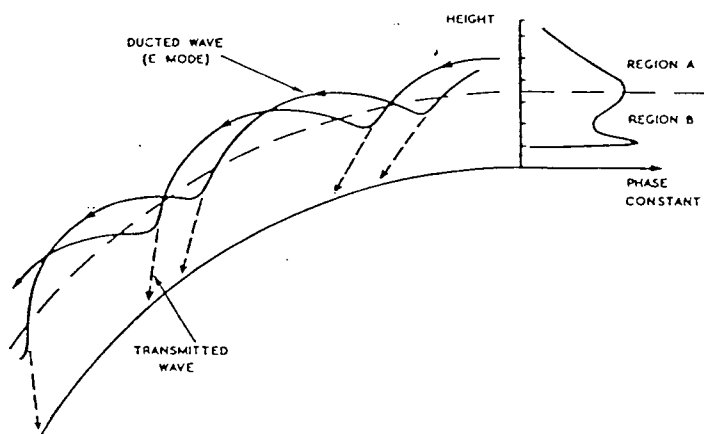


FIGURE 66.

Top: Typical propagation paths for trapped fast mode (labelled E (extraordinary) mode in the diagram) waves in the F2 region duct (after Manchester, 1966). Bottom: Height profile of R-mode reflection coefficients for different values of Snell's constant $S (=n \cdot \sin \theta)$ (after Altman and Fijalkow, 1980).

Finally, it should be pointed out that the attenuation versus frequency profiles produced by the different waveguide models differ significantly.

The ionospheric waveguide also appears to exhibit a lower cut-off frequency near 0.5Hz. This cut-off frequency varies with duct conditions and has been variously calculated at 0.45Hz by Manchester (1968), with the cut-off being due to attenuation, and depending on the ionization conditions between 0.10 and 0.36 Hz by Greifinger and Greifinger (1968), with the cut-off being due to boundary conditions. One aspect on which the different models agree fairly well, both among themselves and with observations, is the group velocity of fast mode propagation within the duct, which is typically 300-800 km/sec, depending on ionospheric conditions (Tepley and Landshoff, 1966; Manchester, 1966, 1968; Greifinger and Greifinger, 1968; Altman and Fijalkow, 1980). Note that two of the most important factors controlling ionization conditions in the ionospheric waveguide are the local time and the sunspot number. The events studied in this thesis were recorded near sunspot maximum.

The waveguide results discussed so far have been for meridional propagation only, since a common simplifying assumption in duct models, justified by some experimental results, has been to consider only propagation in this

direction. Greifinger and Greifinger (1973) showed that, for off-meridian directions, coupling between the ducted fast mode wave and the field guided slow mode wave produces generally two to four large peaks in attenuation within the IPDP frequency band. The frequency ranges covered by these peaks, each of which is ≈ 0.1 to 0.3 Hz wide, are dependent on geomagnetic latitude. Thus, for any off-meridian direction except purely east-west, each frequency component of a wave will encounter a region of high attenuation as the latitude varies along the wave's path, effectively eliminating off-meridional ducting (Greifinger and Greifinger, 1973). The treatment of Altman and Fijalkow (1980) included ducting in both the north-south and east-west directions, and found that attenuation of waves travelling in the east-west direction to be generally only slightly larger than for those travelling along the meridian. Experimentally, the Pc 1 observations of Hayashi et al. (1981) also indicate that ducting occurs preferentially in the east-west and north-south directions.

The polarization characteristics of some Pc 1 band micropulsations, including IPDPs, can be very useful in understanding these events. As stated above, the initial incoming slow mode wave has LH polarization. However, the ducted mode into which it is converted, the fast mode, has RH polarization. This could be expected to lead to

observations of LH polarization at ground stations below the incoming field guided wave, and RH polarization at stations beneath the ducted wave. However, it has been shown that the horizontal component perpendicular to the direction of propagation is not transmitted to the surface, so that, at large distances from the source field lines, the polarization should be nearly linear with the ellipse axis aligned with the direction of propagation (Greifinger and Greifinger, 1968; Rudenko et al., 1985). The vertical component of the wave field will vanish at the surface, assuming infinite ground conductivity (Greifinger, 1972). In regions near but not under the incoming wave, the polarizations can be complex, with the direct wave, here appearing as RH (Greifinger, 1972), superimposed on the linear appearance of the ducted wave.

Experimentally, Althouse and Davis (1978) and Hayashi et al. (1981) obtained mixed results from Pc 1 polarization studies, though in the former case stations far from the source did show mainly linear polarization. These results may be due to the near source complex region noted above and/or to the superposition of two or more waves arriving at the same site from different directions as a result of horizontal gradients in ionospheric densities affecting wave propagation paths (Altman and Fijalkow, 1980).

In general there is a reasonably good qualitative match

between most model calculation results and duct propagation observations. Examples of this include the existence of a cut-off frequency, general polarization patterns, diurnal variations in duct attenuation, and lack of a significant vertical wave component. However, on a more detailed level, including quantitative aspects, the models' predictions do not always agree well with each other or with experimental results. This is quite likely due to the different approaches taken by some authors, and, perhaps more importantly, the variant assumptions used in their different works. These assumptions include, among other aspects; vertical stratifications of the ionosphere, wave incidence angles, horizontal homogeneity in the ionosphere, collisions, mode coupling, background magnetic fields, and ground conductivity.

Such disagreements make it impractical to use any specific results as an aid to IPDP interpretation. Therefore, the characteristics of ionospheric propagation required in this thesis have been obtained from the data analysed for the Feb. 14 and Feb. 15 IPDPs. Attenuation has been calculated from the measured signal levels from stations on a north-south line, and proved to be greater than most model results. While the attenuation found from the daytime event, the Feb. 15 event, was larger than that for the night event, the Feb. 14 IPDP, the difference was

not as extreme as predicted. The polarization pattern seen in these IPDPs of LH below the secondary source and RH elsewhere was as expected. In addition, there were intervals of LH polarization covering the low frequency beginnings of the events, indicating the presence of non-ducted waves at frequencies below the duct cut-off frequency. These cut-off frequencies were generally similar to, though somewhat higher than, the expected values. The pattern of their diurnal variation, lower during the day, was as predicted.

APPENDIX C. GEOMAGNETIC INDICES

A geomagnetic index is a system which attempts to provide summarized information concerning the behaviour of a specific geomagnetic variation. Indices are generally presented as discrete values calculated from a certain time interval using data from one or more geomagnetic observatories. There are a number of different kinds of geomagnetic indices related to various geomagnetic phenomena of both local and planetary scale. An index is not only useful for studying the specific geomagnetic variation from which it is calculated, but can also be helpful in understanding related geomagnetic phenomena. In this thesis, we have used or mentioned three indices in the latter manner. These are the Dst index (ring current), the Kp index (magnetospheric activity), and the AE index (auroral electrojets). A description of each of these is presented below. If more information on these, or other, indices is desired, the reader should refer to the monograph of Mayaud (1980).

Dst Index

The magnetic field of the ring current, which flows westward around Earth in the equatorial plane, has the effect of depressing the dipole field at Earth's magnetic equator. The Dst index is intended to monitor this effect, and therefore also monitor the intensity of the ring current

itself. It does this quite well, and is probably the most accurate of all the geomagnetic indices in representing the phenomenon for which it is derived. There are, however, some difficulties in determining the Dst index; most importantly, separating ring current variations from other transient variations and from secular variations.

Some transient variations are averaged out by the one hour interval over which each value of the Dst index is calculated. Others, such as the first phase of a storm, that is, the period of increased H-component which may precede the main phase of a storm, can contribute to the index, however. The effect of the DP 2 irregular variation, quasi-periodic fluctuations with a period of ≈ 1 hour, could significantly interfere with the Dst index near the equator, but its effect is minimized by not using equatorial stations in the calculation of the index. Auroral disturbances could also affect this index, though, the effect of the westward electrojet is minor at low latitudes, and the eastward electrojet is recognized as being due to the partial ring current allowing its effects to be considered part of the phenomenon being monitored (Mayaud, 1980). The regular daily variations must also be removed in order to accurately calculate the Dst index. This is accomplished by computing a statistical version of this daily variation from the five quietest days of each month, and then subtracting this from

the observed data for each day of that month. Since the daily variations are not constant from day to day, there are necessarily errors introduced by this process though these should be reduced somewhat when all the stations are averaged together to produce the actual Dst index. Note also that these daily variations do not affect the stations when they are on the night side of Earth. Lastly, secular variations must also be removed if the Dst index is to be useful for long term studies.

Before actual calculation of the Dst index can begin, a reference level must be set. This is determined from the H-component annual means calculated from the five quietest days of each month (Mayaud, 1980). Note that this reference level is not a zero level, since the ring current always exists, and therefore only provides a reference to ring current intensity in very quiet times. For each station, a raw Dst estimate is then calculated as follows:

$$\text{Dst} = H_{obs} - Sq(t) - H_0(t) \quad (C.1)$$

where H_{obs} is the observed H-component of the magnetic field, $Sq(t)$ is the estimated daily variation, and $H_0(t)$ is the reference level. These Dst estimates from each station are averaged to remove local effects and then corrected for latitude in order to yield the ring current effect at the

equator. This last step requires that the stations all be at similar latitudes. The actual observatories used are Honolulu (Hawaii), San Juan (Puerto Rico), Hermanus (South Africa), and Kakioka (Japan). They are well spread out in longitude in order to minimize local effects, and average about 28° from the geomagnetic equator. This is at a low enough latitude to be near the ring current and to minimize auroral effects, and still far enough from the equator to avoid DP 2 interference.

With this process, a final Dst is calculated, in γ , for each hourly interval, leaving a simple set of 24 Dst values per day. The index can be either positive or negative. Large negative values are indicative of large magnetic field depressions at the equator, common during storm times when the ring current becomes strongly enhanced by substorm plasma injections.

Kp Index

The Kp index consists of a quasi-logarithmic scale indicative of mid to high latitude geomagnetic activity on a planet-wide basis. It is derived from local K indices calculated at 11 geomagnetic observatories ranging from 45° to 63° corrected geomagnetic latitude (Hakura, 1965).

The K index at each observatory is determined for each 3-hour period, for example, 0000-0300 UT, from the component, either H or D, showing the larger range of

irregular variations within that period. The index is intended to be sensitive to irregular variations only and, as with the Dst index, the regular daily variation must be removed. The range from the chosen component, the difference between the maximum and minimum levels of that component within the specified interval, is then assigned to a class of ranges, each with an associated number from 0 to 9. The dividing lines between these range classes increase quasi-logarithmically and are adjusted by latitude, since the amplitude of the ranges displayed varies strongly with latitude. This adjustment makes the distribution of K indices uniform at each observatory.

Before the Kp index can be determined from the K indices produced by the 11 observatories, further standardization of the various K's must take place. Beyond latitudinal effects, there exist further differences in the K's from each of the observatories, and also from a single observatory in different seasons. These are removed by determining conversion tables for each observatory which enable their K's to be converted into a standardized form, termed Ks. The Kp index is then just an average of the Ks indices for each 3-hour period from the 11 observatories distributed around the globe. The Kp scale is actually divided into finer intervals than the whole numbers mentioned above. Each K range class is split into thirds,

giving a scale where the $K_p = 2$ range, for example, is divided equally into $K_p = 2_-$, 2_0 , and 2_+ sections. Active storm times typically have K_p 's of between 3 and 6, while K_p 's of ≈ 8 or more, representing extremely active times, are quite rare. Conversely, very quiet periods, which are much more common than $K_p \geq 6$ times, have K_p 's of less than 1.

AE Index

The AE index is designed to be a measure of global auroral electrojet activity. The electrojets are the predominant form of auroral-zone magnetic variation. Thus, as in the case of the Dst index but different from the K_p index, a well defined class of irregular variations is being monitored.

A global network of up to 13 observatories at or near auroral zone latitudes, of $\approx 70^\circ$ corrected GM Lat., is used to determine the AE index. The current directions of the eastward and westward electrojets make the H-component the logical one to use in determining this index, with the eastward electrojet producing positive ΔH deviations and the westward electrojet negative ΔH deviations. For each month, the reference level from which these deviations are calculated is determined using an average of the H-component of the five quietest days of that month. After removal of the reference level, the H-component traces from all of these stations are superimposed, yielding upper and lower

envelopes. The upper envelope is the AU index, and monitors the eastward electrojet, while the lower envelope is the AL index, which monitors the westward electrojet. This envelope technique means that, for any specific time, each index is actually given by the one station best situated to observe that electrojet at that time. Note that these indices are produced in a digital form with a 2.5 minute sampling rate.

The AE index is simply the difference between the AU and AL indices, that is: $AE = AU - AL$. This operation removes ring current contamination, which is significant only in very active times, from the AU and AL indices, leaving the AE index dependent only on the electrojets. Actually, the regular daily variation still interferes with the AE index, but is quite small, ≈ 10 s of γ , compared to electrojet ΔH amplitudes of ≈ 100 s of γ . Other difficulties which can interfere with this index include various, and unknown, ground induction effects at the observatories, the H-component not being necessarily precisely normal to the current directions, and a less than ideal distribution with respect to latitude and longitude of the observatory network as caused largely by the uneven distribution of land masses. Since the auroral electrojets are a direct result of magnetospheric storms, the AE index reaches large values, often $\geq 1000\gamma$, in stormy periods, while very quiet times can have AEs of $\leq 100\gamma$.